Variable-density swirl-enhanced mixing within the lower plenum of high-temperature nuclear reactors

Von der Fakultät Energie-, Verfahrens- und Biotechnik
der Universität Stuttgart

zur Erlangung der Würde eines Doktors der
Ingenieurswissenschaften (Dr.-Ing.) genehmigte Abhandlung

vorgelegt von

Dominik von Lavante

aus Heidelberg

Hauptberichter: Prof. Dr.-Ing. habil. E. Laurien

Mitberichter: Prof. M. Casey D.Phil.

Tag der mündlichen Prüfung: 8. 12. 2009

Institut für Kernergetik und Energiesysteme

Juni, 2009

I would like to dedicate this thesis to my loving parents...
I am forever grateful for their life-long support and dedication to my wellbeing.

Acknowledgements

This thesis could have never been written without the support of many helpful people, whose efforts have been greatly appreciated and I want to thank all these persons for their help.

First and foremost, incredible thanks are due to my supervisor Prof. Dr.-Ing Eckart Laurien. From the introduction into the subject of this thesis at the beginning of the long journey to my doctorate degree, till the very end with his helpful insights on the analysis of data, he has always been very supportive in every aspect of my studies at Stuttgart.

Special thanks is also due to Prof. Lohnert for the insightful discussions surrounding the HTR-Module, and the nuclear industry in general. Without his work and efforts I could not have been part of the exciting HTR-PM project at the end of my stay in Stuttgart. I also have to thank Frau Vencia for her organizational help and support, as well as Frau Böhm for keeping the IT-systems running.

This research would not have been possible without the help and support of my colleague Dr.-Ing Wintterle. His help during the start of my research enabled me to quickly come to grips with CFX and his knowledge of many undocumented features of CFX were crucial for completing the work of this thesis. Furthermore, I want to thank Mr. Zhu, Herr Zirkel, Herr BenSaid and all other colleagues of the IKE for their support, companionship and for the highly informative discussions with them. Particular thanks are also due to Prof. Dr.-Ing Jakirlic for his assistance in broadening my knowledge in insightful discussions in the field of turbulence modeling during several ERCOFTAC meetings.

A sincere thank-you also to all the proof-readers of this thesis: My father Ernst von Lavante and my brother Etienne.

I am very grateful for the frequent discussions with my father in the general field of fluid mechanics and help in learning LaTeX. This gratitude extends as well to my brother Etienne for his help with LaTeX templates as well as aid in relearning Matlab for the analysis of data of this thesis. Ultimately, no words can express how grateful I am for the life-long support and motivation through my parents, and the sacrifices they have made to allow my studies at Impington Village College and Imperial College London.

Abstract

With recent progress in high-temperature pebble-bed reactor programs research focus has started to include more ancillary engineering issues. One very important aspect for the realizability is the mixing of hot and colder helium in the reactor lower plenum. Under nominal operating conditions, depending on core design, the temperature of hot gas leaving the core can locally differ by up to 210 °C. Due to material limitations, these temperature differences have to be reduced to at least 15 °C at the turbine inlet, or heat exchanger inlet, by mixing in the lower plenum. To achieve this, swirling flows can be used. Several reduced-size air experiments have been performed to demonstrate the ability, but their applicability to modern commercially sized reactors is not certain. With the rise in computing power CFD simulations can be performed in addition, but advanced turbulence modeling is necessary due to the highly swirling and turbulent nature of this flow. The presented work uses the geometry of the German HTR-Modul which consists of an annular mixing channel and radially arranged ribs. Using the commercial CFD code ANSYS CFX, a detailed analysis of the complex 3D vortical flow phenomena within this geometry has been made. Several momentum transport turbulence models, e.g. the classical k-ϵ model, advanced two-equation models and Reynolds-Stress Models were compared with respect to their accuracy for this particular flow. In addition, the full set of turbulent scalar flux transport equations was developed, validated and implemented for modeling the three components of turbulent transport of enthalpy separately and were compared with the standard turbulent Prandtl number approach. As expected from previous work in related fields of turbulence modeling, the differences in predicting the mixing performance between models were significant. Only the full Reynolds-Stress model coupled with the scalar flux equations was able to reproduce the experimentally observed reduction of mixing efficiency with increasing Reynolds number. The correct scaling of mixing efficiencies demonstrates that the utilized turbulence models are able to reproduce the physics of the underlying flow. Hence they could be employed for the scaling and optimization of the lower plenum geometry. The results also showed that the original geometry used for the HTR-Modul is insufficient to provide adequate mixing, and hence for future reactor designs adequate mixing might not be guaranteed. Based on this work, an optimization for future lower plenum geometries has become feasible.

Zusammenfassung

Mit dem Fortschritt in der Entwicklung von Kugelhaufen-Hochtemperaturreaktoren und prismatischen Blockhochtemperaturreaktoren, als Teil der internationalen Forschungsprogrammen zu Generation IV Nuklearreaktoren, richtet sich der Fokus aktueller Forschungsbemühungen mehr und mehr auf sekundäre Bereiche, abseits der Thermo-Hydraulik des Reaktorkernes. Zur Realisierung von Kugelhaufen-Hochtemperaturreaktoren (HTR) ist hierbei ein wichtiger Aspekt die Vermischung von heißem und kaltem Helium im unteren Plenum des Reaktordruckbehälters. Je nach Reaktordesign und -auslegung betragen die Temperaturunterschiede der aus dem Reaktorkern austretenden Gase bei Normalleistung bis zu 210 °C. Um den Verschleiß und die Belastbarkeit von nachgeschalteten etwaigen Heliumturbinen oder Dampferzeugern zu minimieren, müssen diese Temperaturunterschiede, bei heute verfügbaren Bauteilen und Materialien, auf weniger als 15 °C reduziert werden. Um diese Vorgabe zu erreichen, wurden in der Vergangenheit mehrere kleiner skalierte Luftexperimente mit starker Drallströmung durchgeführt, um die Machbarkeit dieser Vermischung zu untersuchen. Die Ergebnisse dieser Untersuchungen, wenn hochskaliert auf reale Reaktorgrößen wie auch Bedingungen, weisen auf die grundsätzliche Machbarkeit dieser Vermischung hin, aber die Anwendbarkeit und Skalierung dieser Experimente im Einzelnen auf moderne Reaktoren, wie sie sich momentan in Entwicklung befinden, ist nicht garantiert.

Aufgrund der rasanten Entwicklung der Computer-Rechenleistung ist es nun möglich diese Strömung ebenfalls mittels CFD, wobei hier im Besonderen auf die genaue Modellierung der stark verdrallten turbulenten Strömung mittels geeigneten Turbulenzmodellen zu achten ist, zu untersuchen. Die hier vorgestellte Arbeit basiert auf der Geometrie des HTR-Moduls welche aus einem Ringsammelkanal mit radial nach innen gerichteten rippenähnlichen Hohlräumen besteht. Mittels des CFD Softwarepacketes ANSYS CFX konnte eine detaillierte Analyse der unteren Plenumsströmung mit ihren komplexen, dreidimensional verdrallten Strömungsphänomenen erbracht werden. Es wurden mehrere Turbulenzmodelle, z.B. klassisches k-ϵ, shear stress transport und Reynoldsspannungsmodelle, für die Impulsgleichungen ausgewählt und bezüglich ihrer Modellierungsgenauigkeit zu der vorherrschenden Strömung miteinander verglichen. Zur Modellierung des turbulenten Transports der Enthalpie wurden zusätzlich Transportgleichungen der turbulenten skalaren Flüsse entwickelt, implementiert und mittels bekannten Testfällen aus der Turbulenzmodellierung validiert. Diese Modelle wurden mit der herkömmlichen Methode der Modellierung der turbulenten Diffusion mittels des Wirbelviskositätsansatzes und der Annahme einer turbulenten Prandtl Zahl verglichen. Es zeigten sich erhebliche Unterschiede in den Ergebnissen zwischen den verschiedenen Turbulenzmodellen. Einzig das Reynoldsspannungsmodell kombiniert mit dem skalaren Flussmodell war in der Lage die experimentellen Ergebnisse der Luftexperimente zum unteren Plenum des HTR-Moduls mit

hoher Genauigkeit zu reproduzieren. Besonders die Skalierung der Mischeffizienz mit variabler Reynoldszahl ist hierbei hervor zu heben, welche nur mittels Reynoldsspannungsmodellen (RSM) im Vergleich mit den Experimenten reproduziert werden konnten.

Mit dem Nachweiß der Skalierbarkeit in Abhängigkeit der Reynoldszahl mittels des eingesetzten Turbulenzmodells, ein RSM in Kombination mit skalarem Flussmodell, kann induziert werden, dass die vorherrschende Physik der drallbehafteten turbulenten Mischvorgänge richtig reproduziert worden sind. Beim Anwenden dieses Turbulenzmodells auf die realen Bedingungen des HTR-Moduls wurde eine Verschlechterung der Mischeffizienz wie auch eine Erhöhung des Druckabfalls gegenüber den erwarteten Werten aus der Extrapolation der experimentellen Werten beobachtet. Diese Unterschiede beruhen auf eine zu stark vereinfachte Methode der Extrapolation in den publizierten Experimenten in Kombination mit nicht optimal gewählten Betriebspunkten. Auf der Basis dieser Arbeit können nun verbesserte Luft-Experimente für zukünftige HTRs aufgebaut werden. Die Ergebnisse für den HTR-Modul zeigen weiterhin, dass die Mischeffizienz der ursprünglich gewählten Geometrie unter Umständen nicht ausreichend ist, und dass das Reduzieren der Temperaturunterschiede in zukünftigen Reaktoren unter Umständen problematisch werden kann. Die in dieser Arbeit vorgestellten Modellierungsmethoden wie auch die implementierten Turbulenzmodelle ermöglichen nun die Optimierung des unteren Plenums für zukünftige Reaktoren.

Contents

List of Figures

Nomenclature

Dimensionless Variables

$\mathbf{Ec}$	Eckert number
$\mathbf{Eu}$	Euler number
$\mathbf{Fr}$	Densimetric Froude number
γ	Ratio of maximum density difference
κ	Ratio of specific heat coefficients
$\mathbf{Ma}$	Mach number
Ψ	Dimensionless mixing efficiency
$\mathbf{Pe}$	Peclet number
$\mathbf{Pr}$	Prandtl number
$\mathbf{Pr}_t$	Turbulent Prandtl number
$\mathbf{Re}$	Reynolds number
$\mathbf{S}$	Swirl number
ξ	Dimensionless pressure loss coefficient

Greek Variables

δ_{ij}	Kroneker Delta
ϵ	Turbulent scale of dissipation
$\widetilde{\epsilon}$	Density-weighted turbulent scale of dissipation

Γ	Diffusion coefficient for a passive scalar
λ	Thermal diffusion coefficient
μ	Dynamic viscosity of a fluid
μ_t	turbulent viscosity from the Boussinesq-approximation
Ω	Turbulent time scale of dissipation
$\overline{\Phi}$	Arbitrary time-averaged tensorial quantity
Φ	Arbitrary instantaneous tensorial quantity
Φ'	Arbitrary (Reynolds decomposed) fluctuating tensorial quantity
Φ''	Turbulent Favre-decomposed fluctuations of an arbitrary tensor
φ	Passive scalar transported within a fluid
$\widetilde{\Phi}$	Density-weighted average (Favre average) of an arbitrary tensor
$\overline{\rho}$	Time-averaged density
ρ	Instantaneous density of a fluid
ρ'	Reynolds-decomposed fluctuating density
σ_{ij}	Deviatoric stress tensor of a fluid, see eqn. 2.17
σ_{ij}^{Re}	Reynolds stress tensor
Θ_{ij}	Fluid strain tensor

Latin Variables

P	Pressure
R	Universal gas constant
R_o	Outer radius of a round pipe
T	Temperature
c_p	Specific heat capacity at constant pressure
c_v	Specific heat capacity at constant volume
D	Molecular diffusion constant
e_i	Thermodynamic internal energy of a fluid per unit mass

g	Gravitational acceleration constant
h_0	Total enthalpy
k	Turbulent kinetic energy
k	Tturbulent kinetic energy
M	Molar mass of a gas
ΔP	Absolute pressure loss
p_c	Critical pressure
r	Radius, distance from the centerline of a round pipe
t	Time
T_c	Critical temperature
$\overline{\rho}\,\widetilde{u_i''\varphi''}$	Turbulent flux of a passive scalar (Favre averaged)
$\overline{\rho}\,\widetilde{u_i''u_j''}$	Reynolds stress tensor (Favre averaged)
$\rho\,\overline{u_i'u_j'}$	Reynolds stress tensor
U	Characteristic velocity used in dimensional analysis
u	Axial velocity in round pipe flow
u_1	Velocity of a fluid in x-direction
u_2	Velocity of a fluid in y-direction
u_3	Velocity of a fluid in z-direction
v_c	Critical velocity
w	Tangential velocity in cylindrical coordinates
x	Vector direction parallel to the x-axis of a cartesian coordinate system
y	Vector direction parallel to the y-axis of a cartesian coordinate system
y	Vector direction parallel to the z-axis of a cartesian coordinate system

Chapter 1

Introduction

1.1 Motivation

Nuclear reactors account for approximately 22% of electricity generation in the OECD [1] countries and 15% world wide, the equivalent in electricity generation preventing the consumption of roughly 1.2 billion tons of coal per year and preventing the emission of approximately 3.2 billion tons of CO_2 per year. This would be the equivalent of nearly 11% of all CO_2 equivalent emissions by mankind based on the year 2005 [2]. Given the current state of urgency in mitigating CO_2 equivalent emissions to reduce the severity of global warming, there are no other technologies currently available that could scale with the necessary size to effect the global CO_2 footprint of mankind in a noticable way.

High-Temperature Reactors (HTR) are helium cooled, graphite moderated nuclear reactors with several unique features compared to conventional light water reactors (LWR). One of them, the origin of its name, is its very high coolant exit temperatures ranging between 700 to 950 °C, enabling much higher thermal plant efficiencies compared to LWRs. These temperature ranges are sufficiently high for most processes in the petro-chemical industry and nearly all other industrial applications needing process heat. Among other reasons, the US Department of Energy has hence chosen this reactor for additional funding within the "Generation IV" future nuclear reactor research program. It is envisaged to use this reactor type for the CO_2-free production of hydrogen via the thermo-chemical sulfur-iodine cycle or high-temperature electrolysis.

These high coolant exit temperatures are possible due to the use of ceramic coated fuel particles, which prevent the release of radioactive fission products well beyond temperatures of 1600 °C [3; 4]. In combination with a low reactor core power density, this allows the reactor to always remain below the temperature of failure of these ceramic barriers via purely passive means of cooling such as heat conduction and radiation. The passive and safe coolability of the core is explicitly possible during any combination of postulated accidents such as loss of coolant, convection, air- and water ingress. HTR reactors are hence deemed to be inherently safe and are often called "walk away safe". Even during the worst accident possible, no operator action is required to keep the public safe from any hazardous release of ionising radiation.

The idea of developing a "walk away safe" graphite moderated gas-cooled reactor, the basis of HTRs, was already conceived during the late 50s / early 60s. Only due to advances in metallurgy, fluid mechanics, and especially due to advances in the fabrication of high-quality ceramic coated particles has interest in this reactor design grown since the late 1980s/early 1990s. Especially the work done by the Forschungszentrum Jülich, the place of origin of the modern TRISO (TRIple ISOtropic layers, see [3; 4]) fuel particle now used by all HTRs, and that by Fort St.Vrain, stand out in this regard.

The high temperature TRISO particles are key to the entire safety concept of HTRs. TRISO particles consist of a central kernel made up of uranium-dioxide fuel with a diameter of approximately 500 micrometers. Surrounding this fuel kernel are three protective layers: First a sponge-like layer of graphite which can accommodate fuel swelling and build up of gaseous fission products, next a mechanically very strong layer of silicon carbide, and lastly a layer of pyrolytic graphite; a very strong form of near perfect crystalline graphite. Unlike all other nuclear reactor types, there is no need for a high-strength containment building surrounding the primary circuit to prevent the catastrophic release of fission products during postulated very severe accidents: the HTR reactor itself is made up of billions of micro containment structures in the form of its micrometer small TRISO particles, each magnitudes stronger and more leak-tight than any civil structure could theoretically be. And even in the case of failure of a coated particle due to manufacturing errors, the amount of release of radioactive isotopes stored within a single particle is minuscule and poses a near zero threat to the public.

TRISO particles can reliably retain fission products at approx. 1200 °C for months with burn-ups of up to 200GWd/t heavy metal content (commercial light water reactors achieve max. 60 GWd/t), and more than 1600 °C during short duration peaks [3; 4]. Systematic failure of the ceramic layers occurs at temperatures beyond 2000 °C. Ensuring that during normal operation as well as during any accident conditions maximum temperatures remain below these limits makes detailed and reliable analysis of the coupled thermo-neutronics necessary.

HTRs can be broadly divided into two different groups: Block structured and pebble bed. The block structured reactor core is similar in topology to any graphite moderated gas cooled reactor. Within the pressure vessel, the TRISO particles are compacted into cylindrical fuel pellets and inserted into fuel channels within prismatic graphite blocks. These graphite blocks have cooling channels and control rod holes bored into them and are stacked on top of each other within the pressure vessel. The US as well as Japanese Generation IV HTR concepts use this reactor topology, mostly because of the ability to reuse well tested system codes developed for light water reactors, such as Relap-5, and due to the ability of achieving higher power levels per reactor pressure vessel.

In a pebble bed topology (figure 1.1 and 1.2) the fuel particles are compressed into billiard ball sized graphite spheres and are put into the reactor cavity, which is lined by graphite moderator blocks. These spheres are continuously cycled during operation and depending upon burn-up either sent again through the core or removed to the spent fuel pile. Pebble bed HTRs offer several advantages over block structured HTRs. Their technical availability is significantly improved since no down-time is required to refuel the core. Due to continuous recycling of fuel, excess reactivity within the core can be maintained at an absolute minimum at all times, making the reactor much safer during hypothetical accident conditions (ease of shutdown as well as limited inventory of fission products and fissile material). Additionally, this opens up an extreme flexibility of the reactor to radically different fuel compositions (different Uranium enrichment levels, Plutonium or Thorium) without any changes to the core as well as safety of the reactor. Since the fuel pebbles will only be put into the spent fuel pile after achieving a maximum burn-up value, fuel utilization will be very close to the maximum licensed levels, reducing fuel costs significantly. Pebble bed reactors also have a few disadvantages over block structured HTRs, namely a significantly lower thermal output per reactor vessel (300MW$_{th}$ vs +600MW$_{th}$), and more importantly, the necessity of developing and verifying a completely new code base for the coupled thermo-neutronics codes.

One particular issue of this type of reactor geometry is the mixing of hot gases as they exit the reactor [5]. A pebble bed type reactor has a strongly radially decreasing power density which, coupled with poor gas mixing within the pebble bed, leads to a radially varying temperature profile of the helium coolant. Depending on core geometries, differences can be as high as 210 °C at the end of the reactor core [5; 6; 7]. Additionally, higher temperature differences can be caused due to leakage flows between the graphite moderator/building blocks. In a worst-case scenario this could cause temperature differences in excess of 400 °C in the hot gas header. These temperature differences have to be reduced to at most 10-15 °C [5] at the inlet of the heat exchangers to reduce thermal stresses and hence to guarantee a long service life of those components.

Related to the issue of sufficient hot gas mixing is the issue of pressure drop within the lower plenum. Due to safety concerns as well as a reduction of complexity, the reactor is planned to be equipped with only a single one-stage blower, which puts a limit to the maximum blower power of approximately 5MW, and hence a severe limit to the allowable pressure drop within the entire primary circuit. The lower plenum alone accounts for approximately 30% [5] of the entire pressure drop within the primary circuit. Hence the engineering challenge of providing efficient mixing without causing too strong loss of pressure has to be solved for the lower plenum of pebble bed HTRs.

For block type reactors, the issue of insufficient mixing is not quite as severe as with pebble bed topologies. Due to the fixed nature of the core, the heat input into each individual coolant channel can be determined in advance, and by placing shutters into these channels, one can control coolant flow such that the exit temperature out of each coolant channel is roughly equal. While this may sound simple at first sight, it has to be noted that the exact heat input into each coolant channel changes over time due to the burn-up of fissile material as well as burnable neutron poisons, causing changes in the distribution of power within the core over time. Transient behavior, such as performing load following by the

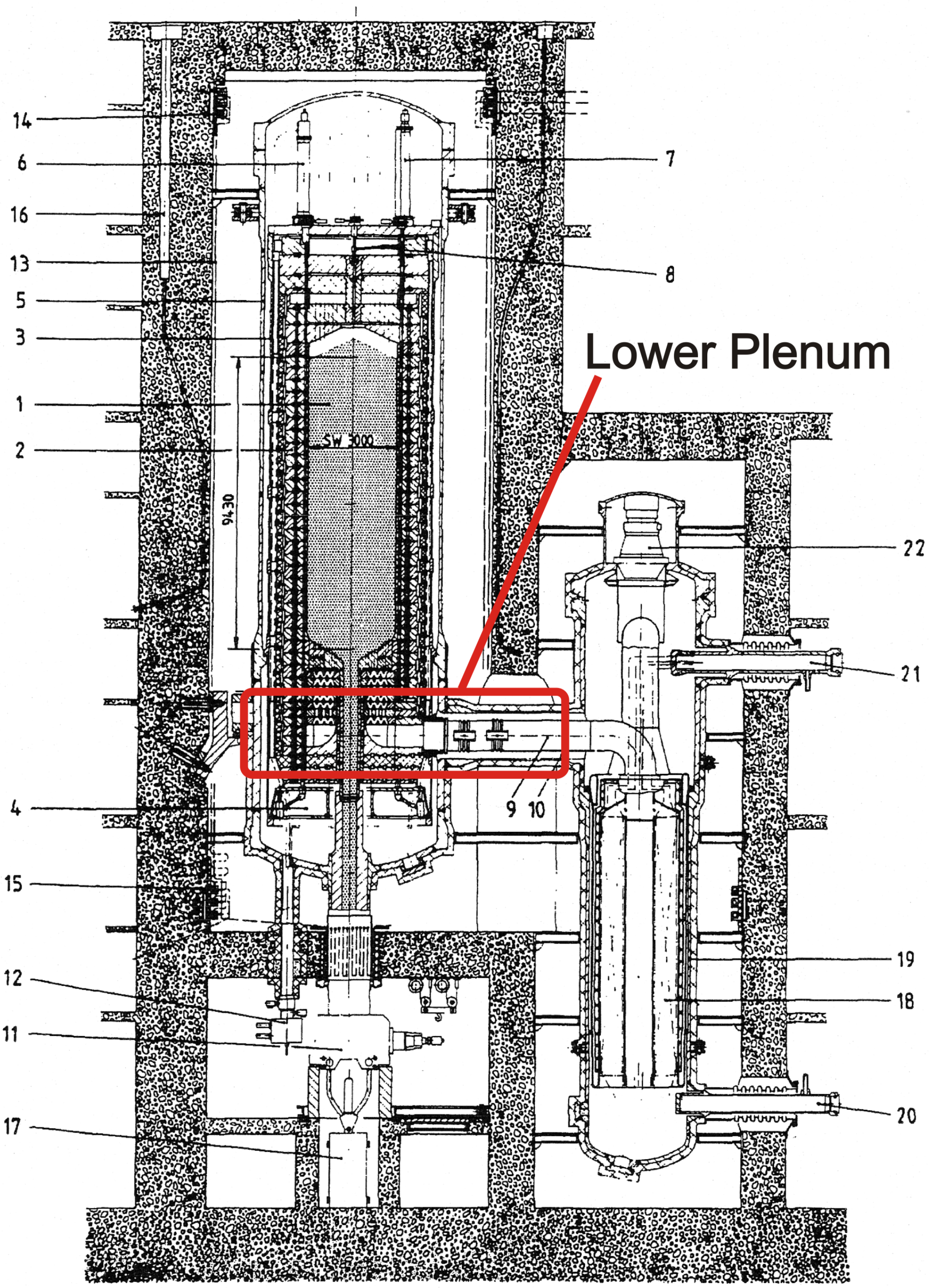

Figure 1.1: Schematic of the primary circuit of the HTR-Modul by Interatom;

(1)pebble bed reactor core, (2) graphite core, (3) core vessel, (4) core support, (5) reactor pressure vessel, (6) small absorber spheres unit, (7) reflector rod, (8) fuel element charging tube, (9) hot gas duct, (10) cold gas channel, (11) valve bank for fuel element discharge, (12) valve bank for small absorber spheres system, (13) cavity cooler, (14) return lines cavity cooler, (15) forward lines cavity cooler, (16) neutron flux instrumentation, (17) failed-fuel cask, (18) tube bundle, (19) steam generator pressure vessel, (20) feed water line, (21) live steam line, (22) blower.

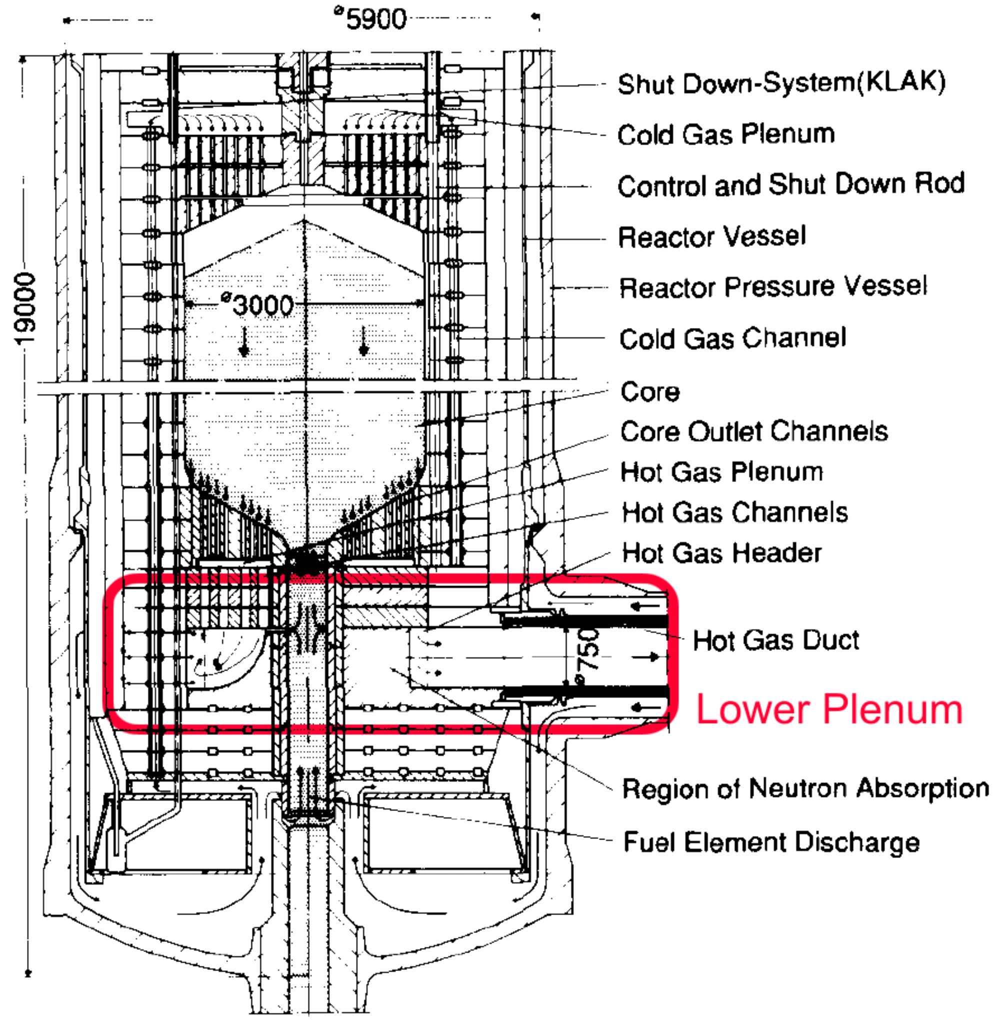

Figure 1.2: Closeup of the lower and upper plenum of the HTR-Modul design

plant, can also change the power distribution within the core significantly. Additionally, these shutters may interfere with the ability of the core to properly reject heat in the case of accident scenarios, making their use not certain before detailed safety design analysis is performed. Due to the still on-going scientific work of laying out the exact specifications of such block-type reactors, any predictions about the exact need of mixing different coolant temperatures are premature and speculative at best. With respect to pressure loss, block-type reactors have a significantly smaller pressure loss due to their smooth round coolant channels. Other flow effects, such as re-laminarization, are of greater importance and the object of scientific research for these reactors.

1.2 Experimental work

The issue of efficient gas mixing in the lower plenum was identified and investigated for the first design of a commercial pebble bed reactor, the HTR-Modul by Interatom during the mid to late 80s. After several iterations of trial-and-error, the following geometry design was proposed and published by Damm and Wehrlein in [5]:
The mixing chamber (Figure 1.3) consists of an annular ring channel which has several "ribs" orientated radially inwards. Hot gas enters the mixing chamber via inlets at the top of these ribs, which then act as a ramp to induce a strongly vortical flow to enhance mixing within the ring chamber. The ring chamber then leads to a short pipe connecting the heat exchangers or turbine with the lower plenum of the reactor.

The flow within the lower plenum consists of a highly complex vortical structure within the ring configuration. Central to the displayed flow is the positioning of the four gas inlets per "rib". The first three inlets, two hot and one cold, flow into the "rib" which acts as a sort of ramp. The fourth, also the largest inlet, acts as a wall of gas forcing the gas within the rib towards the bottom of the ring chamber and to flow around this jet. This flow motion, coupled with the out-of-center location of the fourth inlet, induces a very strongly swirling flow within the ring chamber. Due to a constant cross section of the ring chamber, this vortical motion is accelerated as more gas is added to the ring chamber with every passing "rib". The ratio of momentum in tangential direction, compared to axial direction is in excess of 2. A more detailed discussion of this flow is presented in chapter 6, Results.

Damm and Wehrlein also conducted temperature mixing experiments on a 1:2.9 scaled-down version of the lower plenum geometry of Interatom's 200MWth HTR Modul during the late 1980s. Due to cost issues, air was used as a test medium. The flow conditions were scaled according to similarity laws for equal Reynolds number and Prandtl number. Their results showed that sufficient mixing could be attained for the flow conditions tested, but due to too high Mach numbers, the experiments were only performed up to 60% equivalent full mass flow of the HTR Modul. With rising mass flow, and hence rising Reynolds number, a deterioration of mixing efficiencies could be seen, and extrapolating this

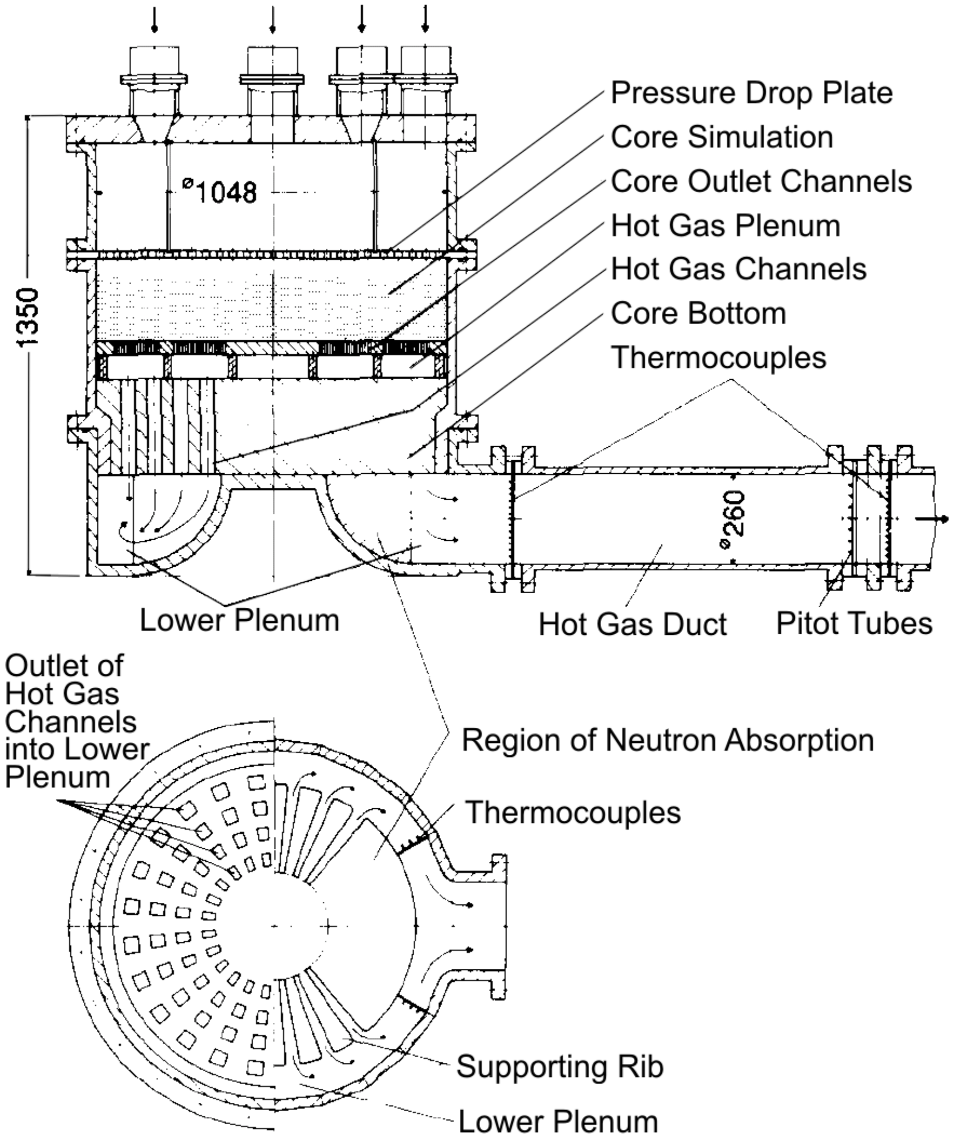

Figure 1.3: Schematic of the 1:2.9 scaled model of the hot gas mixing chamber used by Damm and Wehrlein

trend to 100% mass flow showed a high probability that the maximum 15 °C temperature difference stated in the introduction would be exceeded. Another issue with this experiment is whether the right assumptions were made for the laws of scaling with respect to replacing helium with air.

Unfortunately, these experiments do not provide an in-depth analysis of the flow structures present in this geometry. The main aim was to provide only two numbers to the nuclear licensing authorities: The mixing efficiency φ and the pressure loss measured in mbar. In addition, at the time of budgeting the design, the lower plenum was regarded as an unimportant and already solved side issue. Only toward the end of the design process was the first iteration of the lower plenum tested as an after-thought. According to lead engineers involved in the project, those experiments showed disastrous mixing efficiencies as well as pressure loss for the design. The above lower plenum design was developed in a state of utmost urgency and has to be considered as a rushed solution to a problem which nearly killed the entire HTR-Modul project.

Further experimental work on the lower plenum of pebble bed reactors can be found for the small Chinese HTR-10 Experimental reactor [8]. Four different lower plenum geometries were investigated: One identical to Damm and Wehrlein, scaled to the size of the HTR-10, a simpler geometry involving less "ribs", one with only a baffle plate at the outlet as flow restriction and lastly a completely empty lower plenum. The experimental work showed that for the case of the small 10MWth HTR-10, a simpler lower plenum geometry involving less "ribs" performed similarly to the much more intricate design of the HTR-Modul. The other two geometry variations, baffle plate and empty chamber, performed significantly worse and would have easily caused rapid damage to the steam generators due to thermal stresses. The applicability of these results for much bigger production sized HTRs is very limited since the flow velocities are two orders of magnitude below, and the temperature differences are one order of magnitude below that of future full scale designs. The operating conditions are summarized in table 1 for different pebble bed reactors as well as the lower plenum air experiments of Damm and Wehrlein.

Similar experimental work was also conducted on block type HTRs for example [9; 10; 11; 12]. In this reactor topology, the lower plenum geometry is

op. conditions	HTR-Modul	Damm Experiments	HTR-10	Unit
medium	He	air	He	–
temperature	700	40	700	^{o}C
pressure	60.0	1.3	30	bar
mass flow	85.4	6.0	4.3	kg/s
velocity HGD	65.0	80.0	70.0	m/s
Re-number	$3.2 \cdot 10^6$	$1.6 \cdot 10^6$	$6.4 \cdot 10^5$	–
Mach-number	0.03	0.27	0.02	–
Pr-numer	0.64	0.66	0.65	–

Table 1: Comparison of operating conditions for different HTR configurations.

compared to different pebble bed type reactors. The coolant channel flow enters into a hexagonally formed cavity that is interrupted by a dense matrix of round structural pillars holding the entire reactor core up. The coolant flows around these pillars and the wake influence of these pillars onto the overall flow is of great importance. Mixing occurs mostly within shear layers between different coolant jets entering the plenum and interactions with wake vortices induced by the pillars. The work by [12] is very noteworthy in this regard. The authors analyzed the lower plenum of a block type configuration using the system code Relap 5 as well as using the commercial CFD code ANSYS CFX. Their results indicated that the lower plenum could not sufficiently mix the helium jets of varying temperatures leaving the reactor core, and that hence hot streaking due to unmixed jets was observed. Any conclusions, though, have to be deferred since the thermo-neutronic analysis and design of the reactor core are not yet complete and may cause massive changes to the relevant helium coolant temperatures. In the future, block type reactors my have to use a similar lower plenum geometry as found in the HTR-Modul to sufficiently enhance mixing. In contrast to the pebble bed lower plenum, block type reactors do not exhibit large swirling flow structures enhancing mixing, and hence the relevance of that work is small for this thesis.

1.3 Previous CFD work

In [13] and [14] a rudimentary CFD analysis is performed on the simplified HTR-10 geometry as well as on the geometry of the HTR-Modul using the CFD package ANSYS CFX. In [13] the HTR-10, including the geometry variations of [8] as well as the experiments by Damm and Wehrlein were modeled. The employed turbulence model was the default k-ϵ model and the employed mesh a very coarse unstructured tetrahedral mesh. The turbulence was simply initialized with the default setting of automatically generated length scales, and all inlets were prescribed with constant normal velocities. Their results are not compared with the results of the experiments conducted on the HTR-10 air experiment, and the validation attempt for the experiments on the HTR-Modul is not convincing. The CFD simulation lacked the experimentally observed deterioration of mixing efficiency with increasing Reynolds Number, and hence the question needs to raised whether the CFD simulation managed to properly model the basic flow phenomena of swirl mixing.

The results published in [14] are nearly identical to the previous ones in [13]. More emphasis was put into the discussion of the results for the various geometry variation for the HTR-10, but any attempt of comparing these results with the experimental results in [8] could not be found. A quick comparison between these results shows that the CFD mixing efficiencies as well as pressure drop simply do not agree with the experiments. For example, the empty lower plenum had a temperature difference of approximately 11 °C, whereas the CFD value was 0.71 °C. The CFD is even predicting an improvement in mixing efficiency for geometries involving less ribs, and even better efficiencies for geometries with none at all; which stands in stark contrast to the experiments showing the reverse trend. Clearly, the need to develop a scalable and validated methodology for simulating the lower plenum in CFD has yet not been met.

1.4 Aim of the present work

One of the main problems in designing and building the pebble bed HTR is the uncertainty about the flow field in the lower plenum in general and the temperature distribution of the cooling gas (Helium) at the outflow from the collector (or - better - inflow into the power generating turbine) in particular. As will be described in more detail in chapter 2, the temperature variations about its mean value of approximately 750 °C could be as high as 210 °C. This temperature non-uniformity would be most certainly damaging to the steel components following the lower plenum. Consequently, the designer of the HTR has to achieve nearly uniform temperature distribution at the outflow from the lower plenum. This task is, however, very difficult to accomplish. The flow field is highly complex, three-dimensional, rotational, dominated by swirling flow and turbulent effects. A thorough knowledge of the flow field in question is essential for a successful design of the entire HTR-system.

The potential investigator of the flow field in the lower plenum has generally two methods to his disposal: experimental or numerical. Full scale experimental study of the lower plenum flow is very difficult, expensive, time consuming and therefore in the academic environment nearly impossible. It has been shown that all of the experiments have been carried out on model configurations. Here, the scalability of the low temperature, reduced size results is in question, as there is no unique similarity law for highly swirling flow. The previous experiments provide useful information for the validation of numerical codes and make general statements about the tendencies of the flow character possible, but they are not suitable for detailed design. The only alternative is numerical simulation of the flow in the lower plenum. In this regard, however, one must recognize that all the previous flow simulations failed even to show the correct experimentally determined tendencies and lack almost all physical relevance. The reasons for the lack of success of the previous CFD work could be many-fold, but a careful consideration of the results reveals that neither the grid resolution nor the turbulence model used were adequate.

The aim of the present work is therefore to develop a reliable and scalable method for investigating and designing the lower plenum of pebble bed type reactors with the aid of computational fluid mechanics. As the author suspects the most likely reason for the failure of the previous simulations to be an inadequate turbulence model, the main topic of this work is to develop and implement an appropriate turbulence model for the subsequent CFD simulations of the flow field in the lower plenum. The new turbulence model should be capable of modeling the physical processes of scalar mixing in strongly swirling flows accurately.

For modeling the turbulence in this type of flow, careful attention has to be paid to the correct and physically relevant closure of the turbulence effects due to the transport of momentum as well as the transport, and mixing, of enthalpy. Using the RANS approach to modeling turbulent momentum transport, a large number of studies, both experimental as well as numerical, have been performed in the past on strongly swirling confined flows. The lessons learned from this previous work indicated that simple isotropic, zero-, one- or two-equation turbulence models were insufficient and, therefore, more advanced higher order anisotropic two equation models or the full modeling of all individual Reynolds stresses was necessary. Based on experiments done in the field of swirl combustors, investigating the transport of passive scalars, it was decided to develop and implement a new turbulence model for the turbulent transport of passive scalars within the context of the commercial ANSYS CFX 11 flow simulation system of programs. The present turbulence model will be based on the direct modeling of all three turbulent scalar fluxes. Several variations of the closure model, for example algebraic formulations or the full differential transport equations, are going to be investigated in the present work.

Due to the low Mach number gas velocities in the lower plenum of the HTRs as well as their corresponding reduced size air experiments, the flow can be considered to be weakly compressible and hence during the development of concepts for the transport of temperature the problem can be treated as that of a passive scalar. The present approach for the turbulence modeling will to be validated using several simpler flow cases. Based on these validated turbulence models, the lower plenum geometry of Damm and Wehrlein's experimental work will be thoroughly investigated with special consideration given to the development of an understanding of the flow. Particular emphasis will be given to the investigation of the scaling of mixing with varying Reynolds numbers. Based on the results of these investigations, it is hoped to offer proposals for modifications and improvements to the lower plenum design, thus improving the ability to perform numerical fluid mechanics simulations on this type of geometry in particular and strongly swirling mixing flows with temperature gradients in general.

Chapter 2

Physical description of investigated configuration

The lower plenum of pebble bed HTRs is a complex three-dimensional structure facilitating the collection and mixing of helium of varying temperatures as it exits the reactor core situated above. The reader is referred to previous figures 1.1 and 1.2 for more details about the general reactor topology for the pebble bed reactors of interest. The pebble bed column within the reactor does not generate heat uniformly, instead, there is a maximum of power generation along the center of rotation and the power generation density falls off toward the outer graphite reflector blocks. Because of the very small point contact area between neighboring fuel spheres, heat conduction is very poor within the pebble bed despite the excellent heat conduction capabilities of graphite. In addition, the helium coolant gas which is flowing downwards through the pebble bed does not exhibit any significant movement or mixing in the horizontal direction. Both effects combined cause the solid part of the core, consisting of fuel pebbles as well as the moderator, and the helium gas coolant to have a very inhomogenous distribution of temperature. For more information about the reactor core itself, and different configurations, the reader is referred to the work by BenSaid [7] and [15]. The most promising configuration of the reactor core (cylindrical core with no central column) will cause a radial helium temperature profile at the exit of the core with a temperature difference of approximately 200 to 230 °C around the mean of approximately 750 °C. Another source of temperature differences and hence the need for mixing arises from leakage flows of the cold reactor inlet gas of approximately 350 °C leaking through gaps between the graphite moderator blocks.[1] In terms of total mass-flow, this leakage flow is very small given the relatively small pressure differential of about 0.5bar and the long length of travel (about 75cm) between the small graphite block gaps (in the range of a few millimeters).

Downstream of the mixing plenum are various steel components such as piping in the steam generators as well as a hypothetical helium turbine in the power generating part of the reactor. At the elevated temperatures found in the present configuration, the tensile strength of steel rapidly decreases with rising temperatures, leading to a significant requirement to reduce any temperature fluctuations or differences in the outlet stream to reduce thermal stresses and to prolong the service life of all components. Industry sources tasked with developing these components often stated the need to have temperature differences of at most 10-15 °C [5]. This task of mixing the hot helium gases needs to be adequately achieved by the lower plenum of the reactor.

2.1 Lower plenum geometry and flow

The lower plenum, as designed by Interatom and Siemens for the HTR-Modul, and published by Damm and Wehrlein [5], consists of several "ribs" aligned radially outwards from the center of rotation of the reactor pressure vessel. Into each of these ribs there are four round inlets, with the hottest helium entering at the inlet closest to the center of rotation, and the coldest helium entering closest to the reactor pressure vessel. These gases flow through the ribs into a square annular collection chamber which empties into a short round hot gas duct leading to the power generation unit of the reactor. While not directly a part of the lower plenum, the system of channels between the reactor core and the lower plenum cavity has to be considered, too. The channel system consists of long vertical holes drilled into the bottom reflector of the reactor, leading to several annular collection chambers situated directly above the previously mentioned four round inlet holes. The task of this network is to prevent any unsymmetrical feedback effects caused by the lower plenum on to the reactor core flow, see figures 2.1 and 2.2 for the general design of the lower plenum geometry investigated by Damm and Wehrlein in their experiments.

---

[1] Graphite at hot temperatures will contract under neutron bombardment from the nuclear fission reactions in the reactor, causing gaps to form between the blocks with time

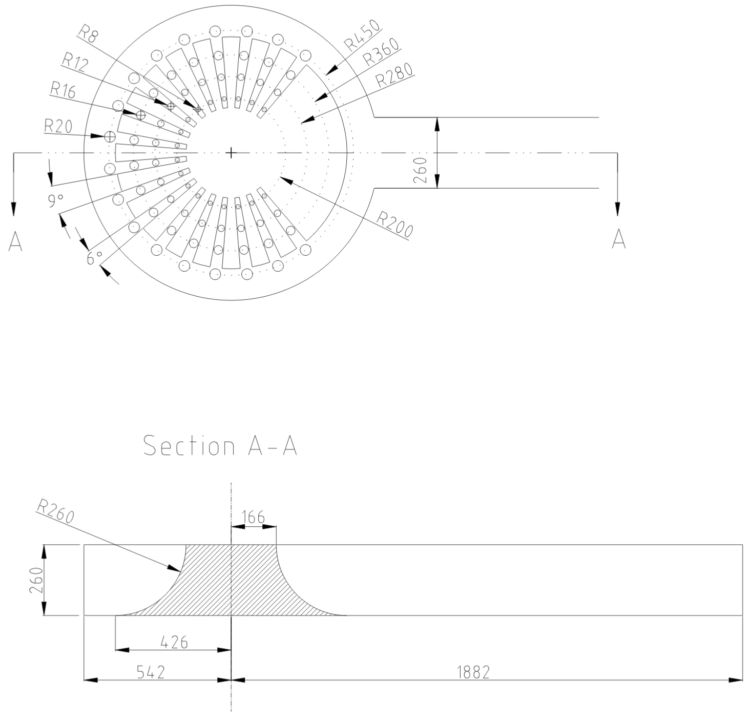

Figure 2.1: Design drawing of the lower plenum of the reduced-size air experminets of Damm and Wehrlein

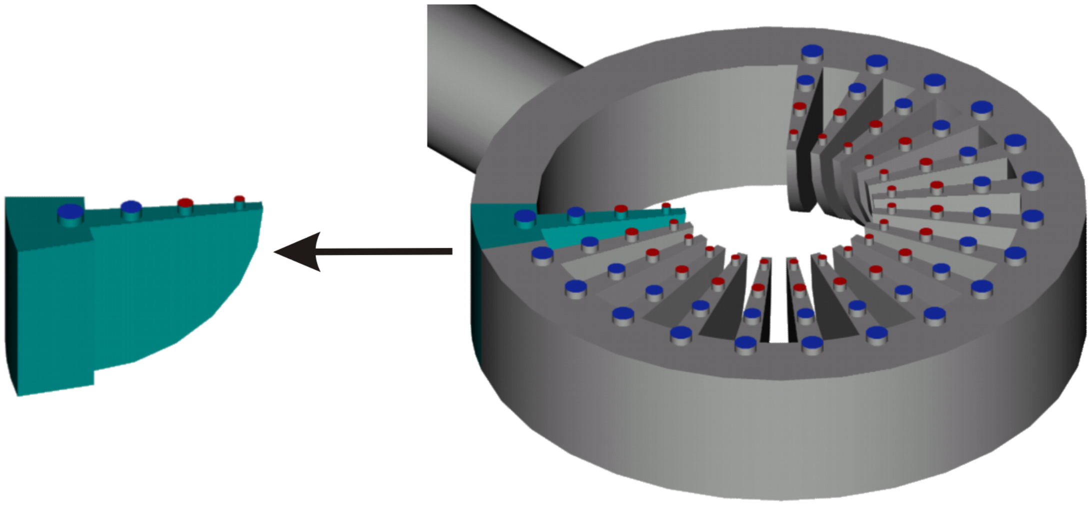

Figure 2.2: Cutaway view of a single space between the "ribs"

The flow within the lower plenum consists of a highly complex vortical structure within the ring enclosure. Central to the displayed flow is the positioning of the four gas inlets per “rib”. The first three inlets, two hot and one cold, flow into the space between the “ribs” which acts as a sort of ramp. The fourth, and also the largest inlet acts as a wall of gas forcing the gas within the rib towards the bottom of the ring chamber and to flow around this jet. This flow motion, coupled with the out-of-center location of the fourth inlet, induces a very strongly swirling flow within the ring chamber, see figures 2.3 and 2.4 . Due to a constant cross section of the ring chamber, the vortical motion is accelerated as more gas is added to the ring chamber with every passing “rib”. The ratio of momentum in tangential direction, compared to axial direction, called Swirl number S (eqn. 2.1) is in excess of 2.

$$S \equiv \frac{\int_0^{R_o} uwr^2dr}{R_o\int_0^{R_o} u^2rdr} \tag{2.1}$$

2.2 Mathematical model

The flow field to be simulated is characterized by the following properties: three-dimensional, unsteady, viscous, turbulent, weakly compressible or incompressible with variable density. The unsteady motion of continuum fluid in three dimensions can be described by the following equations for conservation of mass, momentum and energy [16].

Continuity of mass:

$$\frac{\partial\rho}{\partial t} + \frac{\partial\rho\, u_i}{\partial x_i} = 0 \tag{2.1}$$

Momentum equations:

$$\rho\frac{\partial u_i}{\partial t} + \rho u_i\frac{\partial u_j}{\partial x_j} = \frac{\partial p}{\partial x_i} + \frac{\partial\sigma_{ij}}{\partial x_j} \tag{2.2}$$

$$\text{where } \sigma_{ij} = \mu\left(\frac{\partial u_i}{\partial x_j} + \frac{\partial u_j}{\partial x_i} - \frac{2}{3}\frac{\partial u_k}{\partial x_k}\delta_{ij}\right) \tag{2.3}$$

Energy equation:

$$\frac{\partial\rho h}{\partial t} + \frac{\partial u_i\rho h}{\partial x_i} = \frac{Dp}{Dt} + \frac{\partial}{\partial x_i}\left(\lambda\frac{\partial T}{\partial x_i}\right) + \bar{\bar{\tau}}..\,\bar{\bar{\dot{\epsilon}}} \tag{2.4}$$

where ρ is the density, p static pressure, h static enthalpy, t time, $\vec{v}$ the

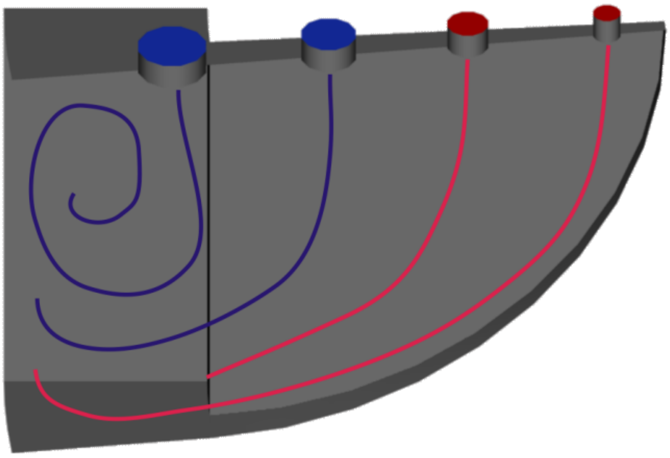

Figure 2.3: Picture of the flow within a single rib

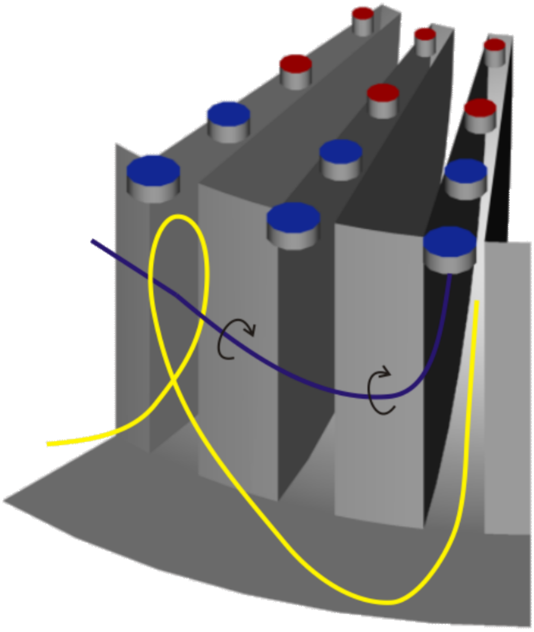

Figure 2.4: Picture of the strong swirl within the square annular collection chamber

velocity vector, $\overline{\overline{\dot{\epsilon}}}$ the rate of strain tensor and $\overline{\overline{\tau}}$ the stress tensor. The above conservation equations are based on following assumptions:

- the fluid can be treated as a continuum
- the stress rate of strain relationship is according to Newton's fluid

It has been pointed out in chapter 2.1 that the presently investigated flow can be assumed to be incompressible with variable density. The density is in this case independent of pressure; it is, however, a strong function of temperature. The ideal gas equation of state is in this case not valid. Instead, the modified equation of state due to Redlich and Kwong [17] was implemented in the code. It is given by:

$$p = \frac{RT}{v-b+c} + \frac{a(T)}{v(v+b)} \tag{2.5}$$

where a, b and c are obtained from

$$a = a_0 \left(\frac{T}{T_c}\right)^{-n} \tag{2.6}$$

$$a_0 = \frac{0.42747 R^2 {T_c}^2}{p_c} \tag{2.7}$$

$$b = \frac{0.08664 R T_c}{p_c} \tag{2.8}$$

$$c = \frac{R T_c}{p_c + \frac{a_0}{v_c(v_c+b)}} + b - v_c \tag{2.9}$$

$$\tag{2.10}$$

The standard value of $n = 0.5$ has been replaced in the CFX-program by a general variable exponent. All variables with the subscript c denote variable values at the critical point. The interested reader is referred to the CFX-Manual [17] for further details.

The above conservation equations can be cast in compact integral form in terms of functional vectors Q and H as:

$$\int_\tau \frac{\partial Q}{\partial t} d\tau + \oint_A H \cdot \vec{n}\, dA = S \qquad \text{mit} \qquad Q = (\rho, \rho u, \rho v, \rho w, e)^T. \tag{2.11}$$

The vector Q consists of the so called conservative variables ρ (specific mass), $\rho\vec{v}$ (specific momentum) and e (volume specific total energy). The generalized flux vector H contains the inviscid convective terms, the pressure terms and the viscous terms. Using the Gauss theorem, the integral form can be transfered into the divergence form:

$$\frac{\partial Q}{\partial t} + \overrightarrow{\nabla} \cdot H = 0. \tag{2.12}$$

the above equation is in Cartesian coordinates:

$$\frac{\partial Q}{\partial t} + \frac{\partial (F - F_v)}{\partial x} + \frac{\partial (G - G_v)}{\partial y} + \frac{\partial (H - H_v)}{\partial z} = 0, \tag{2.13}$$

with the inviscid terms F, G and H and the viscous terms F_v, G_v and H_v. In more detail, the fluxes are in Cartesian coordinates:

$$Q = \begin{pmatrix} \rho \\ \rho\, u \\ \rho\, v \\ \rho\, w \\ e \end{pmatrix}, \quad F = \begin{pmatrix} \rho u \\ \rho u^2 + p \\ \rho u v \\ \rho u w \\ (e+p)u \end{pmatrix},$$

$$G = \begin{pmatrix} \rho v \\ \rho u v \\ \rho v^2 + p \\ \rho v w \\ (e+p)v \end{pmatrix}, H = \begin{pmatrix} \rho w \\ \rho w u \\ \rho w v \\ \rho w^2 + p \\ (e+p)w \end{pmatrix}, \tag{2.14}$$

with the viscous fluxes:

$$F_v = \begin{pmatrix} 0 \\ \sigma_{xx} \\ \sigma_{yx} \\ \sigma_{zx} \\ \Omega_x \end{pmatrix} ,$$

$$G_v = \begin{pmatrix} 0 \\ \sigma_{xy} \\ \sigma_{yy} \\ \sigma_{zy} \\ \Omega_y \end{pmatrix} ,$$

$$H_v = \begin{pmatrix} 0 \\ \sigma_{xz} \\ \sigma_{yz} \\ \sigma_{zz} \\ \Omega_z \end{pmatrix} . \tag{2.15}$$

The elements of the viscous fluxes that appear in the energy equation are:

$$\begin{aligned} \Omega_x &= \sigma_{xx}\, u + \sigma_{xy}\, v + \sigma_{xz}\, w - q_x , \\ \Omega_y &= \sigma_{xy}\, u + \sigma_{yy}\, v + \sigma_{yz}\, w - q_y , \\ \Omega_z &= \sigma_{xz}\, u + \sigma_{yz}\, v + \sigma_{zz}\, w - q_z , \end{aligned} \tag{2.16}$$

the components of the deviatoric stress tensor σ_{ij} can be written as:

$$\sigma_{ij} = -\frac{2}{3}\mu\frac{\partial u_k}{\partial x_k}\delta_{ij} + \mu\left(\frac{\partial u_i}{\partial x_j} + \frac{\partial u_j}{\partial x_i}\right) , \tag{2.17}$$

with the Kronecker delta δ_{ij} . The above equations were formulated using the Stokes hypothesis:

$$\lambda = -\frac{2}{3}\,\mu . \tag{2.18}$$

and the heat conduction vector was obtained from the Fourier law:

$$q_i = k\frac{\partial T}{\partial x_i} . \tag{2.19}$$

The above system of equations represents five equations for seven unknown flow variables (ρ, u, v, w, e, p, T) . For a proper mathematical closure, two more equations are necessary. One of them is the already mentioned equation of state with the specific gas constant R. The caloric equation of state, known from thermodynamic considerations, is the last necessary equation:

$$e_i = c_v T, \tag{2.20}$$

with the internal energy e_i and the specific heat capacity c_v for constant volume. Finally, the following form of the equation of state is highly useful:

$$p = (\kappa - 1)\left[e - \frac{1}{2}\rho\left(u^2 + v^2 + w^2\right)\right] \tag{2.21}$$

with κ being the ratio of the two specific heat coefficients. For general compressible fluid, the above equations are all coupled. The requirement of global conservation of flow properties, necessary for the correct simulation of discontinuities, makes the implementation of the full conservation form imperative.

Given proper grid resolution, the governing equations are capable of directly simulating turbulent effects. This is, however, only in very few selected cases practically possible. Mostly, a time-averaged form of the Navier-Stokes equations, the so called Reynolds-Averaged-Navier-Stokes equations (RANS) is used. The details of the implementation of this procedure and the selection of the appropriate closure models will be discussed in chapter 3.

In the present case, the flow is incompressible or weakly compressible, meaning that the energy equation is coupled to the momentum and continuity equations only by the dependency of the coefficient of dynamic viscosity on the temperature. The energy equation can be, therefore, considered as decoupled from the momentum and continuity equations.

Chapter 3

Treatment of turbulence

3.1 Selection of turbulence models

Fundamental to correctly simulating the flow of the lower plenum is the issue of turbulence modeling, and in particular the modeling of turbulent mixing of gases with varying temperatures. Previous CFD work published on the plower plenum by Tsingtao university ([13], [14]) did not infer confidence in the abilities of the used isotropic k-ϵ turbulence model to generate physically sound results. Clearly, more thought has to be given to the selection of an appropriate turbulence model, and the default models in the CFX program are not sufficient.

For modeling turbulence in CFD, generally three approaches can be identified which are scientifically well developed: Direct numerical simulation (DNS), spatial filtering techniques which are called large eddy simulation (LES) and lastly statistical filtering techniques such as Reynolds Averaging. A DNS applied to this very large geometry coupled with a Reynolds number (based on the outlet pipe diameter) of the order of a million would necessitate computational resources which are well outside of any practical considerations. The complex flow conditions within the lower plenum, with its many vortex structures interacting with each other, would make an LES approach to modeling turbulence very attractive. Rule of thumb estimations for the necessary grid size (+100 million cells) as well as time steps of the order of $10^{-6}s$, with an average flow residence time of $0.14 - 0.20s$, would result in too high computational needs for at least the next decade given recent developments in computational power. One is hence left with statistical methods such as Reynolds averaging or Favre averaging for modeling turbulence. The following section will discuss and identify among the class of statistical methods for turbulence treatment suitable turbulence models for flow within the lower plenum of pebble-bed HTRs.

3.2 Time averaged transport equations

Statistical averaging techniques employed in CFD for modeling turbulence revolve around the idea of Reynolds averaging and the following variable decomposition (for more detail see e.g. [16] or [18]): given an instantaneous tensorial quantity Φ of a fluid, it can be split into a mean time-averaged part $\overline{\Phi}$ and an instantaneous turbulent fluctuating part Φ', ie. a temporal filter is being applied to all dependent variables.

$$\Phi(x,t) = \overline{\Phi}(x) + \Phi'(x,t) \tag{3.1}$$

where $\overline{\Phi}$ is formally defined as

$$\overline{\Phi} = \lim_{T\to\infty} \frac{1}{T} \int_{t_0}^{t_0+T} \Phi dt \tag{3.2}$$

Inserting eqn. 3.1 into the generalised Navier-Stokes-Equations (eqn. 2.1 + eqn. 2.2) for all dependent variables u_i, p, and assuming $\rho \neq f(t)$, yields the following Reynolds Averaged Navier-Stokes equations (commonly called RANS)

$$\frac{\partial \rho}{\partial t} + \frac{\partial \rho \overline{u_i}}{\partial x_i} = 0 \tag{3.3}$$

$$\frac{\partial \rho \overline{u_i}}{\partial t} + \frac{\partial}{\partial x_j} \left(\rho \overline{u_i u_j}\right) = -\frac{\partial \overline{p}}{\partial x_i} + \frac{\partial}{\partial x_j} \left[\sigma_{ij} + \rho \overline{u_i' u_j'}\right] \tag{3.4}$$

$$\text{where } \sigma_{ij} = \mu \left(\frac{\partial \overline{u_i}}{\partial x_j} + \frac{\partial \overline{u_j}}{\partial x_i} - \frac{2}{3} \frac{\partial \overline{u_k}}{\partial x_k} \delta_{ij} \right) \tag{3.5}$$

The same can be done with the energy equation (eqn. 2.4)

$$\frac{\partial \rho \overline{h_0}}{\partial t} - \frac{\partial \overline{P}}{\partial t} + \frac{\partial \rho \overline{u_i} \overline{h_0}}{\partial x_i} = \frac{\partial}{\partial x_i} \left(\lambda \frac{\partial}{\partial x_i} \overline{T} \right) - \frac{\partial \rho \overline{u_i' h_0'}}{\partial x_i} + \frac{\partial}{\partial x_i} \left(\overline{u_i \sigma_{ij}} \right) \tag{3.6}$$

Formally, all $\partial\overline{\Phi}/\partial t = 0$ of an arbitrary tensor Φ, if the limiting case of $t \rightarrow \infty$ is a valid assumption to a flow, but in cases of unsettled, transient, or unsteady flows, it is possible that $\partial\overline{\Phi}/\partial t \neq 0$ for an arbitrary point in Eulerian space. For such flows, it is assumed that T is sufficiently large compared to the statistical time scales of turbulence, and hence $\partial\overline{\Phi}/\partial t$ terms can be part of the transport equations. These equations are called the unsteady Reynolds-averaged Navier-Stokes equations (URANS), alternatively it is sometimes called very large eddy simulation (VLES) in literature. For the case of the lower plenum flow, there is no indication that the assumption of the flow being steady is valid. There are many sharp edges where separation might occur and the vortex interaction with the inlet jets of each rib is very likely itself unsteady. Hence, all equations formulated here will be dependent on time, too.

The above URANS equations are based upon the assumption that $\rho \neq f(t)$ for an arbitrary point in space. This assumption is too simplistic for the case of incompressible flows with variable density. Applying the Reynolds decomposition also onto the instantaneous density ρ leads to several unknown density variation terms in the case of time averaging over any convective product ($\rho\Phi u_i$) of a tensorial quantity Φ :

$$\overline{\rho\Phi u_i} = \underbrace{\overline{\rho}\,\overline{\Phi}\,\overline{u_i}}_{I} + \underbrace{\overline{\rho'\Phi'}\,\overline{u_i}}_{II} + \underbrace{\overline{\rho' u_i'}\,\overline{\Phi}}_{III} + \underbrace{\overline{\rho}\,\overline{\Phi' u_i'}}_{IV} + \underbrace{\overline{\rho'\Phi' u_i'}}_{V} \tag{3.7}$$

Terms I and IV are the same terms as with standard Reynolds decomposition and averaging, but terms II, III and V are new unknown turbulent density correlations that would need to be closed with new turbulence models. In order to reduce the required number of closure terms, several simplifying approximations to the above equations have been proposed. One approach is the so-called binary regrouping where eqn. 3.7 is simplified to two terms, identical in form to Reynolds averaging consisting of one mean value based term ($\overline{\rho}\,\overline{\Phi}\,\overline{u_i}$ and one term with turbulent fluctuating values which needs to be closed by a turbulence model. The most common binary regrouping method is based on Favre density weighted averaging [19], which will be gone into more detail later on. Other binary regrouping methods split the terms of eqn. 3.7 into a Reynolds averaged advection part, and a mass-weighted averaged convective part, for more details see Chassaing [20] and HaMinh et al. [21] Ternary regrouping methods have also been proposed by Chassaing [20], but use of this method has been very limited so far.

The formal definition of a density weighted "Favre-time average" is as follows:

$$\frac{\overline{\rho\Phi}}{\overline{\rho}} = \frac{1}{\overline{\rho}} \lim_{T\to\infty} \frac{1}{T} \int_{t_0}^{t_0+T} \rho(x,t)\Phi(x,t)dt \tag{3.8}$$

Introducing a new "Favre-average" operator "$\widetilde{\quad}$" reduces the above relation to a more compact form of

$$\frac{\overline{\rho\Phi}}{\overline{\rho}} = \widetilde{\Phi} \tag{3.9}$$

An instantaneous quantity Φ can hence be "Favre-decomposed" into a "Favre average" and a new turbulent fluctuating part

$$\Phi = \widetilde{\Phi} + \Phi'' \tag{3.10}$$

It should be noted that

$$\begin{aligned} \overline{\rho}\widetilde{\Phi} &= \overline{\rho\Phi} \\ \text{inserting } 3.10: \quad &= \overline{\rho\widetilde{\Phi}} + \overline{\rho\Phi''} && (3.11) \\ &= \overline{\rho}\widetilde{\Phi} + \overline{\rho\Phi''} && (3.12) \end{aligned}$$

The paradox in eqn. 3.11 can only be solved by acknowledging that Favre-averaging implicitly assumes that

$$\begin{aligned} \overline{\rho\Phi''} &= 0 \\ &= \overline{\overline{\rho}\Phi''} + \overline{\rho'\Phi''} && (3.13) \end{aligned}$$

Eqn. 3.13 allows for sweeping simplifications to the earlier posed problem of variable density advection of an arbitrary tensor Φ in turbulent flows (3.7). Favre-decomposing (eqn. 3.10) Φ and u_i and Reynolds-decomposing ρ yields

$$\begin{aligned} \overline{\rho u_i\Phi} &= \overline{(\overline{\rho}+\rho')(\widetilde{u}_i+u_i')\left(\widetilde{\Phi}+\Phi''\right)} \\ &= \underbrace{\overline{\rho'}\widetilde{u}_i\widetilde{\Phi}}_{=0} + \underbrace{\overline{\rho'\Phi''}\widetilde{u}_i + \overline{\overline{\rho}\Phi''}\widetilde{u}_i}_{=0} + \overline{\rho}\widetilde{u}_i\widetilde{\Phi} + \underbrace{\overline{\overline{\rho}u_i''}\widetilde{\Phi} + \overline{\rho' u_i''}\widetilde{\Phi}}_{=0} + \overline{\rho' u_i''\Phi''} + \overline{\overline{\rho}u_i''\Phi''} \\ &= \overline{\rho}\widetilde{u}_i\widetilde{\Phi} + \overline{\rho u_i''\Phi''} \\ &= \overline{\rho}\widetilde{u}_i\widetilde{\Phi} + \overline{\rho}\widetilde{u_i''\Phi''} && (3.14) \end{aligned}$$

At first sight, eqn. 3.14 looks nearly identical to a Reynolds decomposed convective term with constant density, however, the following points should be emphasized:

- The mean velocities of variable density flows are not defined in the same way as in the case of constant density flows. Hence, the mean strain rate, the mean vorticity etc. are not physically identical between both cases. A point which should be taken into consideration when using these properties later on as arguments for turbulence closure schemes.
- Favre fluctuations are not centered:

  $$\overline{\Phi''} = \overline{\rho\Phi'}/\overline{\rho} \neq 0 \tag{3.15}$$

  Thus closure schemes for quantities such as $\overline{u_i''u_j''}$ would need to be carefully chosen, having the ability to model such unsymmetric behavior.

Inserting the above Favre identities into the standard transport equations for mass continuity, momentum and total enthalpy (eqn. 2.1, 2.2, 2.4) results in the equations below, for more details on the derivation the reader is referred to the original works of Favre or Chassaing.

$$\frac{\partial \overline{\rho}}{\partial t} + \frac{\partial \overline{\rho}\widetilde{u}_i}{\partial x_i} = 0 \tag{3.16}$$

$$\begin{aligned} \overline{\rho}\frac{\partial \widetilde{u}_i}{\partial t} + \overline{\rho}\widetilde{u}_i\frac{\partial \widetilde{u}_j}{\partial x_j} &= -\frac{\partial \overline{P}}{\partial x_i} - \frac{\partial}{\partial x_j}\left(\overline{\rho}\widetilde{u_i''u_j''}\right) + \frac{\partial \overline{\sigma_{ij}}}{\partial x_j} \\ \text{where } \overline{\sigma_{ij}} &= \overline{\mu\left(\frac{\partial u_i}{\partial x_j} + \frac{\partial u_j}{\partial x_i}\right)} - \frac{2}{3}\delta_{ij}\mu\overline{\frac{\partial u_k}{\partial x_k}} \end{aligned} \tag{3.17}$$

$$\begin{aligned} \overline{\rho}\frac{\partial \widetilde{h}_0}{\partial t} - \underbrace{\frac{\partial \overline{P}}{\partial t}}_{I} + \overline{\rho}\widetilde{u}_i\frac{\partial \widetilde{h}_0}{\partial x_i} &= \frac{\partial}{\partial x_i}\left(\lambda\frac{\partial}{\partial x_i}\left(\widetilde{T} + \overline{T''}\right)\right) - \frac{\partial \overline{\rho}\widetilde{u_i''h_0''}}{\partial x_i} \\ &\quad + \underbrace{\frac{\partial}{\partial x_i}\left(\widetilde{u}_i\widetilde{\tau_{ij}} + \overline{u_j''\tau_{ij}} + \widetilde{u}_j\overline{\tau_{ji}''}\right)}_{II} \end{aligned} \tag{3.18}$$

For the case of weakly compressible flows, pressure work (term I) as well as viscous work (term II) can be neglected in the energy equation. I should be noted that due to density weighted averaging the $\overline{T''}$ term within the laminar diffusion term is not zero and would need in theory to be closed via a turbulence model. For most flows $\overline{T''} \ll \widetilde{T}$, and hence the energy eqn. (3.18) can be reduced to the general transport equation of a passive scalar φ:

$$\overline{\rho}\frac{\partial \widetilde{\varphi}}{\partial t} + \overline{\rho}\widetilde{u}_i\frac{\partial \widetilde{\varphi}}{\partial x_i} = \frac{\partial}{\partial x_i}\left(\Gamma\frac{\partial \widetilde{\varphi}}{\partial x_i}\right) - \frac{\partial \overline{\rho}\widetilde{u_i''\varphi''}}{\partial x_i} \tag{3.19}$$

The above transport equations contain unknown terms arising from turbulence, which need to be closed via separate equations. The momentum equation (3.17) contains the term $\overline{\rho}\widetilde{u_i''u_j''} = \sigma_{ij}^{Re}$, which is commonly called the Reynolds stress tensor. The scalar transport equation (3.19) contains the term $\overline{\rho}\widetilde{u_i''\varphi''}$, called the turbulent flux of a passive scalar. The following chapters 3.3 and 3.4 will discuss closure strategies for these terms respectively.

3.3 Transport of momentum in swirling turbulent flows

The term $\overline{\rho}\widetilde{u_i''\varphi''}$ (Reynolds stress tensor) is unknown and has to be closed via a turbulence model. The classical approach to closing this term is via the linear eddy viscosity assumption. The generation as well as dissipation of turbulence is based on the assumption of a linear relationship between the fluid shear rates and an assumed virtual turbulent viscosity μ_t:

$$\tau_{ij}^{re} = \mu_t\left(\frac{\partial \overline{u_i}}{\partial x_j} + \frac{\partial \overline{u_j}}{\partial x_i}\right) - \frac{2}{3}k\delta_{ij} \tag{3.20}$$

$$\text{with} \quad k = 1/2\widetilde{u_i''u_i''} \tag{3.21}$$

This closure is commonly called the Boussinesq-approximation in turbulence modeling literature. It allows for the reduction of the six unknown Reynolds Stresses to one unknown term μ_t, called the eddy viscosity, needing closure modeling. The most prominent representatives of this class of turbulence models is the k-ϵ [22] or k-ω [23] model based on expressing μ_t as a linear function of two new transport variables: turbulent energy, usually the turbulent kinetic energy

k, and a scale of turbulent dissipation, either a length scale ϵ or a time scale Ω.

$$\mu_t = \rho C_\mu \frac{k^2}{\epsilon} \text{ or } \mu_t = \rho \frac{k}{\Omega} \tag{3.22}$$

These models offer numerical stability, fast convergence and most importantly a wide field of application to many flows. However, in the case of flows with strong streamline curvature, such as highly swirling or vortical flows, these models produce poor results. This is well known in the field of turbulence modeling and has been already stated by Launder [24] in 1976, and more recent publications (e.g. see Jakirlic [25] [26] or Jones [27]) state this as a fact without any references. Two-equation models perform poorly in swirling flow due to the anisotropic production as well as destruction of turbulence along a streamline with strong curvature. This results in an over prediction of turbulent momentum diffusion, over dampening vorticity in swirling flows. Given the pretext of time averaging turbulence, there are two approaches to model this anisotropic behavior: non-linear eddy viscosity concepts or second order models solving the individual Reynolds stresses $\overline{\rho}\widetilde{u_i''\varphi''}$ directly.

Non-linear eddy viscosity concepts rely on a polynomial expansion of the μ_t modeling term. The majority of these models are based on quadratic expansions. Due to many possible methods of defining the constants of these expressions, the proposed and implemented quadratic schemes are too numerous to be listed in completeness. For a short, but still incomplete, up-to-date overview the reader is referred to Jones [27]. A number of cubic expansions have been proposed, e.g. [28; 29; 30], but Abdon and Sunden [30] have shown that a higher order than quadratic has very little influence on results for most practical flows if the modeling coefficients are chosen to reflect streamline curvature effects. The critical point to non-linear models is in general the determination of the model coefficients. These can have a significantly greater impact on model performance than the order or type of expansion chosen for the underlying non-linear model. Compliance with formal limiters such as realizability, Schwartz's inequality and other criteria borrowed from thermodynamics, often not rigorously enforced in above models. Weigand et al. [31] for example recognized that an inappropriate choice of model coefficients can have profound effects such as switching the nature of the modeled equations from parabolic to hyperbolic. A recently proposed model by Jones and Lentini [27] has been developed to take all of these limiters as well as Favre-averaging into account. While the results are a significant improvement over several previous non-linear eddy viscosity models, their model is still found to be lacking under strong swirl compared to Reynolds stress models (RSM).

An intermediate step between full transport equations 3.23 for all individual Reynolds stresses $\widetilde{u_i''u_j''}$ and non-linear eddy viscosity models are algebraic Reynolds stress models. Since gradients of the Reynolds stresses only appear in the rate of change, convection and diffusion terms of the Reynolds stress transport equations, one can derive an algebraic expression by eliminating these expressions via model approximations. The most common one was proposed by Rodi [32] by assuming that the transport of $\widetilde{u_i''\varphi''}$ is proportional to the transport of k, and obviously neglecting the rate of change term by assuming steady state flow. The resulting expression is an implicit algebraic expression that has been known to offer (see e.g. [33]) very poor convergence to numerical solutions. An explicit algebraic stress model can be developed by adopting a non-linear dependence of $\widetilde{u_i''\varphi''}$ on k which is then transformed by an appropriate tensor basis to recover an explicit non-linear expression. Due to the nature of the full tensor basis, the five individual terms may result in singular expressions in some situations, which requires a regularization of the expression for the stresses. This and other realizability constraints are the object of current research and the reader is referred to for example Weis and Hutter [34] for further details.

The most complex option to closing $\widetilde{u_i''u_j''}$ is by solving differential transport equations for all six Reynolds stresses individually. These models are called Reynolds stress models, or short RSM. For the case of flows with constant density, the derivation of the relevant equations is straightforward and can be looked up for example in [18]. Unfortunately, this is not the case for the Favre-averaged form of these equations and multiple sources in literature contradict each other in some details of these equations. To remove this confusion, the Reynolds stress transport equations have been derived in Appendix A.1:

$$\underbrace{\overline{\rho}\frac{\partial \widetilde{u_i''u_j''}}{\partial t}}_{\text{rate of change}} + \underbrace{\overline{\rho}\widetilde{u}_k\frac{\partial \widetilde{u_i''u_j''}}{\partial x_k}}_{\text{convection}} = \underbrace{-\overline{\rho}\widetilde{u_j''u_k''}\frac{\partial \widetilde{u}_i}{\partial x_k} - \overline{\rho}\widetilde{u_i''u_k''}\frac{\partial \widetilde{u}_j}{\partial x_k}}_{\text{production}}$$

$$+ \underbrace{\frac{\partial}{\partial x_k}\left[\overline{\rho}\widetilde{u''{}_i u''{}_j u''{}_k} \; + \; \overline{p' u''{}_i}\delta_{jk} + \overline{p' u''{}_j}\delta_{ik} - \overline{u''_i \sigma_{jk}} - \overline{u''_j \sigma_{ik}}\right]}_{\text{diffusion}} \tag{3.23}$$

$$\underbrace{- \overline{u''_j}\frac{\partial \overline{p}}{\partial x_i} - \overline{u''_i}\frac{\partial \overline{p}}{\partial x_j}}_{\text{density-velocity covariance}} \quad \underbrace{+ \; \overline{p'\left(\frac{\partial u''{}_i}{\partial x_j} + \frac{\partial u''{}_j}{\partial x_i}\right)}}_{\text{pressure strain-rate correlation}} \quad \underbrace{- \; \overline{\sigma_{ik}\frac{\partial u''_j}{\partial x_k}} - \overline{\sigma_{jk}\frac{\partial u''_i}{\partial x_k}}}_{\text{viscous dissipation}}$$

The main difference between the Favre-averaged and Reynolds-averaged form of the Reynolds stress transport equations is in the absence of the density-velocity covariance term for Reynolds-averaging and slightly different forms for all viscous dissipation terms. The rate of change, convection and production terms can be calculated directly and do not need be closed via model assumptions. The diffusion term, velocity covariance term, pressure velocity-gradient term and the viscous dissipation term on the other hand contain unknown variables and need to be closed via model assumptions. The viscous parts of the diffusion term can be neglected and the viscous dissipation term is commonly approximated by the assumption of representing a locally isotropic dissipation process by $-\overline{\sigma_{ik}\partial u''_j/\partial x_k} - \overline{\sigma_{jk}\partial u''_i/\partial x_k} = 2/3\overline{\rho}\delta_{ij}\widetilde{\epsilon}$. The pressure induced diffusion parts (those containing p') are negligible compared to the triple correlation part $\widetilde{u''_i u''_j u''_k}$. The triple correlation part of the diffusion term is commonly modeled by assuming linear diffusion of Reynold stresses introduced by Launder [35]:

$$\frac{\partial}{\partial x_k}\left(\overline{\rho}\widetilde{u''_i u''_j u''_k}\right) = -C_s \frac{\partial}{\partial x_k}\left(\overline{\rho}\frac{\widetilde{k}}{\widetilde{\epsilon}}\widetilde{u''_k u''_l}\frac{\partial \widetilde{u''_i u''_j}}{\partial x_l}\right) \tag{3.24}$$

The last two remaining terms, especially the pressure strain-rate correlation term, are the object of multiple different closure models. The first model was proposed by Launder, Reece and Rodi [35; 36] for constant density flows, and is abbreviated as the LRR-RSM in literature. The pressure correlation term was split into two parts, the so-called rapid and slow parts, linearly dependent on $\overline{u''_i u''_j}$. Subsequent work by Speziale, Lumley and others (see e.g. [37; 38; 39]) have provided a mathematical theoretical basis for to this model to develop and achieve realizability constraints as well as proper treatment of strong stream-wise curvature [40]. These developments resulted in a quadratic model for the pressure correlation term proposed by Sakar, Speziale and Gatski [41], commonly called the SSG-RSM. This model is very well suited to modeling swirling flows as shown by Jones et al. [42] and Gibson et al. [43].

This model has several deficiencies, one being the complete neglect of variable density effects. This was corrected by Hogg and Leschziner [44] and Hirai and Takagi [45]. The other was the assumption of very high Reynolds numbers in the flow and hence local isotropy of fine scale turbulence. This is especially problematic in the near wall region, where anisotropies in the turbulent length scales extend into the large scale energetic eddies well above the Kolmogorov limit. This effect was corrected by the introduction of wall correction functions modifying the pressure strain-rate correlation term to reproduce experimental results. While this correction is sufficient for correctly reproducing simple wall bounded flows, it is insufficient for more complex wall-mean flow interactions of reattaching flows. Based on the groundbreaking work by Hallbäck and Johansson [46], by introducing an algebraic non-isotropic dissipation rate model for the ϵ-equation of RSMs, these anisotropies could be linked to physical flow processes and did not any longer require artificial correction functions. These algebraic extensions to the dissipation rate were used by Hanjalic and Jakirlic [47] to develop a low-Reynolds number RSM which was able to very accurately reproduce flow reattachment processes.

3.4 Transport of a passive scalar in swirling turbulent flows

Using the same approach as for to the momentum equations, the individual scalar fluxes $\overline{\rho}\widetilde{u_i''\varphi''}$ have to be closed via a turbulence model. Similarly to the Boussinesq-assumption for the Reynolds stresses, the standard approach to modeling these scalar fluxes is via a linear eddy diffusion assumption of

$$\overline{\rho}\widetilde{u_i''\varphi''} = \frac{\mu_t}{\mathrm{Pr}_t}\frac{\partial\overline{\varphi}}{\partial x_i} \tag{3.25}$$

where μ_t is the eddy viscosity as calculated by the turbulent momentum closure scheme (see eqn. 3.22) and Pr_t is the turbulent Prandtl number, commonly set equal to 0.7 or 0.6. Similarly to the Reynolds stresses, this assumption is simply erroneous for the case of flow with streamline curvature. Swirling flow may enhance or retard the transport of passive scalars, and in extreme cases it may even cause counter-gradient diffusion. Anisotropic production of scalar fluxes, and much the effects mentioned beforehand, can be captured with a linear eddy viscosity model. The reader is referred to Hirai and Takagi [48] for a detailed theoretical discussion of these effects. A practical example of where all three phenomena are observed is for example the TECFLAM burner [49; 50]. Just as with turbulent momentum transport, several non-linear eddy diffusivity models have been proposed and used in the past (see Groetzbach [51] or Jones et al. [27]), but all fail to even address most simplistic physical constraints such as the extremum principle, and hence failing realizability constraints which build upon these principles as prerequisites. The extremum principle simply says that given a strictly conserved scalar, all minimal and maximum values arising as a solution for such a scalar can only lie on the boundaries of the solution domain. Failure of meeting this criterion can have dire consequences as unphysical solutions can arise with for example negative mass fractions, mass fractions beyond unity and temperature profiles that can violate the second law of thermodynamics. The only non-linear model found in literature that rigorously adheres to these constraints is the one proposed by Jones and Lentini in 2008 [27].

An alternative method to modeling streamline curvature effects on scalar fluxes is to model the three individual scalar fluxes directed with their respective transport equations. The derivation of these equations is nearly identical to the derivation of the Reynolds stress transport equations, and the reader is referred to [52] for more details about this derivation. The resulting equation is shown below:

$$\begin{aligned}
&\underbrace{\overline{\rho}\frac{\partial \widetilde{u_i''\varphi''}}{\partial t}}_{\text{I = rate of change}} + \underbrace{\overline{\rho}\widetilde{u}_k\frac{\partial \widetilde{u_i''\varphi''}}{\partial x_k}}_{\text{II = convection}} = \underbrace{-\overline{\rho}\widetilde{u_k''\varphi''}\frac{\partial \widetilde{u}_i}{\partial x_k} - \overline{\rho}\widetilde{u_k''u_i''}\frac{\partial \widetilde{\varphi}}{\partial x_k}}_{\text{III = production}} \\
&\underbrace{-\frac{\partial}{\partial x_k}\left(\overline{\rho}\widetilde{u_i''u_k''\varphi''} + \widetilde{\varphi''p'\delta_{ik}}\right)}_{\text{IV}} + \underbrace{\overline{p'\frac{\partial \varphi''}{\partial x_i}}}_{\text{V}} - \underbrace{\overline{\varphi''}\frac{\partial \widetilde{p}}{\partial x_i}}_{\text{VI}} - \underbrace{\overline{\sigma_{ik}\frac{\partial \varphi''}{\partial x_k}}}_{\text{VII = dissipation}}
\end{aligned} \tag{3.26}$$

Similarly to RSMs, the rate of change, convection as well as production can be solved exactly, capturing most of the relevant physics for turbulent diffusion of scalars. The remaining terms (IV to VII) need to be closed via approximations. Of these terms, two terms are of great importance and scalar flux models found in literature will usually only differ by these terms. The relevant terms are the triple correlation term $\widetilde{u_i''u_k''\varphi''}$ in (IV) and the pressure-scalar-gradient correlation term (V). Term VII is zero if fine scale scalar fluctuations can be assumed to be isotropic, and the contribution of the pressure fluctuation part of term IV is deemed negligible compared to the triple correlation part. The last remaining term VI is either neglected or modeled via the following assumption for the density-covariance term:

$$\overline{\varphi''} = \frac{\overline{\varphi''^2}}{\overline{\rho}} \frac{\partial \overline{\rho}}{\partial \widetilde{\varphi}} \tag{3.27}$$

with an additional transport equation for $\overline{\varphi''^2}$ being solved.

The first scalar flux model was proposed by Launder and Samaraweera [53] for flows with constant density and used linear correlations for terms IV and V. Similarly to RSMs, the pressure-scalar-gradient correlation term V is divided into a slow and rapid part. Jones and Musonge [54] extended their model to satisfy realizability constraints. These models were found to be lacking due to the assumption of constant density, which was corrected by the introduction of Favre-averaging by Hogg and Leschziner [44] and Hirai and Takagi [45] who also applied this model to simulate the very challenging series of experiments by So et al. [55] on a model swirl combustor. The linear correlations for terms IV and V of the previous models were extended to quadratic correlations by Ohtsuka [56] and Kawamura et al. [57]. The model by Ohtsuka showed the best agreement of all scalar flux models models with experiments (including those by So et al. [55]) but the complex closure terms introduced ignored the division of a rapid and slow part for the pressure correlation term. In terms of physical soundness, this is very suspect since Brasseur [58] showed in a series of direct numerical simulations that the separation of a rapid and slow part in the pressure correlation term is necessary. The rapid and slow part both represent two phenomena with physical time scales that are independent of each other. Kawamura et al. [57] on the other hand, developed the most complex non-linear scalar flux model to date which satisfies realizability, but in doing so, Pope's linearity principle [59] had to be abandoned. To date, the author could not find any application of these models outside of 2D applications, and most models are only derived for 2D axial-symmetric flows.

3.5 Form and implementation of present turbulence model

For modeling the turbulent transport of momentum, the SSG Reynolds stress model [41] was selected. It is a well validated model that has been used to model swirling flows in the past (see the reviews [25; 26]) with very good results. It offers a good compromise between quality of results and modeling effort compared to more elaborate models such as the model proposed by Hanjalic and Jakirlic [47] or Hallbäck [46]. Additionally, by choosing a Reynolds stress model, second order closure schemes can be extended to the turbulent transport of scalars offering the ability of significantly more accurate modeling of turbulent scalars in swirling flow. As shown in the previous chapter, non-linear eddy diffusivity schemes violated in many cases even basic principles such as the extremum-principle and even the most modern model, which satisfies realizabilty and other basic principles, by Jones [27], produces poorer results compared to the second order modeling of scalars. Hence, the choice to implement a RSM was mostly dictated by the lack of good alternatives to a full second order closure for the turbulent flux of scalars. Only for the case of swirling flows with no scalar transport, modern quadratic or cubic $k - \epsilon$ models offer similar agreement with experiments as RSMs, with the advantage of significantly improved numerical stability and convergence.

More elaborate RSMs than the SSG-model were deemed unnecessary due to several reasons. Firstly, the near wall behavior of flow is not of high importance in the lower plenum of HTRs. Nearly all mixing of hot and cold gases occurs in the main flow, far away from any wall influences. Neither are considerations such as the exact points of reattachment of separated flow phenomena highly important, as they depend on very accurate modeling of the anisotropic dissipation of momentum in vicinity of the wall. Secondly, buoyancy effects can be neglected in the lower plenum. The flow regime can be placed into the regime of strongly forced convection as well as turbulent perturbations arising from buoyancy effects can be neglected due to the (densimetric) Froude number being greater than approximately 1000:

$$\mathrm{Fr} = \frac{U^2}{gD\left|1 - \rho_{hot}/\rho_{cold}\right|} \tag{3.28}$$

where U is the characteristic mean velocity of the flow, g the gravitational acceleration constant, D the molecular diffusion constant, ρ_{hot} and ρ_{cold} is density of the hot and cold helium, respectively, entering the lower plenum. For the Damm and Wehrlein air validation test case, $U = 60\frac{m}{s}$, $D \approx 10^-5 m^2 s^{-1}$, $\rho_{hot}/\rho_{cold} \approx 0.8$; and for the BenSaid reactor test case, $U = 90\frac{m}{s}$, $D \approx 10^-5 m^2 s^{-1}$, $\rho_{hot}/\rho_{cold} \approx 0.8$. Hence, for both cases the densimetric Froude number is well above 1000. Based on the above Froude number definition (eqn. 3.28), Chen and Rodi [60] have introduced a scaled distance $\widehat{x} = \mathrm{Fr}^{-1.2} \left(\rho_{hot}/\rho_{cold}\right)^{1.4} x/D$ and shown in experiments with round jets that buoyancy instabilities become important for $\widehat{x} > 0.5$. For the case of the lower plenum flow in an HTR, $\widehat{x} \ll 0.5$ (it is of order 10^{-4}), and hence all buoyancy terms in turbulence models can be neglected.

The SSG model used in this thesis does not formally contain Favre-averaged quantities, but instead, a form of variable-density Reynolds-averaged flow has been implemented. Instead of using the formally correct Favre-averaged transport equations for the Reynolds stress transport equations, the simpler constant density Reynolds-averaging has been used instead, where the density has been allowed to be variable (alternatively, one can think that all new terms arising due to Favre-averaging have been neglected). While the above formulation is not correct in a strict mathematical sense, it has been shown by Chen et al. [61] on the basis of multiple DNS that the effect of this error is minuscule for the case of momentum transport. On the other hand, Chen et al. demonstrated that the difference of using a Favre-averaged versus "variable-density" Reynolds-averaged quantities for scalars to be very significant. The exact form of the implemented SSG model is shown below:

$$\rho\frac{\partial\overline{u_i'u_j'}}{\partial t} + \rho\overline{u}_k\frac{\partial\overline{u_i'u_j'}}{\partial x_k} = \Psi_{ij1} + \Psi_{ij2} + P_{ij} + \frac{\partial}{\partial x_k}\left[\left(\mu + \frac{2}{3}c_s\rho\frac{k^2}{\epsilon}\right)\frac{\partial\overline{u_i'u_j'}}{\partial x_k}\right] - \frac{2}{3}\delta_{ij}\rho\epsilon \tag{3.29}$$

where Ψ_{ij1} and Ψ_{ij2} are the pressure strain correlations, divided into their slow and rapid parts respectively. These terms are modeled as follows:

$$\begin{aligned}\Psi_{ij1} &= -\rho\epsilon\left[c_{s1}a_{ij} + c_{s2}\left(a_{ij}a_{ij} - \frac{1}{3}\delta_{ij}a_{kl}a_{kl}\right)\right]\\ \Psi_{ij2} &= -c_{r1}Pa_{ij} + c_{r2}\rho kS_{ij} - c_{r3}\rho kS_{ij}\sqrt{a_{ij}a_{ij}} \qquad (3.30)\\ &\quad + c_{r4}\rho k\left(a_{ij}S_{ji} + S_{ij}a_{ji} - 2/3\delta_{ij}a_{ij}S_{ij}\right) + c_{r5}\rho k\left(a_{ij}W_{ji} + W_{ij}a_{ji}\right)\end{aligned} \tag{3.31}$$

and,

$$\begin{aligned} a_{ij} &= \frac{\overline{u_i'u_j'}}{k} - \frac{2}{3}\delta_{ij} \\ S_{ij} &= \frac{1}{2}\left(\frac{\partial \overline{u_i}}{\partial x_j} + \frac{\partial \overline{u_j}}{\partial x_i}\right) \\ W_{ij} &= \frac{1}{2}\left(\frac{\partial \overline{u_i}}{\partial x_j} - \frac{\partial \overline{u_j}}{\partial x_i}\right) \end{aligned} \tag{3.32}$$

P_{ij} is the exact Reynolds stress production term:

$$P_{ij} = -\rho\left(\overline{u_i'u_k'}\frac{\partial \overline{u_k}}{\partial x_j} + \frac{\partial \overline{u_k}}{\partial x_j}\overline{u_k'u_i'}\right) \tag{3.33}$$

The following ϵ-transport equation is used in this thesis:

$$\frac{\partial \rho\epsilon}{\partial t} + \frac{\partial \rho \overline{u_k}\epsilon}{\partial x_k} = \frac{\epsilon}{k}\left(c_{\epsilon 1}P - c_{\epsilon 2}\rho\epsilon\right) + \frac{\partial}{\partial x_k}\left[\left(\mu\delta_{kl} + c_\epsilon \rho\frac{k}{\epsilon}\overline{u_k'u_l'}\right)\frac{\partial \epsilon}{\partial x_l}\right] \tag{3.34}$$

For modeling the scalar fluxes $\overline{\rho}\widetilde{u_i''\varphi''}$ a model based on the one proposed by Launder and Samaraweera [53] was used, modified to reflect Favre-averaging and variable density. The modifications are similar to those introduced by Hogg and Leschziner [62] or Hirai and Takagi [45], only applied to 3D-Cartesian coordinates instead of a 2D-axial symmetric coordinate system. It was at first planned to use more complex models, but the results of the simple model by Launder and Samaraweera produced sufficiently satisfactory results, while the numerical stability was tenuous at best. More complex models have been reported to converge more poorly [27]. These more elaborate models would only offer improvements in the turbulent fluctuating scalar flux terms $\overline{\rho}\widetilde{u_i''\varphi''}$ but little effect in mean flow values such as density or scalar concentrations (compare the results of for example Jester-Zürker et al. [25], Hogg and Leschziner [62], Ohtsuka et al [56] and Hirai and Takagi [45] between different scalar flux models for the same set of experiments). The exact form of the implemented scalar flux transport equations is:

$$\widetilde{u}_j\frac{\partial}{\partial x_j}\left(\overline{\rho}\widetilde{u_i''\varphi''}\right) = -\overline{\rho}\widetilde{u_i''u_j''}\frac{\partial \widetilde{\varphi}}{\partial x_j} - \overline{\rho}\widetilde{u_j''\Phi''}\frac{\partial \widetilde{u}_i}{\partial x_j} + \Pi_{i\Phi} + Diff \tag{3.35}$$

where $\Pi_{i\Phi}$ is the pressure-scalar gradient correlation, which is closed via the following closure approximations:

$$\Pi_{i\Phi} \;=\; -C_{1\Phi}\bar{\rho}\frac{\epsilon}{k}\widetilde{u_i''\Phi''} \;+\; C_{2\Phi}\bar{\rho}\widetilde{u_j''\Phi''}\frac{\partial\widetilde{u}_i}{\partial x_j} \tag{3.36}$$

and $Diff$ is the diffusion transport term, which is closed by the following gradient approximation:

$$Diff \;=\; -\frac{\partial}{\partial x_j}\left[C_{s\Phi}\bar{\rho}\frac{k}{\epsilon}\left(\widetilde{u_l''u_j''}\frac{\partial\widetilde{u_i''\Phi''}}{\partial x_l} \;+\; \widetilde{u_l''u_i''}\frac{\partial\widetilde{u_j''\Phi''}}{\partial x_l}\right)\right] \tag{3.37}$$

The constants are defined in table 2 below.

$C_{1\Phi}$	$C_{2\Phi}$	$C_{s\Phi}$
3.0	0.33	0.11

Table 2: Values of constants used for scalar flux model.

The turbulence model as described above will be validated via two experimental series published and widely used in turbulence modeling literature. The first set of experiments were performed by Steenbergen [63] on the transition of unstable swirl in smooth round pipes to solid body rotation. This experiment will be used for validating the turbulent transport of momentum. In a second step, the validation of turbulent diffusion of passive scalars will be based on an experimental series performed by So et al. [55; 64; 65; 66] on a model combustor with strong swirl. More details about these experiments can be found in subsequent chapters.

Chapter 4

Numerical Setup

4.1 Method of Solution

At the very beginning of the present project, a choice was made to use a commercial program for CFD-simulations rather than to develop a new code. It was clear that the emphasis of the work would lie in obtaining physically relevant data, their analysis and their practical use in future design of the lower plenum. It was decided to use the program system ANSYS CFX-11 for following reasons: the structure of the code made relatively easy implementation of a new turbulence model possible, there was an extensive experience with this program, the program had a proven capability of simulating the investigated flow field and, last not least, the cost of the program was acceptable. A detailed discussion of the advantages and disadvantages of the program CFX will be offered at the end of this chapter.

The original CFX-solver was conceived for incompressible flow, with modifications allowing variable density. The governing equations are solved in their nonconservative form, using the so-called primitive variables u,v,w,p and static enthalpy h. In the full form that also includes the density as a field variable, the governing equations have a mixed hyperbolic-parabolic character. As a consequence, the flow changes are distributed throughout the flow field as waves, with information propagating along characteristic directions with the corresponding wave speeds. A genuine compressible solver of the Navier-Stokes equations has to take this into consideration. In the CFX-code, attention was payed to achieving significant geometric flexibility.

The discretization of the flow field is accomplished using unstructured multihedral finite volume cells. The grid consists actually of nodal points - nodes - at which location all the information about the flow field is stored. Neighboring nodes form an element, which could be a tetrahedral, hexahedral or, generally, multifaceted polyhedral. The centroids of these elements (with a node being at its centre) form a finite volume cell, for which the balance of fluxes of mass, momentum and energy is formed (see figure 4.1). For the determination of the fluxes, it is necessary to extrapolate/interpolate the information necessary for their computation. There are many possible procedures for this step, ranging from very simple constant value assumption (1st-order accurate) to multidimensional extrapolations n-th order. In CFX, the so-called linear shape functions were implemented, which means that linear interpolations second order accurate in space are used. Only the functional vector of the first 4 primitive variables (u,v,w,p) is being interpolated in a direction aligned approximately with the streamlines. Enthalpy and other auxiliary variables, such as turbulence modeling variables, are discretized via the constant value assumption within each finite volume cell, which is only 1st-order accurate. No consideration was given to numerical wave propagation speed and direction.

The discretization in time is implemented by using 1st- or 2nd-order accurate backward differencing in time. Alternatively, a steady formulation can be chosen, with the time derivatives serving as additional terms for relaxation in pseudo-time.

In the simple 2nd-order accurate extrapolation form, the CFX-procedures would display severe oscillation (wiggles) that would eventually destroy the solution. This was obviously known to ANSYS, which is why the reconstruction procedure was augmented by the addition of quasi-nonlinear 4th order artificial damping. In an implicit form, a fourth-order derivative of the pressure is incorporated into the extrapolation. Although being linear and certainly scalar, not reflecting any physics of the flow field, the pressure damping has the advantage that it approaches zero in boundary layers in the direction normal to the surface, thus minimizing its influence on the effective Reynolds number (a Reynolds number taking into consideration the molecular as well as numerical viscosity). However, the amount of artificial damping being added still has to be limited

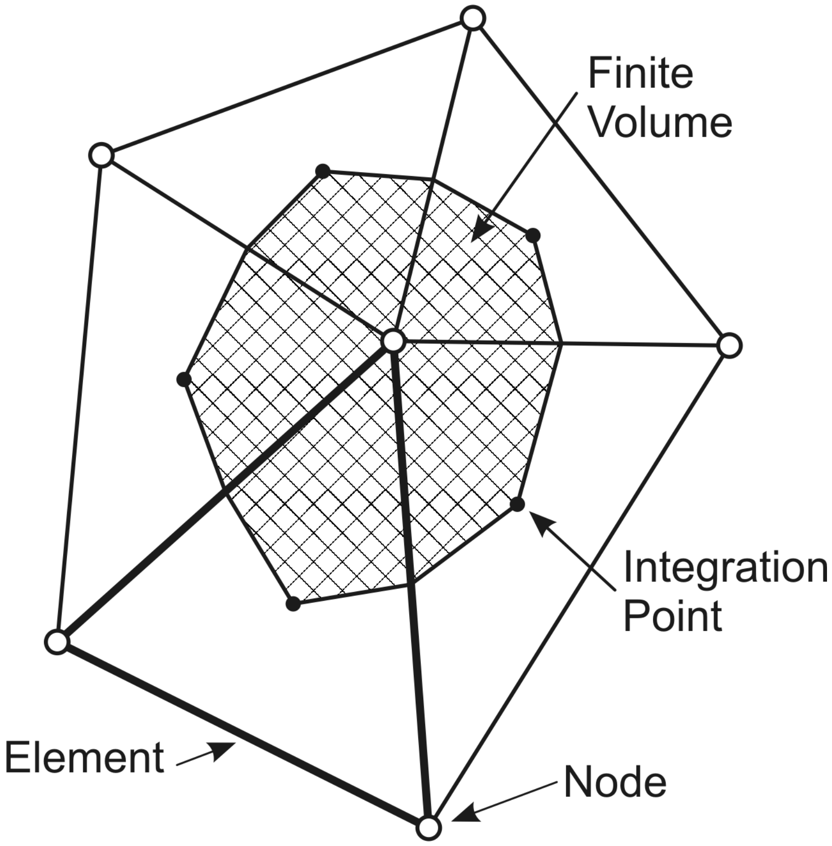

Figure 4.1: Explanation of discretization nomenclature used in CFX.

in order to keep the effective Reynolds number as large as possible. The linear extrapolation is therefore augmented by limiters that are constructed such that in the places with local minima or maxima the accuracy of the extrapolation is reduced. This is similar to the TVD (total variation diminishing) procedures known from compressible flow solvers [67].

The resulting system of equations, given by the continuity and momentum equations (the energy equation as well as all other scalar equations and the auxiliary equations for turbulence modeling were decoupled) at each integration point, consists of blocks of four equations for the unknown state variables (u,v,w,p). Due to the discretization described above, the system is linearized and sparse. It is solved directly by ILU-decomposition (incomplete lower-upper decomposition). As the system is very large (for n internal nodes it results in 4n equations), the solution procedure has to be accelerated. This is accomplished by introducing a simple algebraic multi-grid, where the solution is obtained subsequently on refined hierarchical grids.

The resulting scheme is relatively robust, sufficiently quick (mostly) with satisfactory results for low speed flows. It has, of course, also several disadvantages. It is only second order accurate in space, non-conservative, weakly coupled and it displays a linear scalar artificial damping with all the corresponding artifacts. It is consequently only suitable for simulating incompressible and weakly compressible flows (i.e. variable density flows with $Ma < 0.3$) where the Rankine-Hugoniot relationship plays no role.

The scalar flux turbulence model, as described in chapter 3.4, was implemented via three user defined additional transport variables, one for each individual scalar flux. The default linear eddy diffusion turbulence model of the energy equation, mixture fraction, as well as that for the individual scalar fluxes, was switched off by setting the turbulent Prandtl number very high (O 10^6). The default transport equations of CFX, used for the scalar flux variables, were extended via source terms and ANSYS CFX expression language (CEL). All necessary differential terms were implemented via user Fortran routines and referenced via user defined functions. The actual turbulence terms of $\frac{\partial}{\partial xi}\bar{\rho}\widetilde{u_i'\phi'}$ in the energy equation and mixture fraction equation were added as source terms to the relevant transport equation. The resulting system of expressions, additional transport variables and source terms function as the new turbulence model for a passive scalar.

4.2 Boundary Conditions

4.2.1 Steenbergen experiments

Steenbergen investigated [63] the decay of unstable swirl to solid body rotation flow over long distances in round pipes. The case chosen for validation has most swirl momentum concentrated close to the center line (see figure 4.2) with a swirl number of 0.1. The swirl number S is defined as follows:

$$S \equiv \frac{\int_0^{R_o} uwr^2 dr}{R_o \int_0^{R_o} u^2 r dr} \tag{4.1}$$

where r is the radial distance from the center line, R_o is a half of the pipe diameter, u is the axial velocity and w is the circumferential velocity. Over a short axial distance x of approximately 15 pipe diameters circumferential velocity close to the center line is attenuated by about 20%. At approximately 15 pipe diameter axial length ($x/D_j = 15$), a sudden vortex breakdown occurs and at approximately 20 pipe diameters in axial length most swirl momentum is shifted toward the walls and a condition very close to solid body rotation is achieved. It is this process of sudden vortex breakdown and shifting swirl momentum from the center line to the pipe walls where the selection of an adequate turbulence model is of great importance.

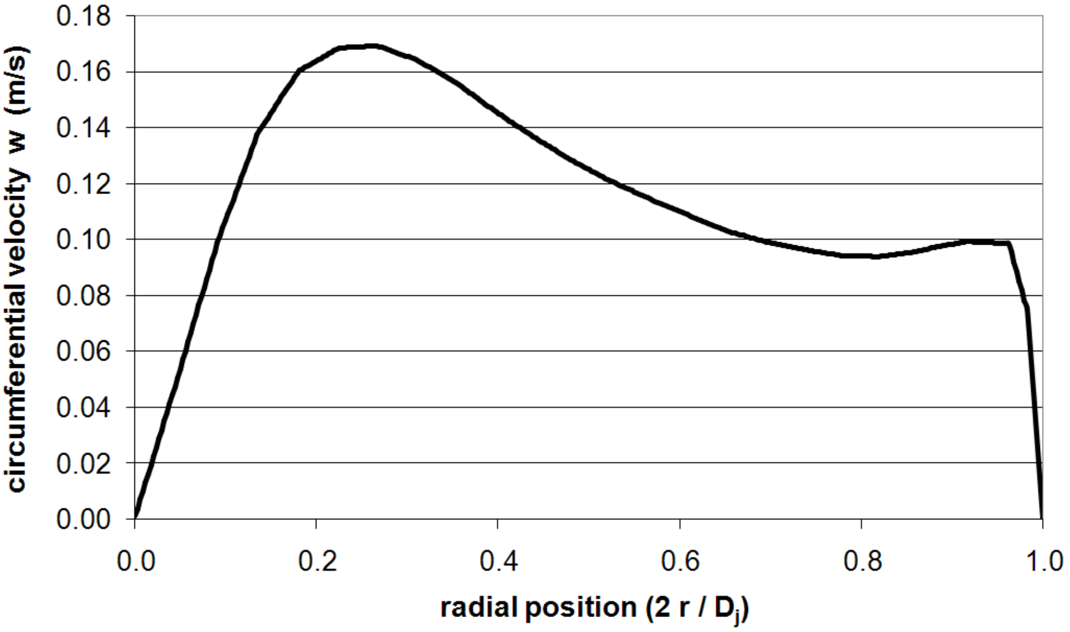

Figure 4.2: Inlet circumferential velocity against radial position of the Steenbergen experiments used as inlet boundary conditions for the Steenbergen validation calculations.

The experiment has measurement points at $x/D_j = 0, 3.7, 7.2, 17$, and the measured experimental values of axial velocity u, circumferential velocity w and all Reynolds stresses $\rho\overline{u_i' u_j'}$ at $x/D_j = 0$ were used to initialize the CFD calculations. The CFD domain extends to $x/D_j = 80$ where a constant mass flow boundary condition was set. The mesh used was a quasi-2D wedge of 5 degree angular thickness with 80 cells in radial direction and 800 cells in axial direction.

Fundamental to modeling the vortex breakdown as well as swirl decay was the proper initialization of the turbulent length scale ϵ. ϵ was initialized for this flow by assuming that turbulence energy is in equilibrium with a characteristic length scale l_m [62]:

$$\epsilon = k^{1.5}/c_\mu^{-0.75} l_m \tag{4.2}$$

where $c_\mu = 0.03$ and $l_m = 0.1r$. Without this initialization of ϵ the results of all turbulence models were very poor. Interestingly, the k - ϵ model would be improved by using incorrect assumptions such as the commonly used uniform turbulence intensity of 5%.

4.2.2 So et. al experiments

The experiments by So et al. [55; 64; 65; 66] consist of a smooth pipe with a strongly swirling outer flow annulus and at the centerline a non-swirling Helium enriched jet is injected into the pipe (a sketch of the experiment can be seen in fig. 4.3). The Helium enriched jet mixes with the pure air swirl flow and He concentrations as well as relevant velocities are measured. The experiments supply a rich data set for mean flow velocities, scalar concentrations and turbulence quantities for velocity as well as scalar concentration.

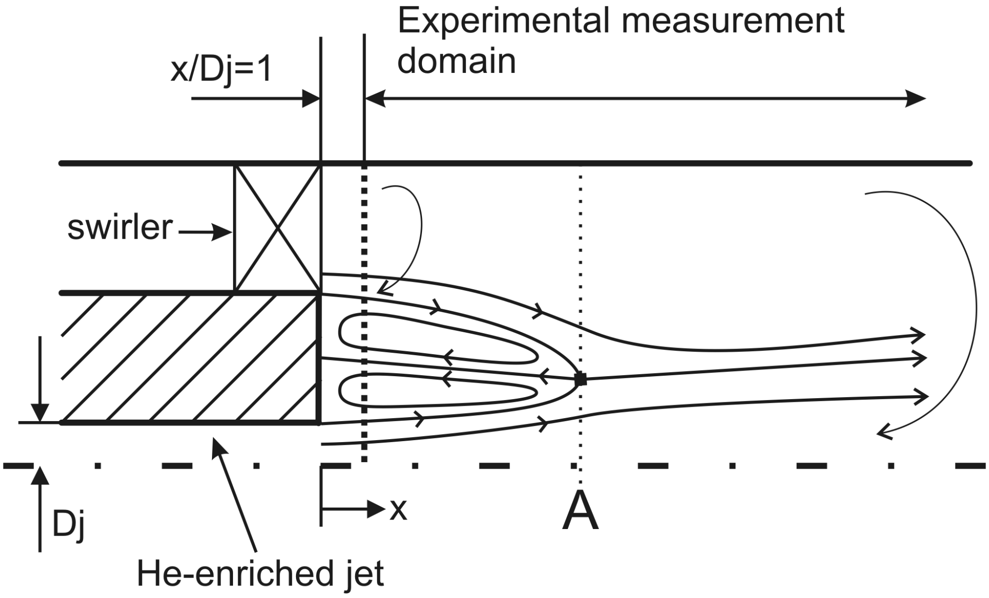

Figure 4.3: Sketch of the experiment by So et al., showing the reattachment point at A

One particularly important issue with RSMs is setting the correct boundary condition for the individual Reynolds stresses as well as an estimation of the turbulent dissipation length scale ϵ. The dissipation length ϵ was calculated under the same assumption of turbulence energy equilibrium and a characteristic mixing length scale l_m as done before for the Steenbergen validation calculations (see equation 4.2):

$$\epsilon = k^{1.5} / c_{\mu}^{-0.75} l_m \tag{4.3}$$

where $c_{\mu} = 0.09$ and $l_m = 0.06r$, which was used previously successfully for the same experiments by Hogg and Leschziner [62]. In oder to estimate the sensitivity of the simulation with respect to the assumed mixing length l_m, it was varied between $0.03r$ and $0.3r$, but no significant effect was observed for velocity scales as well as Helium concentrations.

The experiments by So et al. provide information about the Reynolds stresses of the $\overline{u'^2}$ and $\overline{w'^2}$ components only, the remaining 4 Reynolds Stresses as well as all scalar fluxes are unknown. Hence it was deemed essential to reconstruct the flow history of these experiments by modeling a 24 ° radial symmetric wedge of the entire inlet pipe and swirl generator (figure 4.4). Henceforth, this will be called the “inlet domain”. The 24 ° wedge represents the angular distance between two blades of the swirl generator. The inlet domain starts directly behind the honeycomb flow straightener of the experimental rig, continues to the swirl generator where the flow over a single vane is modeled, and ends at the axial distance x of $x/D_j = 10$ from the helium inlet nozzle within the experimental measurement domain (figure 4.5). The radial symmetric inlet wedge has an inner diameter $D_i = 53.2mm$ and an outer diameter of $D_o = 126.6mm$.

The reconstructed turbulence data are used for the inlet boundary condition of the CFD simulation within the experimental measurements domain (figure 4.5). This domain starts at $x/D_j = 1$ and extends to $x/D_j = 40$ where a 5 ° radial symmetric quasi-2D domain is used. The velocity flow fields and mass fraction fields are initialized with the first set of experimental data at $x/D_j = 1$. For reference, all x/D_j data are in respect to the original experimental coordinate system, for more information about the geometry of the experiments the reader is deferred to the experiments by So et al. The following naming convention is used for the principal directions: x, y, z for axial, radial and circumferential directions

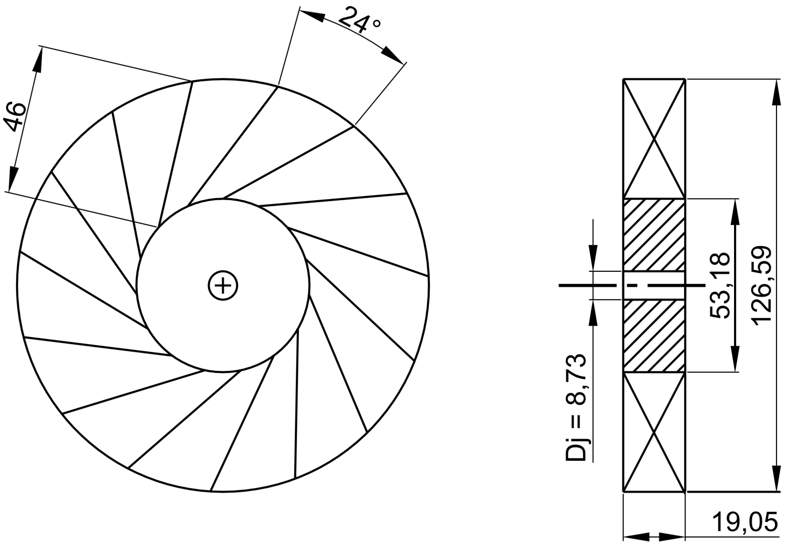

Figure 4.4: Schematic of the swirl generator for the So et al. validation case

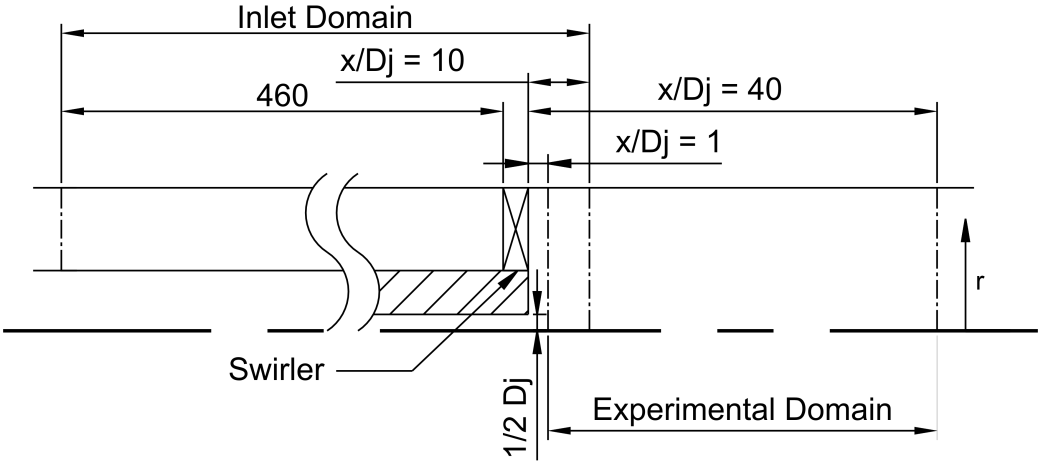

Figure 4.5: Sketch showing the different CFD modeling regions for the So et al. validation case

respectively; u, v, w for axial, radial and circumferential velocity components.

Of the several different cases documented by So et. al., only the following case is presented in this thesis: The central jet velocity U_j is equal to $36.5m/s$, the central jet has a mass mixture fraction of Helium of 0.9 and the swirling flow has a swirl number of $S = 2.25$. A sufficiently resolved mesh for the inlet domain was found at approximately 700 000 hexahedral cells. Due to the quasi-2D mesh of the experimental domain, it consists of 20 000 hexahedral cells only. The swirl generator inlet simulation produced a flow field with a significantly anisotropic Reynolds stress tensor, which explains why previous simulation attempts at modeling these experiments failed when more simplistic isotropic turbulence inlet assumptions were used, but more details can be seen the following chapter 5.1.2.

4.2.3 HTR lower plenum geometry

The main issue of defining the boundary condition for the lower plenum flow as investigated in the Damm and Wehrlein experiments is the correct reproduction of the exact inlet conditions which are very poorly documented. In the experiments, a blower is pushing air into the upper plexiglas chamber consisting of 2 annular zones (see figure 1.3): an outer cold zone and an inner hot zone. The flow is from the top to bottom and at the bottom of these annular zones there is a pressure-drop plate with a series of long, small and straight channels (called “core simulation” by Damm and Wehrlein) feeding into 4 concentrically arranged channels called “hot gas plenum” which feed the four individual rows of “hot gas channels” inlets into the lower plenum (see figure 2.2). No dimensions for this complex channel system are available and the modeler is hence tasked to reproduce the effects of this channel system. The main aim of this channel system is to prevent any feedback of the flow from the lower plenum into the “core simulation” chamber, as well as separating the lower plenum flow as much as possible from any effects introduced by the blowers and heating system.

For a CFD simulation, this effect can be achieved by placing four large concentric chambers above the inlets of the lower plenum chamber (see figure 4.6. One concentric chamber per inlet row. By giving these chambers a sufficiently large height to width ratio which is above 5, the flow is given a sufficiently small flow resistance to organize itself in azimuthal direction. This way, the constant pressure inlet boundary condition placed at the top of concentric inlet chambers will not introduce any bias onto the mass flow imbalances between the 18 round inlets into the lower plenum chamber. Any inlet boundary condition with prescribed mass flow or prescribed velocity would prevent the self-organizational aspect of the flow taking the path of least resistance through the experimental rig. The dimensions of these inlet chambers can be seen in figure 4.6 for the air test cases. For all other relevant dimensions of the lower plenum the reader is referred to chapter 2 and figure 2.1.

The CFD simulation on the lower plenum will be divided to two groups. The first group of simulations is based on the Damm and Wehrlein air experiments (abbreviated henceforth simply as D&W) and are used for validation purposes. The second group of simulations will be based on real HTRs with high temperature helium flow, called the “BenSaid reactor test cases”. Between the two groups of simulations, the shape of the lower plenum is identical with the only difference being that all dimensions of the “BenSaid reactor test cases” need to be multiplied by a factor of 2.9. The reactor test cases are based on reactor exit temperatures published by Ben Said [7] and represent the currently most accurate estimates published in literature on the coupled thermo-hydraulic and neutronic behavior of HTRs.

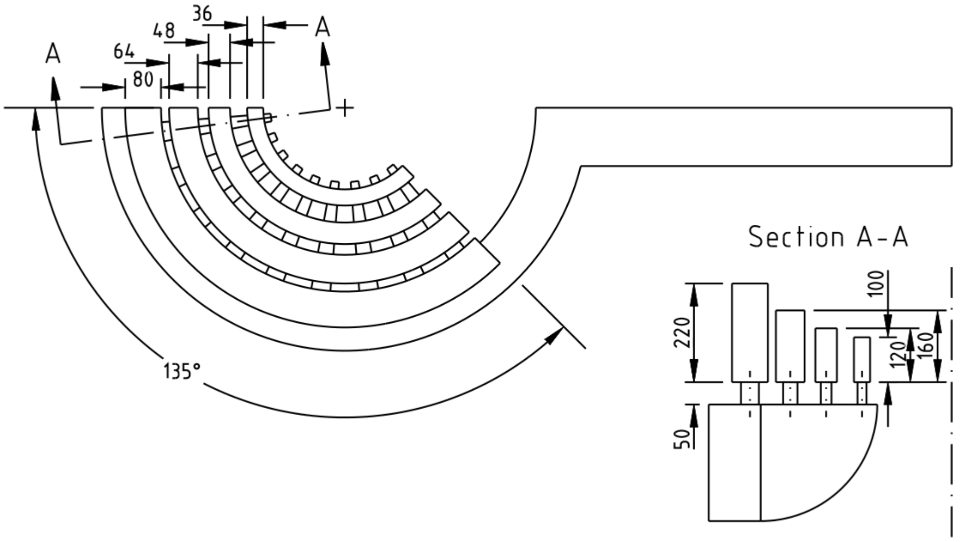

Figure 4.6: Design drawing of the inlet chambers above the lower plenum used for air test cases

The inner two concentric inlet chambers were given the “hot” temperature of 60 °C, mirroring the Damm and Wehrlein experiments exactly, or 760 °C for the case of a realistic reactor with helium as coolant (see figure 4.7 and Table 3). The two outer inlet chambers were given the “cold” temperature of 20 °C or 640 °C for the air experiments and reactor flow respectively. Turbulence quantities for momentum were initialized with zero gradient, ie. fully developed flow, at the inlets.

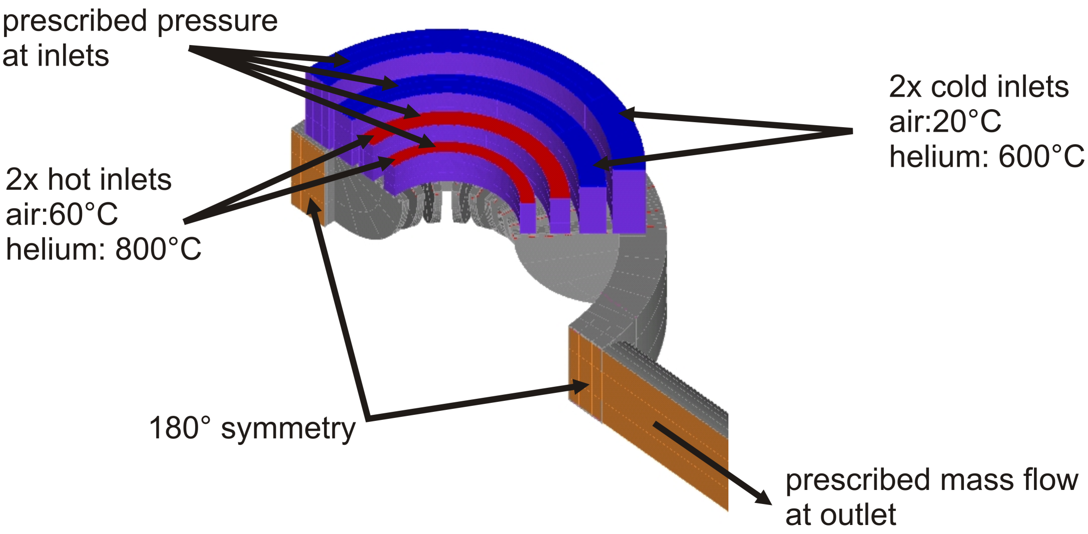

Figure 4.7: Prescribed boundary conditions on a 180 ° symmetric part of the lower plenum

Since the option of a zero gradient inlet condition for additional user-defined variables is not available in CFX, the turbulent scalar quantities were initialized via a separate calculation using an additional inflow geometry. The idea behind this calculation is to elongate the inlet chambers to sufficient flow-length over width ratios that a fully developed flow is achieved in each of the four inlet chambers. The turbulence data hence calculated at the outlets of this geometry can be used as the inlet boundary condition of the inlet chambers for the lower plenum calculations. This geometry is identical to the inlet chambers with the only difference in their height being equal to 200 times the width of the individual concentric chambers. The boundary conditions for this geometry were as follows: Constant pressure at the inlet and prescribed velocity at the outlet, taken from the results of k-ϵ calculations for the inlet chambers of the lower plenum. The scalar fluxes were set to zero at the inlet of the inflow geometry and the values calculated at the outlets were used to initialize the inlet of the lower plenum when using the scalar flux model.

The outlet condition is a constant mass flow outlet with its mass flow defined according to a Reynolds number

$$Re = \frac{\rho \overline{\overline{U}} D}{\mu} \tag{4.4}$$

with the characteristic length scale D being the diameter of the outlet pipe, the characteristic velocity $\overline{\overline{U}}$ being the average axial outlet pipe velocity. The density ρ as well as dynamic viscosity μ properties of the fluid are taken at the average outlet temperature $T_{cold} + T_{hot}/2$. The relevant dimensionless numbers as well as fluid properties for the different test cases can be seen in Table 3 below.

case	Fluid	T_{hot}	T_{cold}	p (bar)	Re	Ma	Pr
D&W 1	air	60 °C	20 °C	1.3	1.6×10^6	0.27	0.66
D&W 2	air	60 °C	20 °C	1.3	1.3×10^6	0.22	0.66
D&W 3	air	60 °C	20 °C	1.3	1.0×10^6	0.17	0.66
D&W 4	air	60 °C	20 °C	1.3	0.6×10^6	0.10	0.66
BenSaid 1	helium	800 °C	600 °C	60	3.2×10^6	0.03	0.64
BenSaid 2	helium	800 °C	600 °C	60	1.6×10^6	0.02	0.64
BenSaid 3	helium	800 °C	600 °C	60	1.3×10^6	0.02	0.64
BenSaid 4	helium	800 °C	600 °C	60	1.0×10^6	0.01	0.64
BenSaid 5	helium	800 °C	600 °C	60	0.6×10^6	0.01	0.64

Table 3: Dimensionless parameters for all investigated test cases.

For the D&W test cases, air according to the ideal gas law was chosen as fluid. Due to the small temperature differences of 40 °C as well as very small pressure difference within the domain, the assumption of the fluid behaving under the ideal gas law is adequate. For the BenSaid reactor test cases, the gas phase combustion material database implemented in CFX was used for determining the fluid properties of helium. In comparison to the high-precision helium properties [68] of the Forschungszentrum Jülich, which are for example used for designing current high-temperature reactors, deviations of the CFX database are well below 0.1% for density, enthalpy and viscosity for the flows investigated in this thesis. This agreement is more than sufficient for accurate calculations and hence there is no need to implement the helium datatables of the Forschungszentrum Jülich.

4.3 Meshing of the HTR lower plenum geometry

Due to the relatively big size of the simulation domain and its complex form, coupled with small scale flow phenomena throughout most of the geometry, meshing this domain is challenging. In order to minimize numerical errors with the least amount of elements, most of the domain has been meshed using a hexahedral block mesh. Due to the complexity of the geometry, two small tetrahedral interface meshes had to be introduced to link different block meshes. The first of these interfaces can be found at the location where the square collection duct of the lower plenum chambers feeds into the round outlet pipe (figure 4.8). Due to the large space available at the top and bottom of this interface mesh, the mesh features a hexahedral core which reduces the amount of necessary elements for this interface by a factor of four. The second of these tetrahedral interface meshes is situated directly beneath the four round inlet holes of the lower plenum (figure 4.9). There are nine of these interface meshes, one for each “rib” cavity, each being 10mm thin (air test scale). The inlet chambers above the lower plenum have been meshed with a very coarse tetrahedral mesh which is refined toward the lower plenum inlets. Since the only purpose of these inlet chambers is to allow for the flow to find the path of least resistance into the lower plenum, this mesh is rather unimportant and can be hence made very coarse. The 180 ° symmetry of the geometry was made use of, and hence only half of the geometry is meshed. When simulating the full 360 ° geometry, then a second mesh half is mirrored and merged with the existing half.

Mesh sensitivity studies were performed using the k-ϵ turbulence model for fast convergence. The test case used for this assessment was the $Re = 1.6 \times 10^6$ air test case. Two criteria were chosen to asses the quality of solution of the mesh, the dimensionless pressure loss coefficient ξ and the dimensionless mixing efficiency Ψ:

$$\xi = \frac{\Delta P}{\rho U^2} \tag{4.5}$$

Where ΔP is the absolute pressure loss across the entire domain, and U is the average velocity at the outlet pipe.

$$\Psi = 1 - \frac{\Delta T_{local}}{\Delta T_{inlet}} \tag{4.6}$$

Ψ is a measure of mixing between two locations. A value of one means that all temperature variations found at the inlet have been mixed completely, down to a homogeneous temperature. A value of zero means that fluid exits the downstream location as unmixed as it entered the domain.

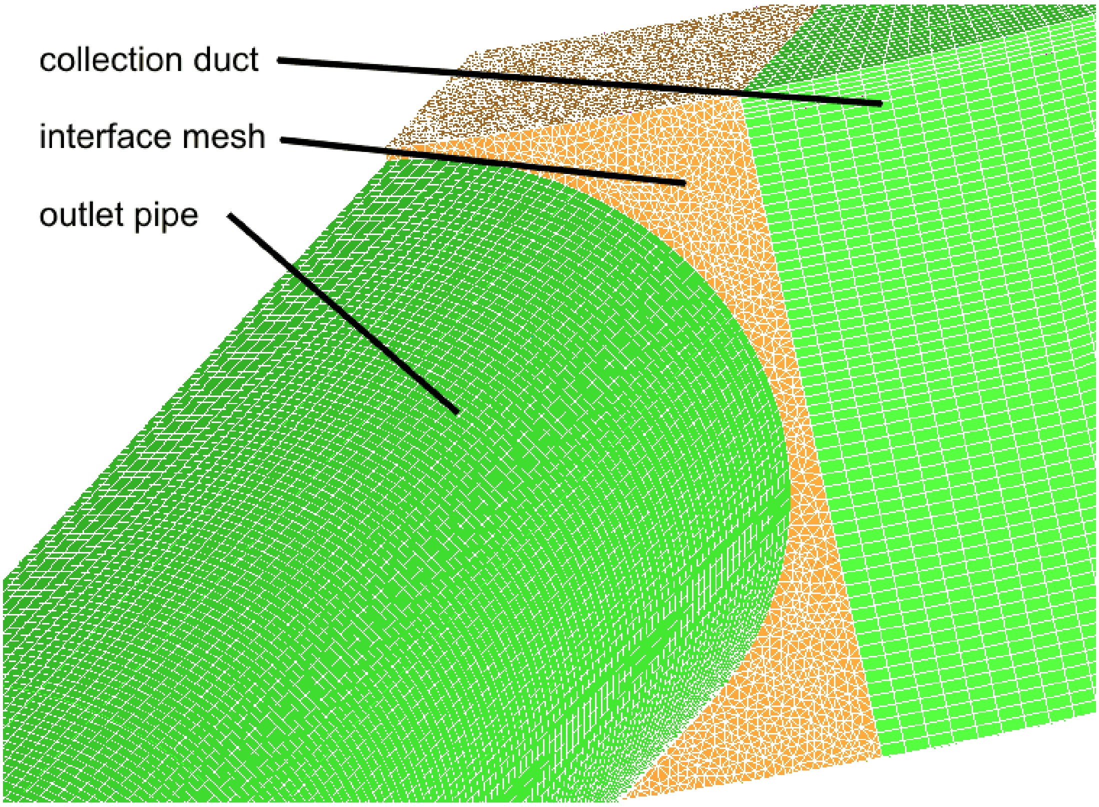

Figure 4.8: Tetrahedral interface mesh situated between the square collection duct of the lower plenum and the round outlet pipe

The mesh sensitivity of ξ can be seen in figure 4.10. A mesh beyond approximately one million elements is insensitive to mesh refinement. Ψ was calculated for two locations, the first comparing the temperature variations between inlet and outlet of the entire domain; the second being the comparison between inlet and the start of the outlet pipe. The results for this variable can be seen in figures 4.11 and 4.12. The results comparing inlet with outlet show an insensitivity of with respect to mesh refinement. For the case of inlet against the start of the outlet pipe, only the last two data points show that the mesh is starting to become insensitive to mesh refinement. Given these results, an adequate mesh appears to be had with approximately 1.4 million elements. A similar sensitivity study was also performed for the tetrahedral interface meshes separately. The mesh sensitivity results presented here already feature these refined tetrahedral meshes. The 180 °C mesh containing 1.4 million elements is used for all test cases in the next chapter, and where necessary it is simply scaled up by a factor of 2.9 for the reactor test case, or mirrored and merged for full 360 °C test cases.

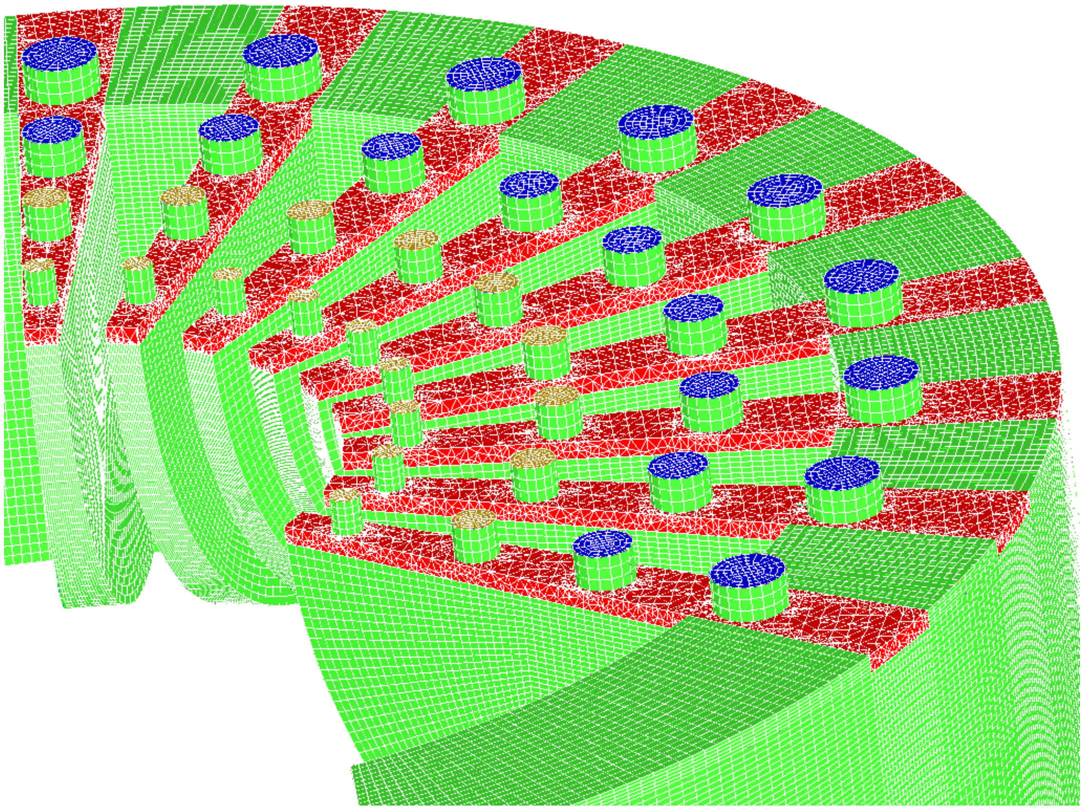

Figure 4.9: Tetrahedral interface meshes (colored red) situated beneath the round inlets of the lower plenum

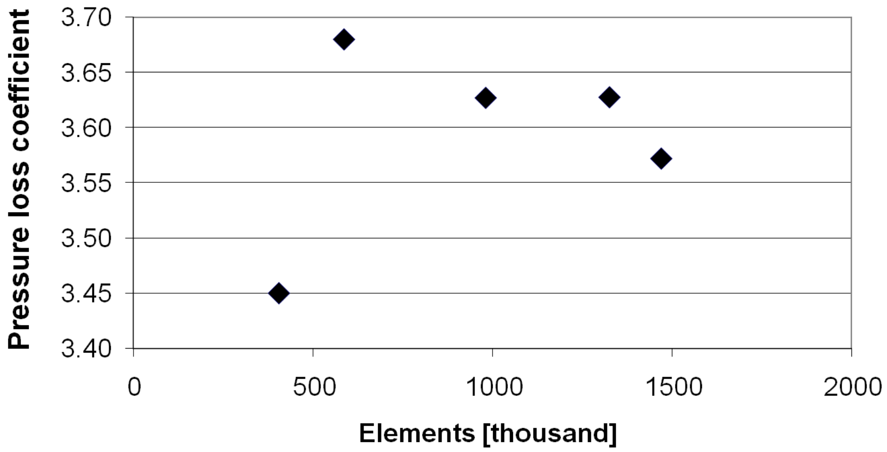

Figure 4.10: Mesh sensitivity of ξ

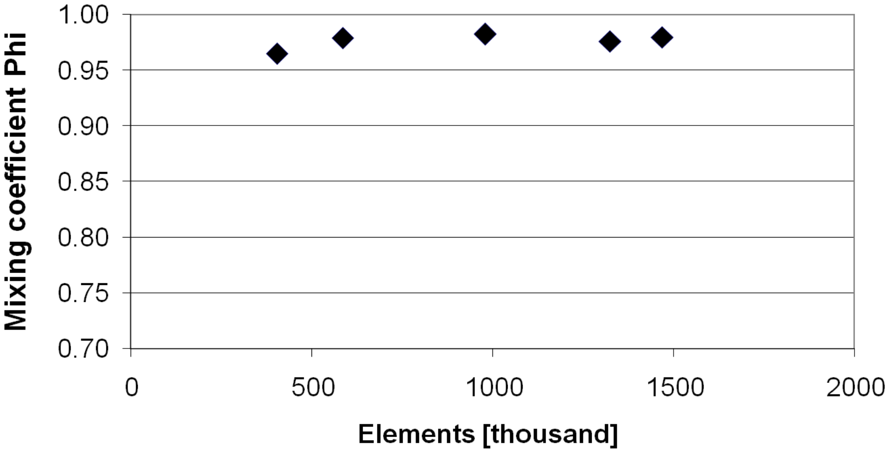

Figure 4.11: Mesh sensitivity of Φ calculated between inlet and outlet of the domain

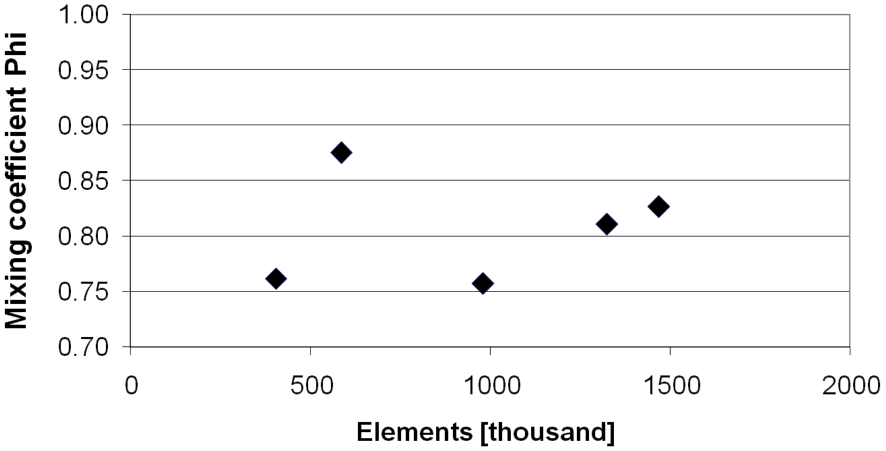

Figure 4.12: Mesh sensitivity of Φ calculated between inlet and start of the round outlet pipe

Chapter 5

Results

5.1 Validation

5.1.1 Steenbergen Experiments

Numerous experiments are available for validating turbulent closures for momentum transport in strongly swirling flows. These experiments can be grouped into several broad categories: 1) pipe flows with rotating walls, 2) rotating channel flows with stationary and moving boundaries, 3) stable and unstable swirling flows in long stationary pipes and 4) swirling flows in idealized combustor chamber geometries. A more detailed list and explanation of these experiments can be found in [26], [63] and [69]. Most of these swirling flow categories only cover fully developed solid body rotation type swirl flow, where the velocity component in azimuthal direction, u_φ can be described by $u_\varphi = cr$ with c being a constant and r being the distance from the swirl centerline. These solid body rotation type flows represent the swirl analogue to fully developed axial pipe flow. It should be noted that unlike fully developed axial pipe flow, the fully developed swirl flow in pipes decays over long distances as swirl momentum is dissipated via wall friction. The flow is fully developed in the sense that the shape $u_\varphi = cr$ of the velocity profile does not change any longer with respect to axial position.

Solid body rotation swirl flow is called fully developed since it is the condition of minimal potential (swirl) energy in swirling flow. It is the point of optimal stability into which swirl flow will develop over time. This can be quickly shown when considering the specific potential energy of a fluid particle rotating with angular velocity Ω:

$$e_{pot} = \frac{1}{2}\Omega^2 r^2 \tag{5.1}$$

taking the gradient of the specific potential yields the centripetal force experienced by a fluid particle

$$f_{centripetal} = \Omega^2 r = \frac{u_\varphi^2}{r} \tag{5.2}$$

Any fluid particle reducing its radius curvature of flow will experience an opposing force slowing it down, or an accelerating force when increasing curvature radius. Minimum viscous shear is achieved if $\frac{\partial^2 r u_\varphi}{\partial r^2} = 0$ which is the case for solid body rotation type flows with $\frac{\partial r u_\varphi}{\partial r^2} = \frac{u_\varphi}{r}$. Hence, a state of minimum energy, and that of highest stability, is achieved when the tangential component of swirling flow is equal to solid body rotation.

Since solid body rotation represents a case of minimal swirl energy, any numerical model achieving basic conservation of momentum will predict the shape of the velocity profile correctly, irrespective of turbulence intensity and turbulence closure models. For these kind of flows, the main effort in research is directed at proper modeling of near wall effects under swirl. Only if the swirling flow is turbulent and in an unstable state with significant deviation from solid body type rotation are models with more refined physical flow modeling necessary. Most practical flows exhibiting strong swirl usually exhibit this unstable state of swirl. Vortex shedding phenomena, swirl stabilized flames, cyclotrons or the flow investigated in this thesis, all belong to the category of unstable swirl. In the above list of experiments, unstable swirl is only the case for two categories: decay of unstable swirl in long stationary pipes and flows in idealized combustor chamber geometries. Due to the relative simplicity of the experimental setup, an experiment providing data for unstable swirl decay in a long round pipe has been selected. The selected experiments were performed and published by Steenbergen [63], and were chosen due to their relatively recent publication date as well as availability of turbulent data such as the individual Reynolds stress components $\overline{u_i' u_j'}$.

The CFD results for tangential velocity profiles using the SSG-RSM and k-ϵ model, which is a placeholder for several other linear viscosity models that performed nearly identically, such as k-Ω, SST and RNG k-ϵ, can be seen in figures 5.1 to 5.3. The error in predicting swirl decay as a function of the swirl number error $S_{error} = \frac{S_{CFD}}{S_{exp}} - 1$ over axial distance can be seen in figure 5.4.

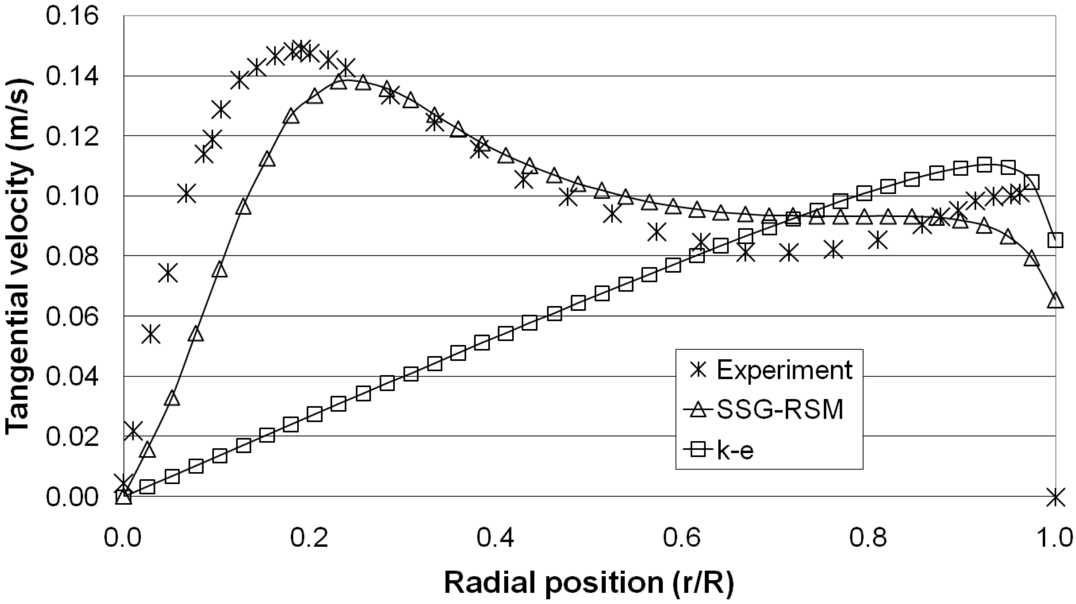

Figure 5.1: Tangential velocity against radial position at $x/D_j = 3.4$ for Steenbergen validation experiments.

Standard linear eddy viscosity models initiate an immediate vortex breakdown within the first pipe diameter of axial length due to the linear coupling of fluid shear strain with turbulent diffusion. The center region of the inlet consists of a highly concentrated swirling core with very high fluid shear strains being about one order of magnitude higher than in the near-wall region. Due to the linear coupling of this shear to turbulent diffusion, this region acts as a very large diffusion source of momentum “shuffling” momentum to the momentum sink close to the wall. Hence, within the first pipe diameter of axial length a fully developed solid body rotation flow is produced with these models. This performance is completely unsuitable to vortexes/swirl with high inertia, which are assumed to exist in the flow of the lower plenum of HTRs, and will cause a near instant attenuation of all vortices/swirl.

The SSG-RSM shows very good agreement with experiment until approximately $x/D_j = 15$, where it delays initialization of vortex breakdown until $x/D_j = 25$. This is a known issue of the SSG-RSM for weakly swirling flows

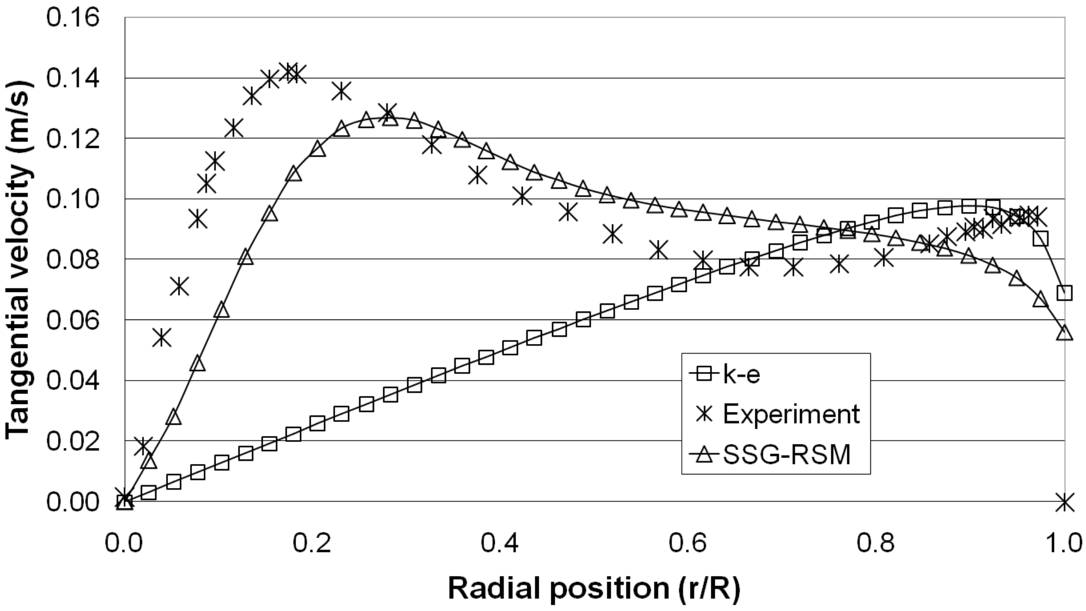

Figure 5.2: Tangential velocity against radial position at $x/D_j = 7.2$ for Steenbergen validation experiments.

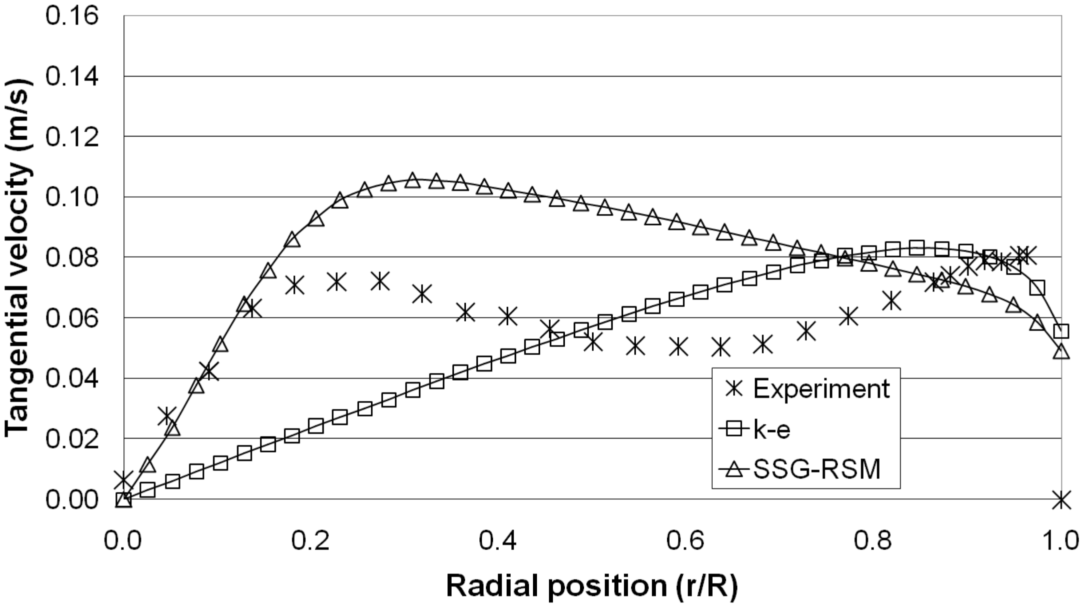

Figure 5.3: Tangential velocity against radial position at $x/D_j = 17$ for Steenbergen validation experiments.

the source of this error is due to the linear model of the rapid part of the SSG closure having a too weak response to streamline curvature (see Jakirlic et al.

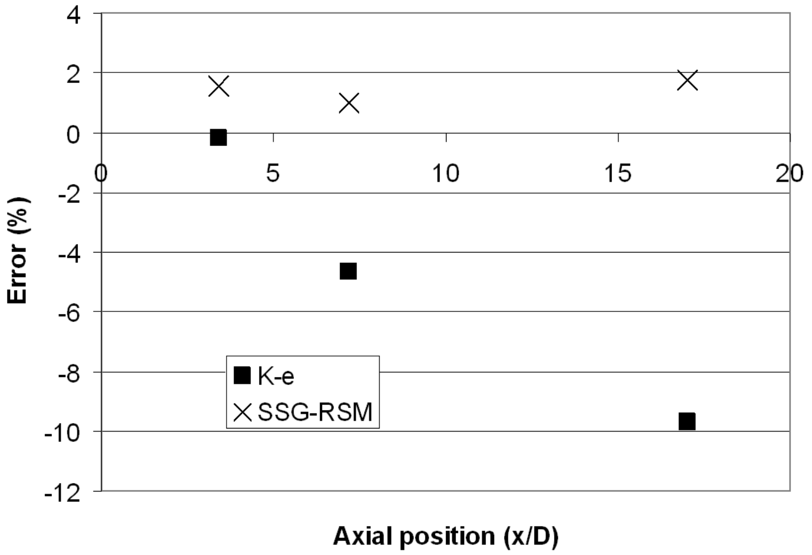

Figure 5.4: Swirl decay error against axial position for Steenbergen validation experiments.

[26]). The performance of the SSG-RSM may not be perfect, but it is a huge improvement over the standard linear eddy-viscosity models.

5.1.2 So et. al Experiments

Whereas there is a very large host of experiments available to validate the turbulent transport of momentum in swirling flows, the same can not be said for the turbulent transport of scalars in swirling flows. A total of only three well documented experiments could be found by the author in literature: A series of experiments performed by So et al. and Ahmed et al. [55; 64; 65; 66] on a model combustor, the weakly swirling, sudden expansion, model combustor experiment by Roback and Johnson [70] and the TECFLAM swirl burner experiments [71] investigating the precession movement of a vortex center. There is a number of swirling flame combustion experiments available where species concentrations as well as turbulent fluctuating scalar fluxes have been measured. These experiments can be discarded since, in the opinion of the author, errors introduced via turbulent combustion modeling will completely mask the performance of the underlying transport equations of momentum as well as species concentrations (scalars).

Of these experiments, those performed by So et al. are the most suitable to the case of the swirling flow in the lower plenum. These experiments offer in addition a wealth of publications where CFD simulations on this flow have been performed before hand, partially due to the very challenging nature of the investigated flow. A number of groups have simulated this flow with a full second order closure model (Reynold stress plus scalar flux transport equations), see Jester-Zrker et al. [25], Hogg et al [62], Ohtsuka et al [56] and Hirai and Takagi [45]. A number of non-linear eddy viscosity and eddy diffusivity models, see Jones [27] and Yang and Ma [72], both with rather poor agreement with experiment. Lastly, a high resolution LES was performed by Pierce and Moin [73], too.

The results are compared with experiments at three axial locations, $x/D_j = 3$, 5 and 10 respectively. Axial and circumferential velocity plots can be seen in figures 5.6, 5.7 and 5.8 for their respective x/D_j locations. Experimental helium mixture fractions were only available for $x/D_j = 5$ and 10 (figures 5.9 and 5.10). The velocity field of this experiment consists of broadly three radial regions, which need to be analyzed separately. In the center there is the helium- enriched jet decaying in axial direction. Surrounding this jet is a recirculation zone starting at the point from which the jet is inserted into the flow field and extending to roughly $x/D_j = 10 - 15$ where it reattaches. From this point onwards, the wake of the recirculation zone, with near zero axial velocity, extends beyond the measurement length of the experimental facility, and obviously of the CFD simulation domain, too. Due to the significant imposition of swirl onto this zone, this recirculation zone has a dampening effect on radial scalar trans-port of the central jet.

Around this zone is the bulk swirling flow, which is undergoing a transition from its initially unstable swirl structure, with high circumferential velocities close at the center line, to the stable condition of solid body rotation, with the bulk of all swirl momentum very close to the wall. The results show that the jet is predicted to decay too strongly in axial direction, as well as broadening too quickly in radial direction. This effect is well documented for turbulent free jets if unmodified general-purpose turbulence models are used, and a similar effect is assumed to happen in this flow.

The recirculation zone is located further toward the pipe walls than in the experiment. This is due to the over prediction of broadening of the jet as well as

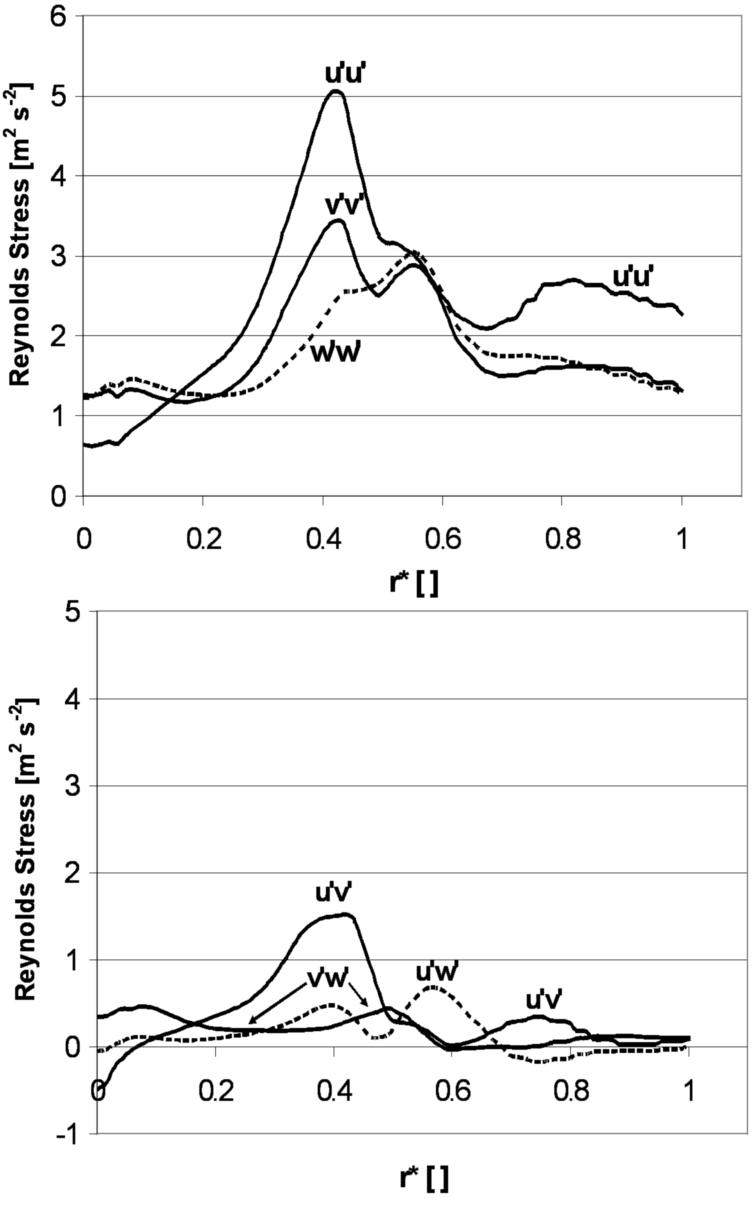

Figure 5.5: Reynolds Stresses generated for the inlet boundary condition of the experiments for the So et al. validation case

the bulk swirl flow transitioning too quickly toward solid body rotation, “pulling” the recirculation zone further outwards. The cause for this too fast transition of the bulk swirl flow lies in the over-production of turbulence, especially that of the $\overline{u'^2}$ component, within the interface between the recirculation zone and the bulk flow. This results in too high diffusion of momentum within that zone, causing swirl as well as axial momentum to be pushed into zones with lower diffusion

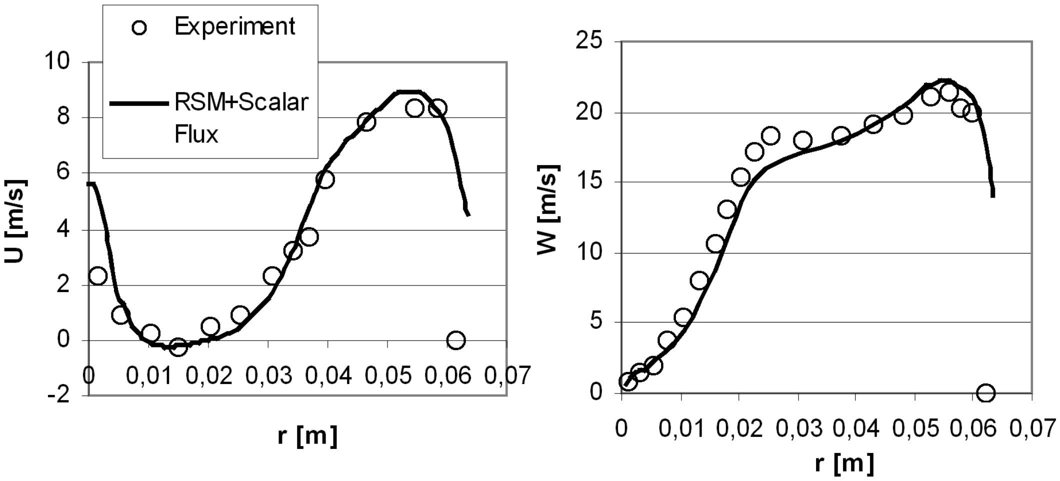

Figure 5.6: U and W velocities vs. r at x/Dj = 3 So et al. validation case

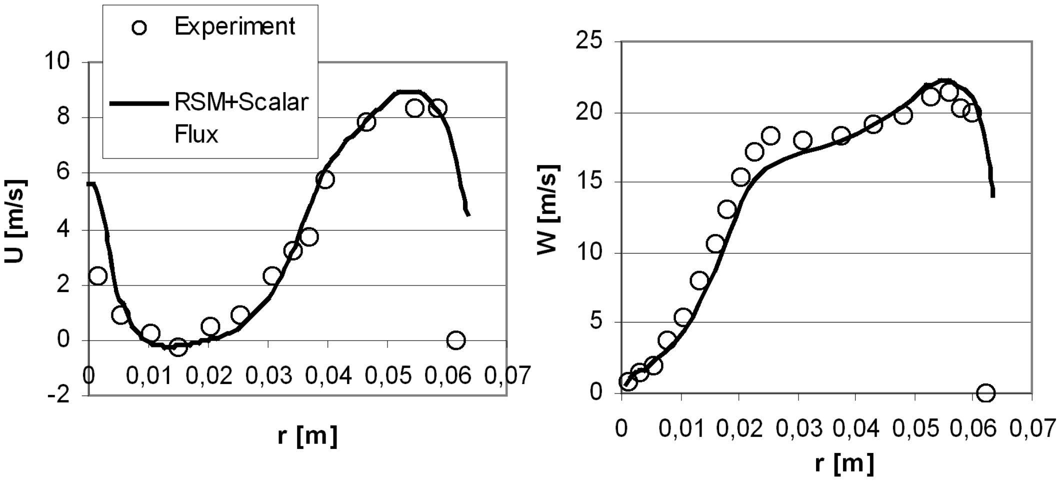

Figure 5.7: U and W velocities vs. r at x/Dj = 5 So et al. validation case

close to the pipe walls.

The reattachment point of the recirculating flow is located at $\approx x/D_j = 8$, which is in reasonable agreement with experiments. It must be noted that the location of this point, as well as the general strength of the recirculation zone, is highly susceptible to the pressure distribution located at the outlet boundary condition (BC). For example a Dirichlet velocity BC causes this point to not occur at all, extending negative axial velocities up to the outlet. The best fit with experiment was found by prescribing velocities directly onto the outlet. Since the

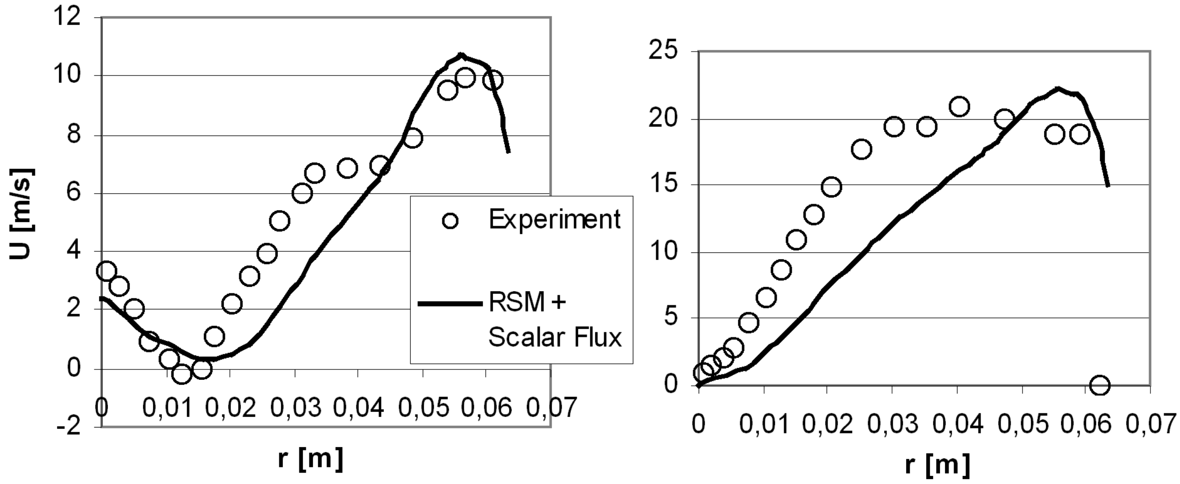

Figure 5.8: U and W velocities vs. r at x/Dj = 10 So et al. validation case

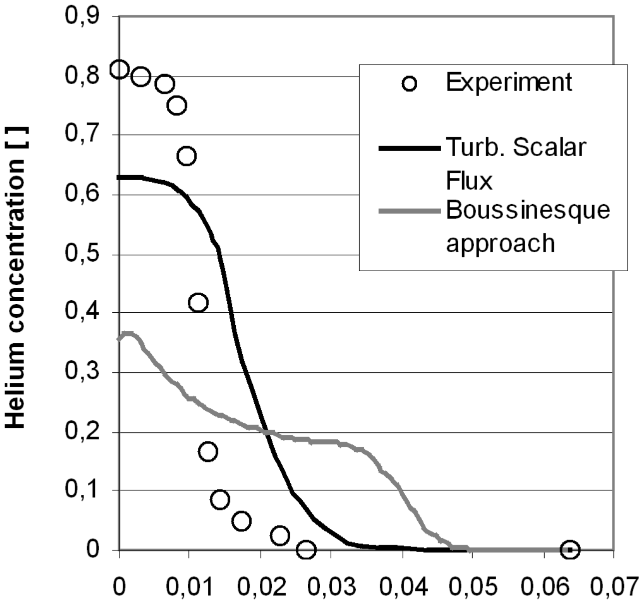

Figure 5.9: Helium concentration vs. r at x/Dj = 5 So et al. validation case

recirculation zone is interacting with the jet as well as the bulk swirl flow, minute changes in the pressure at the outlet BC can have very profound effects on the entire simulation. It is assumed that this sensitivity is caused by standard outlet boundary conditions (Diriclet as well as von Neumann) introducing errors due to pressure reflections from the BC. For example a correct far field pressure distribution cannot be achieved since near field pressure waves are reflected from the BC back into the domain. This issue is amplified by the fact that the recirculation

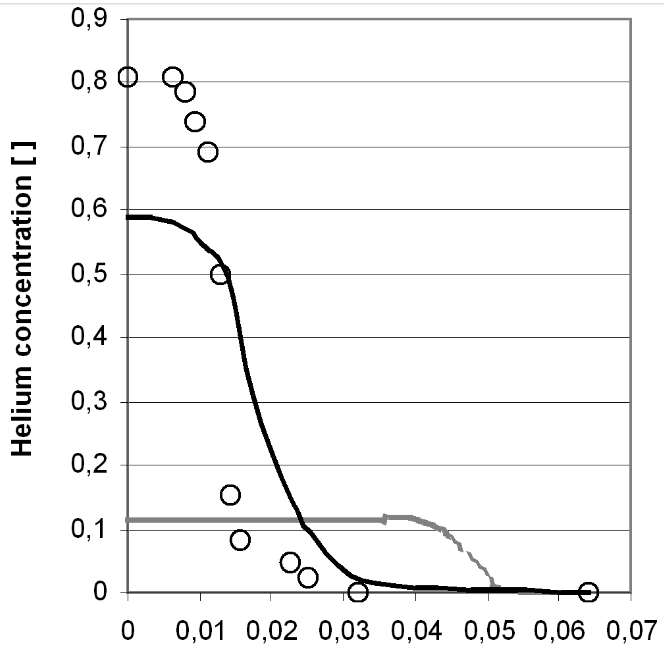

Figure 5.10: Helium concentration vs. r at x/Dj = 10 So et al. validation case

wake region, which is a local pressure minimum, extends beyond the outlet of the simulation domain. A non-reflecting pressure outlet boundary condition, as proposed for example by E. von Lavante et al. [74] would most likely improve results.

Despite the issues in predicting velocities accurately, the results for Helium mixing were in very good agreement with experiments considering that the Helium enriched jet is predicted to decay and spread too quickly. The results for Helium mixture fraction can be seen in figures 5.9 and 5.10. For comparison, the results are shown with the fully implemented scalar flux equations for turbulent transport of mixture fraction, and once with the standard turbulent Boussinesq-like approach. By implementing the full scalar flux equations, the inhibiting effect of swirl within the recirculation region on turbulent scalar transport is reproduced. The linear eddy diffusivity standard approach is completely lacking in this regard and Helium is transported near instantly across the recirculation region. The cause for this is found in the virtual turbulent viscosity being high in this region, while the spacial derivative of Helium concentration is high across this region, too. Hence the eddy diffusivity approach results in a maximum of turbulent diffusion across this region, while in reality the opposite is true.

In conclusion, it can be said that the additional modeling of the differential scalar flux transport equations improved the results of scalar mixing within the jet significantly. Significant deviations of the velocity flow field were observed within the recirculation region. The cause of this deviation is assumed to be due to pressure wave reflections from the BC back into the fluid domain. While the results do not match perfectly with the experiments, they do offer a significant improvement over linear eddy diffusivity models and linear eddy viscosity models.

5.2 Damm and Wehrlein validation cases

5.2.1 Overview

In order to avoid any confusion between the various test cases, the parameters used for the Damm and Wehrlein validation cases will be quickly outlined. The geometry dimensions can be taken from figures 2.1 and 4.6. The fluid is air at 1.3 bar, with the hot inlets at 60 °C and the cold inlets at 20 °C. The mass flow is varied as outlined in table 3. Due to the Mach number becoming greater than 0.3, the experiments, and hence the CFD validation, had to be stopped at the equivalent of only 50% nominal reactor mass flow. Due to the experiments by Damm and Wehrlein not mentioning any transient effect in the flow, all test cases discussed in this subchapter were simulated under the steady state assumption. Unless explicitly stated, all results discussed here were obtained from the simplyfied geometry employing 180 ° symmetry.

The main aim of the experiments by Damm and Wehrlein [5] were to measure mixing efficiencies Ψ as well as pressure loss as a function of Reynolds number in the lower plenum. Unfortunately, the experimenters did not provide information about the observed pressure losses in these air experiments. They only published in their figure 12 pressure loss values scaled to the real reactor flow of the HTR-Modul, while not describing their method of scaling. Due to the laws of scaling and dimensional analysis, the method of scaling is obviously limited to formulations using a pressure loss coefficient ξ and a comparison of scaled experimental values with those from CFD can be done on that basis. Due to some unexpected results observed in the pressure loss of the BenSaid cases, a discussion of pressure loss values for the D&W cases will be deferred until chapter 5.3.

5.2.2 Mixing efficiency

For Ψ (see equation 4.6), very significant differences between the simulation results using the various turbulence models could be found (see figure 5.11). The k-ϵ model coupled with the linear eddy-viscosity model produced unrealistic results which fail to show the diminishing Ψ value with increasing Reynolds numbers. Both Reynolds stress turbulence models were able to reproduce the trend of a decreasing Ψ with increasing Reynolds number. The RSM coupled with the linear eddy-diffusivity (LED) model predicted a decrease too steep in Ψ compared to experiments, while the agreement between experiment and the RSM with the full scalar flux model was very good. The reasons for these observed results will discussed in the following part. Figure 5.12 can be used for orientation and identification between different locations of interest within the lower plenum domain.

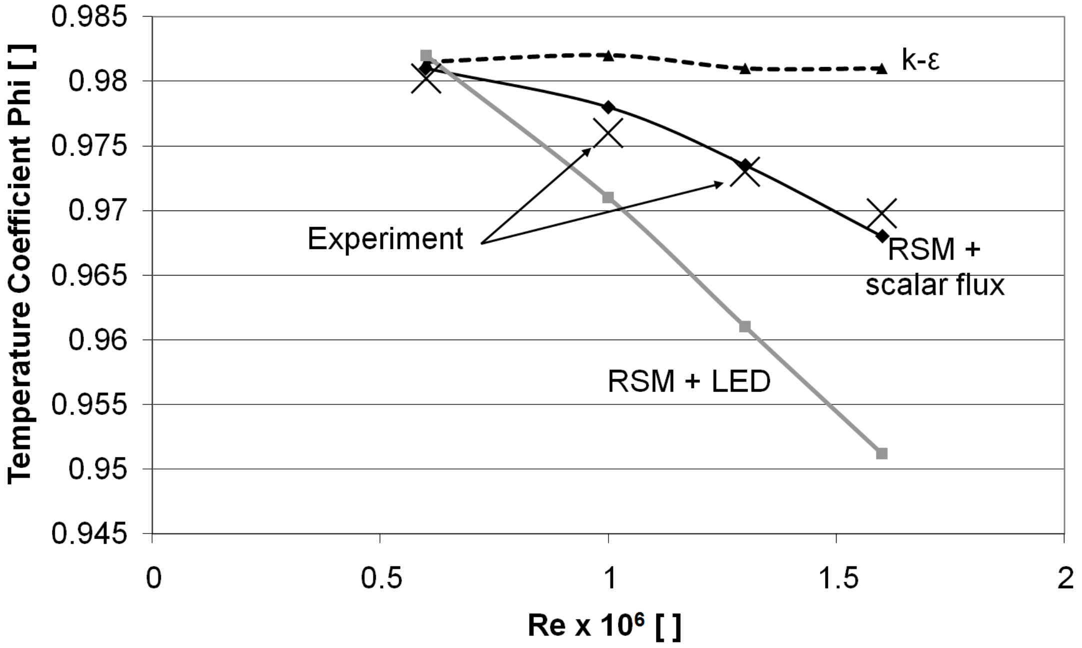

Figure 5.11: Variation of Ψ as a function of Re for the D&W validation cases

The unrealistic behavior of the k-ϵ model is due to the deficiency of this model with respect to swirling flows. In this type of flows, this model over predicts the generation of turbulence and hence causes excessive turbulent diffusion of momentum, and hence of enthalpy too, within the swirling regions. In this particular type of geometry, the k-ϵ model over predicts the diffusion of momentum within the individual ribs in the lower plenum chamber, causing complete damping of any swirling eddy motions within these ribs. Heat transfer between the hot and cold gases only occurs within a thin shear layer as can be seen in figure 5.13. In contrast, results using the RSM (figures 5.14 and 5.15) show that there are many small eddy motions within these narrow ribs causing a lot of mixing already to happen within the individual ribs. Due to the damping of these motions, the k-ϵ model under predicts enthalpy mixing by only allowing mixing to occur within a thin shear layer (compare figures 5.13 and 5.16 as well as table 4). On the other hand, the k-ϵ model over predicts mixing within the simple outlet pipe. It mixes here near perfectly with a Ψ value of 91%, whereas the experiments measured only 67% efficient mixing to occur within the pipe. This over prediction in mixing can be traced back to too strong generation of turbulence within the strongly swirling flow of the outlet pipe by the k-ϵ model. Due to the linear coupling of enthalpy diffusion with turbulent intensity k, the k-ϵ model is overpredicing the turbulent diffusion of enthalpy. This overprediction within the outlet pipe is so strong, that no matter how high the Reynolds number of the pipe flow is, the k-ϵ model always mixes the flow near perfectly within the outlet pipe. This purely numerical artifact is the most likely reason for the observed independence of Ψ from Reynolds number of the k-ϵ model.

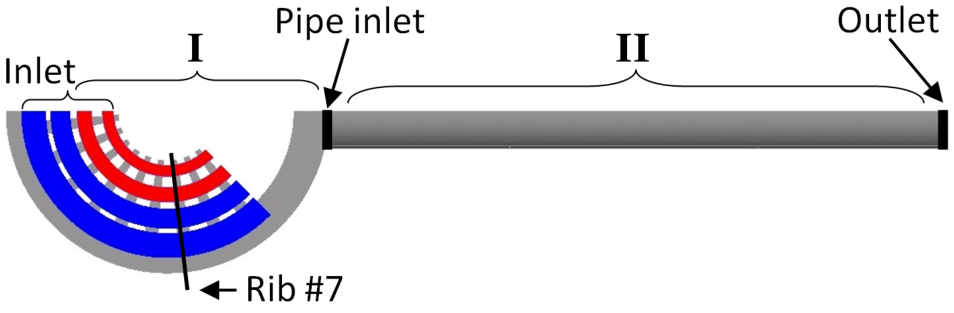

Figure 5.12: Location of rib number 7, and locations used for the definition of Ψ in table

Ψ-definition	region	RSM + LED	RSM + SF	experiment	k-ϵ
$\frac{\text{outlet}}{\text{inlet}}$	I+II	0.951	0.968	0.969	0.981
$\frac{\text{pipe outlet}}{\text{pipe inlet}}$	II	0.771	0.72	0.67	0.91
$\frac{\text{pipe inlet}}{\text{inlet}}$	I	0.786	0.815	0.84	0.768

Table 4: Ψ values at different locations for test case 1, locations see fig 5.12

As already mentioned above, the RSM turbulence models manages to predict the complex and intricate eddy flow within the ribs, as well as the annular collection chamber much better than the k-ϵ model. Similarly to the validation test case discussed in chapter 5.1.2, differences in velocity profiles between the LED model and full scalar flux model were nearly negligible. Yet, there were significant differences in the observed temperature profiles between both RSMs (figure 5.14

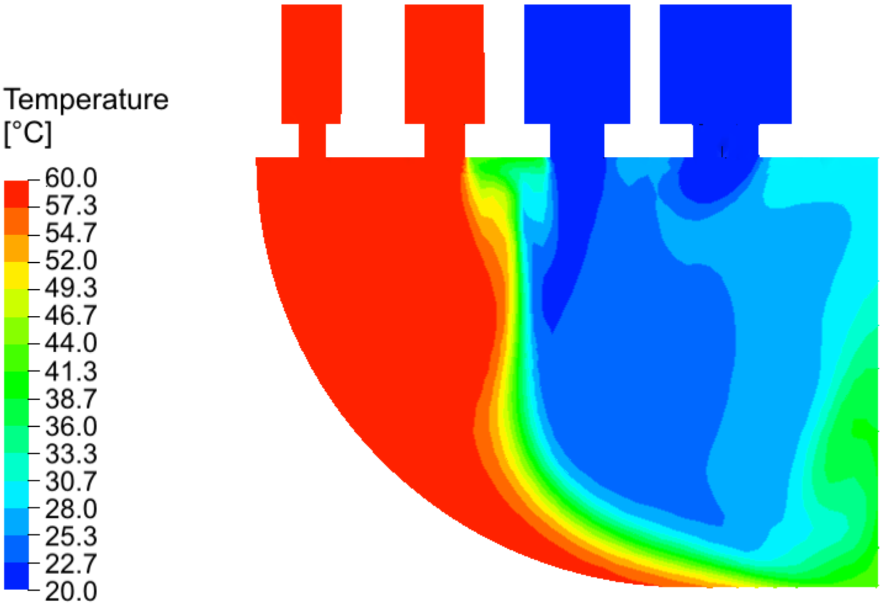

Figure 5.13: Temperature contour plot in rib 7 using the k-ϵ model

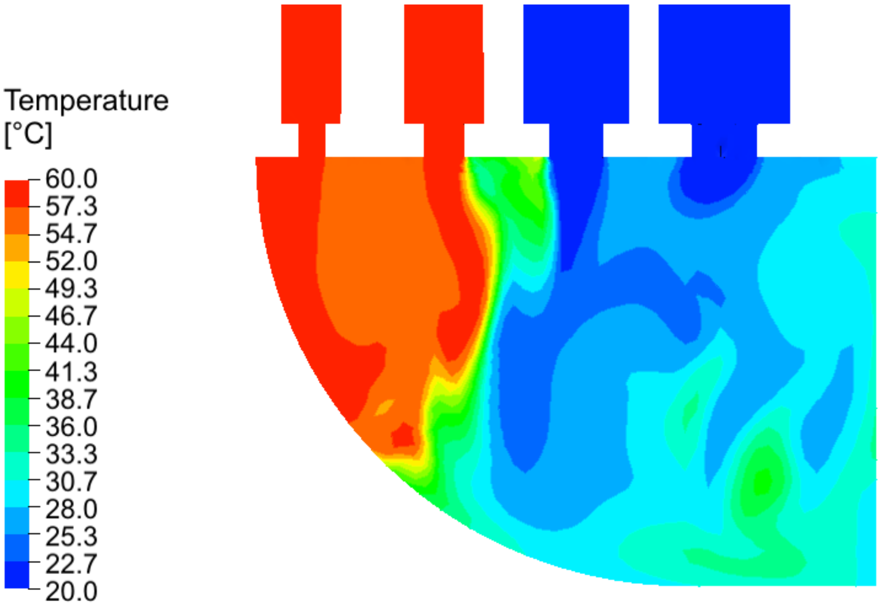

Figure 5.14: Temperature contour plot in rib 7 using the RSM plus LED model

and 5.15). There are minute differences within the turbulent enthalpy diffusion between both RSM models (figure 5.17 and 5.18). Besides of marginally higher rates of turbulent enthalpy diffusion and larger areas of strong turbulent enthalpy diffusion of the scalar flux model, the differences between both RSM models is

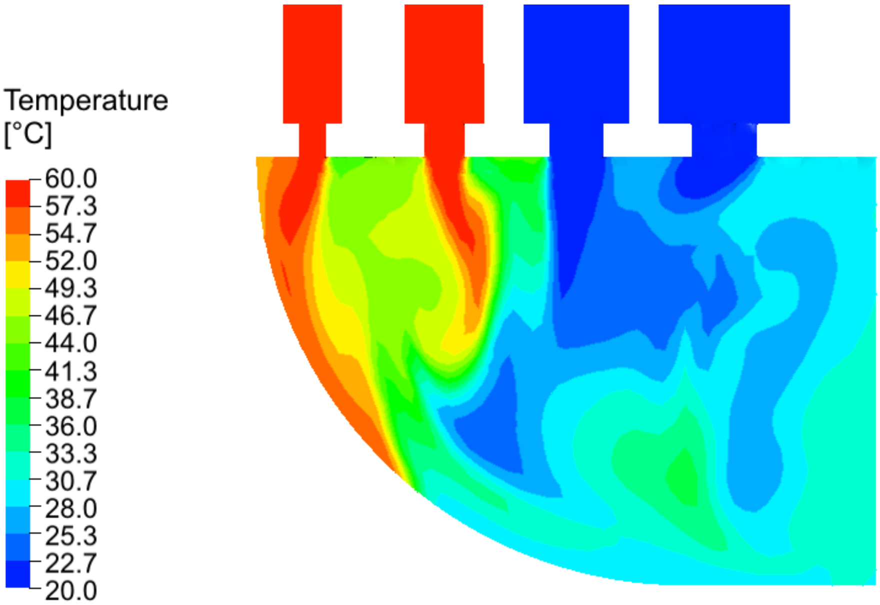

Figure 5.15: Temperature contour plot in rib 7 using the RSM plus scalar flux model

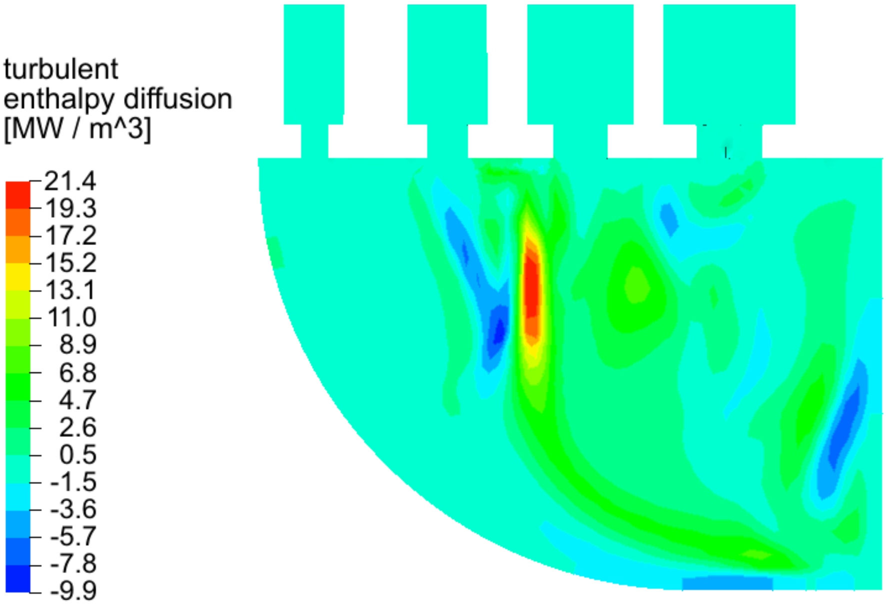

Figure 5.16: Turbulent enthalpy diffusion in rib 7 using the k-ϵ model. Red areas are heating up, while blue areas are cooling down

small. Unfortunately, no detailed velocity distributions have been measured in the experiments, so it can not be said with certainty whether the flow features computed by the RSM models are correct. Comparing the Ψ values with experi-

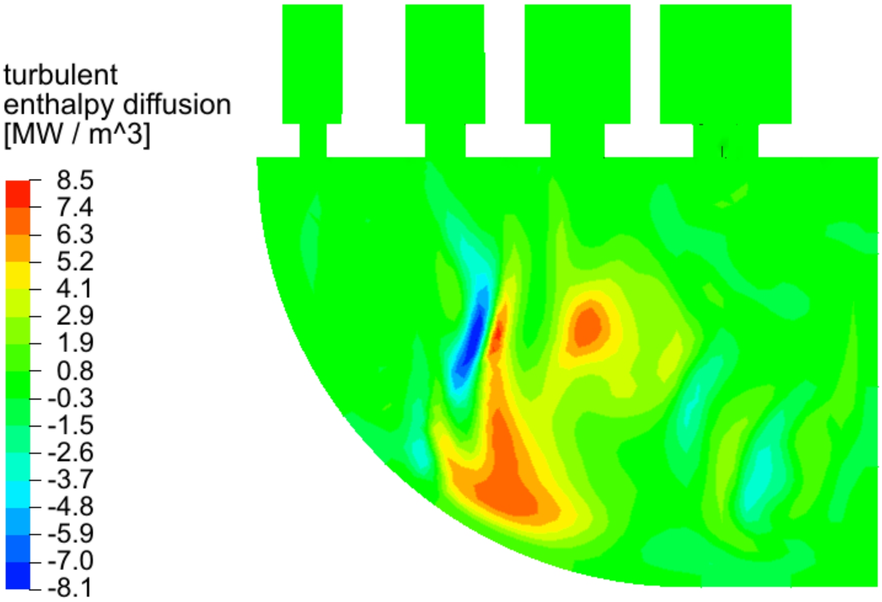

Figure 5.17: Turbulent enthalpy diffusion in rib 7 using the RSM plus LED model. Red areas are heating up, while blue areas are cooling down

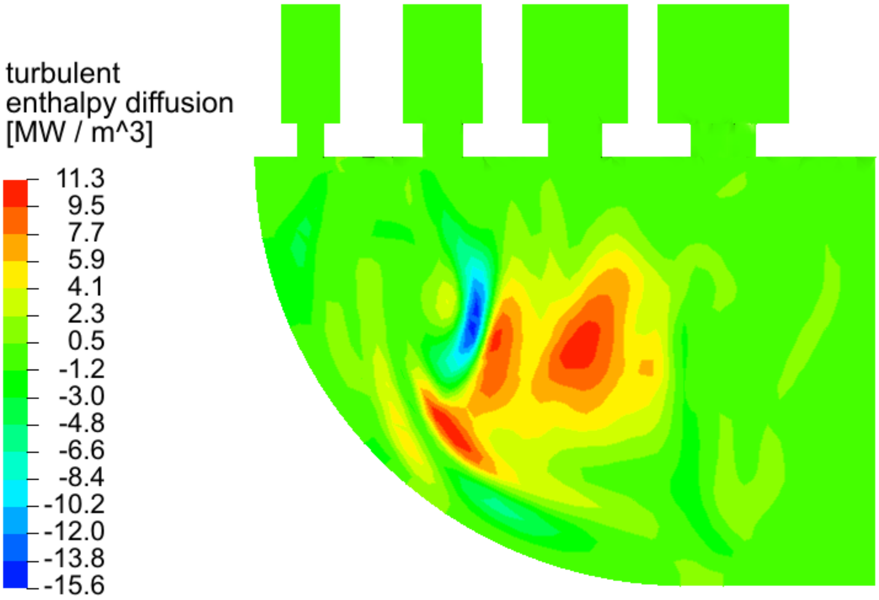

Figure 5.18: Turbulent enthalpy diffusion in rib 7 using the RSM plus scalar flux model. Red areas are heating up, while blue areas are cooling down

ments (see table 4 and figures 5.14, 5.15, 5.17 and 5.18) does show that the RSM model is calculating the integral Ψ values in agreement with experiments. The known deficiencies of the k-ϵ model as well as the correct prediction of Ψ with rising Reynolds number leads to the assumption that the physical characteristics of the flow calculated with the RSMs is closer to reality than the k-ϵ model. Hence, when discussing flow features within the lower plenum, implicitly only the RSM simulations are discussed, as the results of the k-ϵ model are assumed to not reflect reality.

5.2.3 Discussion of flow features

The difference between the two RSM turbulence closures for enthalpy transport needs to be investigated more closely, for which it is important to develop a detailed understanding of the underlying flow features. The general flow structure in the lower plenum can be seen in figure 5.19. Here, streamlines from the hot inlets of the four “ribs” the furthest away from the outlet pipe (ribs 1 to 4) are started. The color of the streamlines displays temperature. Here, one can see the accelerating nature of the main swirl vortex in the annular collection chamber. Interestingly, the core of the vortex is mainly accelerating in downstream direction while new flow coming from the ribs joins this main vortex with a swirl angle of approximately 45 °, meaning a swirl number of ∼1. This flow feature is not readily apparent in this streamline figure since the flow from the first set of ribs is mostly located in the center of this main vortex. Another interesting feature is the readily apparent strong mixing taking place already within the “rib”, and that the outer layers of the main vortex are heating up from the transfer of heat from new mass flow entering the annular chamber via further ribs in downstream direction.

Vector plots through the centerline of rib number 8 and 9 (the two ribs closest to the outlet pipe), as well as vector plots through the annular collection chamber with 7.5 ° separation angle from the two rib centerline plots can be seen in figures 5.20 and 5.21. One can see the main vortex structure in the annular chamber as well as the complex flow structures within a rib can be imagined. The biggest inlet jet cannot be seen in these centerline plots since it gets deflected downstream, i.e. into the paper, by the main annular channel flow. The remnants of this jet can be seen in the 7.5 ° separation angle plots below the large recirculation zone in the top left corner.

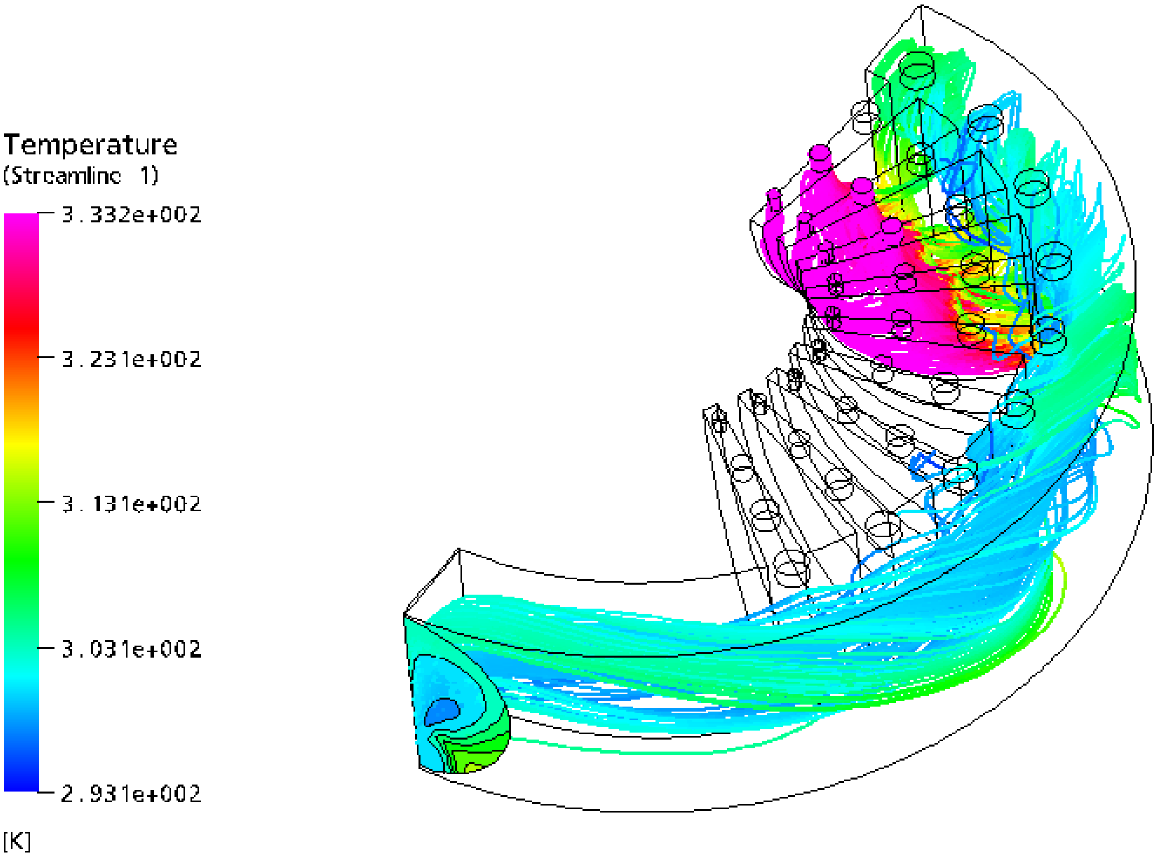

Figure 5.19: Streamlines starting from the hot inlets of the four ribs the furthest away from the outlet. Streamline color shows temperature

A major issue in analyzing these complex swirling flows, is their seemingly chaotic three dimensional nature, making it nearly impossible to capture all features in simple 2D-projections. A very powerful method for visualizing three dimensional swirl is the so called $\lambda 2$ criterion (see A.2). Iso-surfaces generated with this criterion identifies swirl centers and shows the structure of swirl. Such a plot for the lower plenum air flow can be seen in figure 5.22. Here, one can see the earlier mentioned behavior of new flow entering the annular chamber and joining with the main vortex with a swirl number of $\sim$1. Behind the main vortex, one can see strong flow detachment originating from the interaction of the inlet jet from largest inlet hole with the sharp corner of a rib. This flow detachment causes a slight blocking of the main vortex and forces some flow from the main vortex to separate and enter the rib. This diverted flow adds significant amounts of momentum into the volume of a rib, adding energy for complex small scale

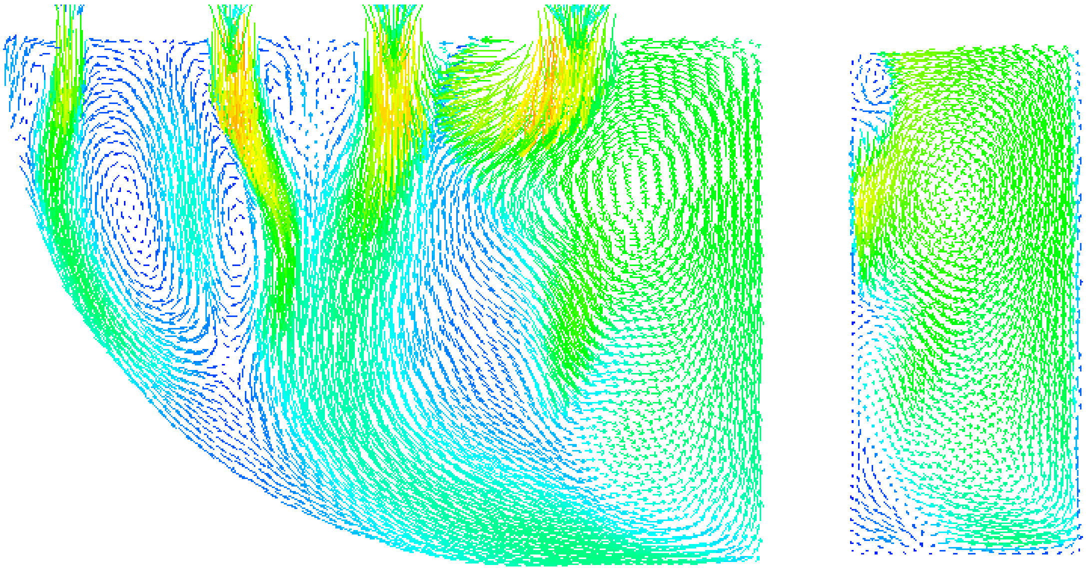

Figure 5.20: Vector plot in the center plane and directly downstream of rib no. 8. Vector colour is magnitude of velocity

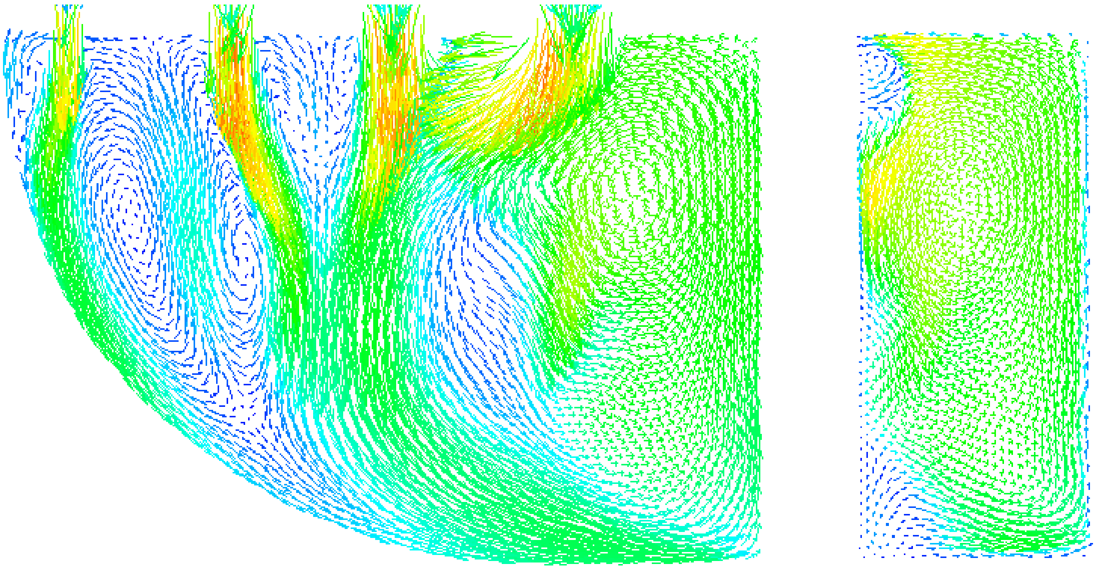

Figure 5.21: Vector plot in the center plane and directly downstream of rib no. 9. Vector colour is magnitude of velocity

eddy interactions within the rib, enhancing mixing significantly. These small scale eddies can be seen in the form of the "mass" of chaotic surfaces within each rib. This in the following few paragraphs this "chaos" will be investigated a bit more.

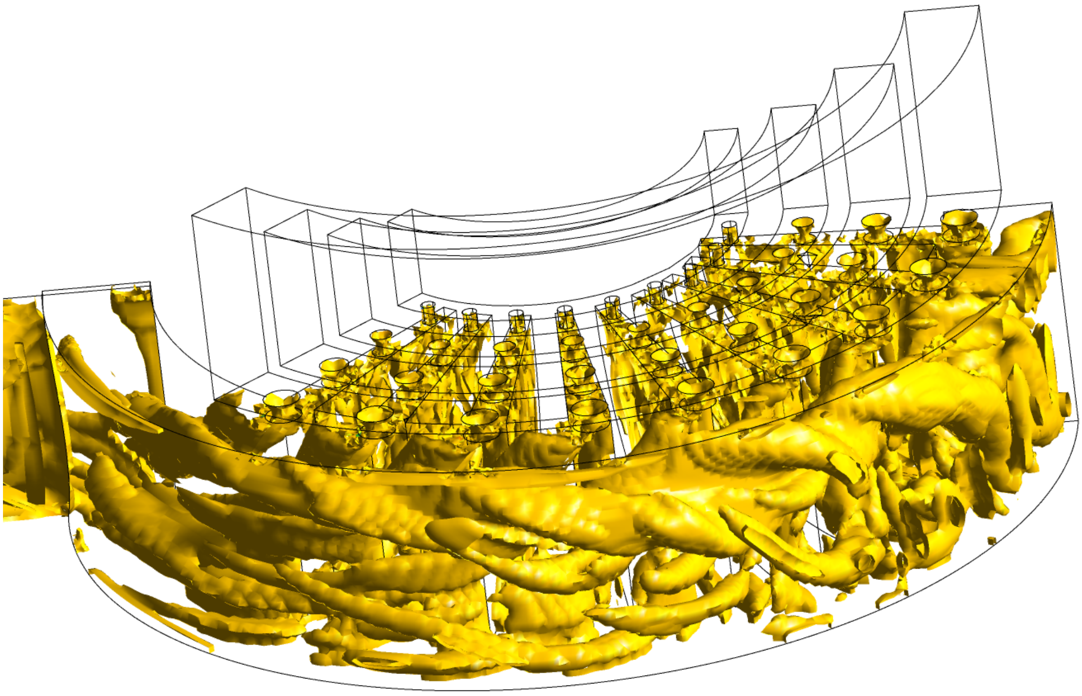

Figure 5.22: Plot of iso-surface of constant $\lambda2$ value for the air test case at $\mathrm{Re} = 1.6 \times 10^6$.

The flow within a rib is characterized by several thin flow layers flowing past each other and interacting with each other by forming weak vortices. This folding motion of thin fluid layers is highlighted in the streamline plots of figures 5.23 and 5.24. In figure 5.23, the flow structure of the two hot inlets of one rib are displayed via streamlines. In figure 5.24 the flow emanating from the two cold inlets of the same rib are shown, and one can easily see how one of the cold inlet jets is split in half and interacts with one of the hot inlet jets. This complex motion is also highlighted in figure 5.26, which is a combination of streamlines with a vector plot in the central plane of a rib. Streamlines as well as vectors are colored in temperature, and one can for example see the strong main swirling motion in the top of the annular collection chamber. Just to give an idea of the complexity of flow, in figure 5.27 iso-surfaces of constant $\lambda2$ are shown for the same rib and flow as in figure 5.26.

The scalar flux model produces more turbulent diffusion of enthalpy than the LED model within the ribs and annular collection chamber mostly due to two reasons: Firstly, within a rib the swirling flow often the center of the swirling motion is colder than its periphery. Due to density differences, centrifugal forces will slightly increase enthalpy diffusion. This can only be modeled via full scalar flux transport equations. Secondly, one is faced with a distinct separation of turbulent momentum intensities and scalar flux intensities in areas of low shear. This effect is especially pronounced and can be seen in the right upper corner of figures 5.14 and 5.15 between the two hot inlet jets. The scalar flux model enhances the turbulent diffusion of enthalpy even though the fluid shear rates are very low in this recirculation region. For the outlet pipe, on the other hand, the scalar flux model is inhibiting the diffusion of enthalpy within the strongly swirling outlet pipe flow, reproducing experimental values very well.

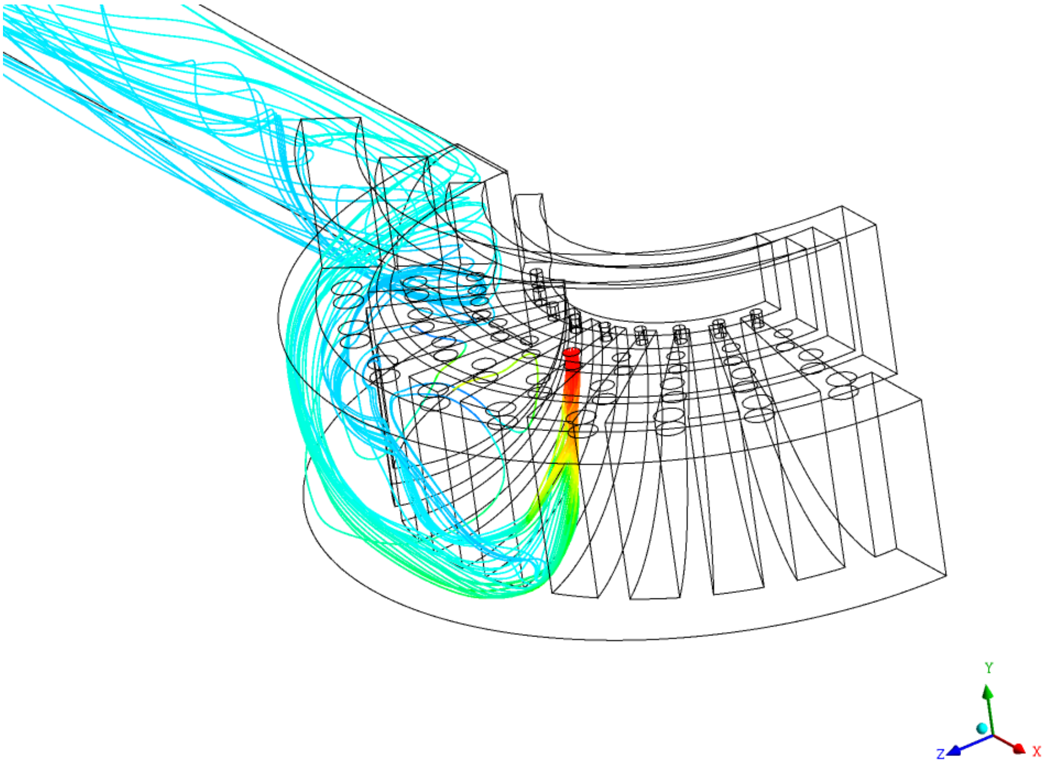

Figure 5.23: Streamlines starting from the two hot inlets of a rib. Streamline color shows temperature

The flow in the outlet pipe can be seen in figure 5.25. In this figure, four cut-through sections with vector plots of the flow are shown. They are ordered from left to right, top to bottom in direction of flow. The first cut-through is located exactly at the start of the outlet pipe, with the following 3 cut-throughs

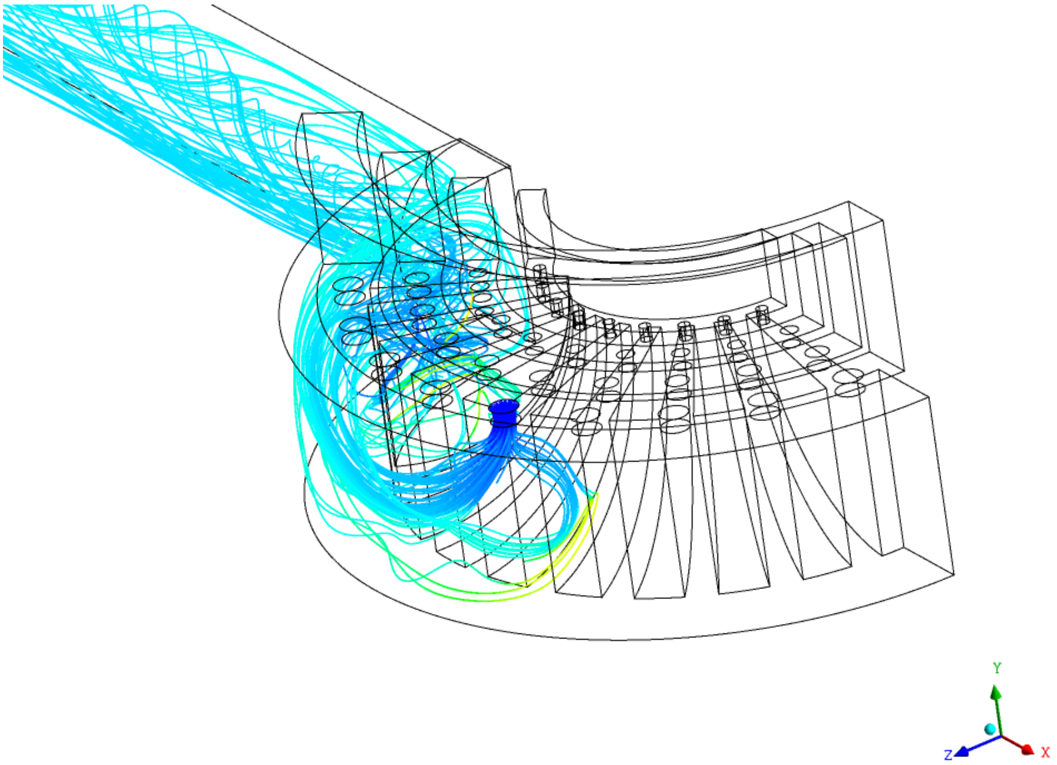

Figure 5.24: Streamlines starting from the two cold inlets of a rib. Streamline color shows temperature

being separated by 0.2 m downstream in axial direction. In the first cut-through one can see a large zone of detaching flow forming due to the sharp corner at the inlet of the pipe. The main vortex of the annular channel is forced downwards toward the wall due to coriolis forces acting on this vortex being bent by 90 ° into the pipe. This vortex remains within the entire length of the outlet pipe and it is observed to precess in an anti-clockwise direction along the pipe walls and symmetry plane of the outlet pipe.

As concluding remarks about the air test cases, it should be mentioned that simulations were also performed with a full 360 ° geometry without any symmetry simplifications. Besides of some minor deviations within the outlet pipe, the steady state solutions for the full 360 ° geometry was surprisingly mirror symmetrical throughout the lower plenum. No mass flow bias to any side could be noticed, and even flow details within individual ribs were mostly mirror symmetrical. No significant deviations for Ψ as well as ξ could be observed when compared to the above 180 ° partial geometry.

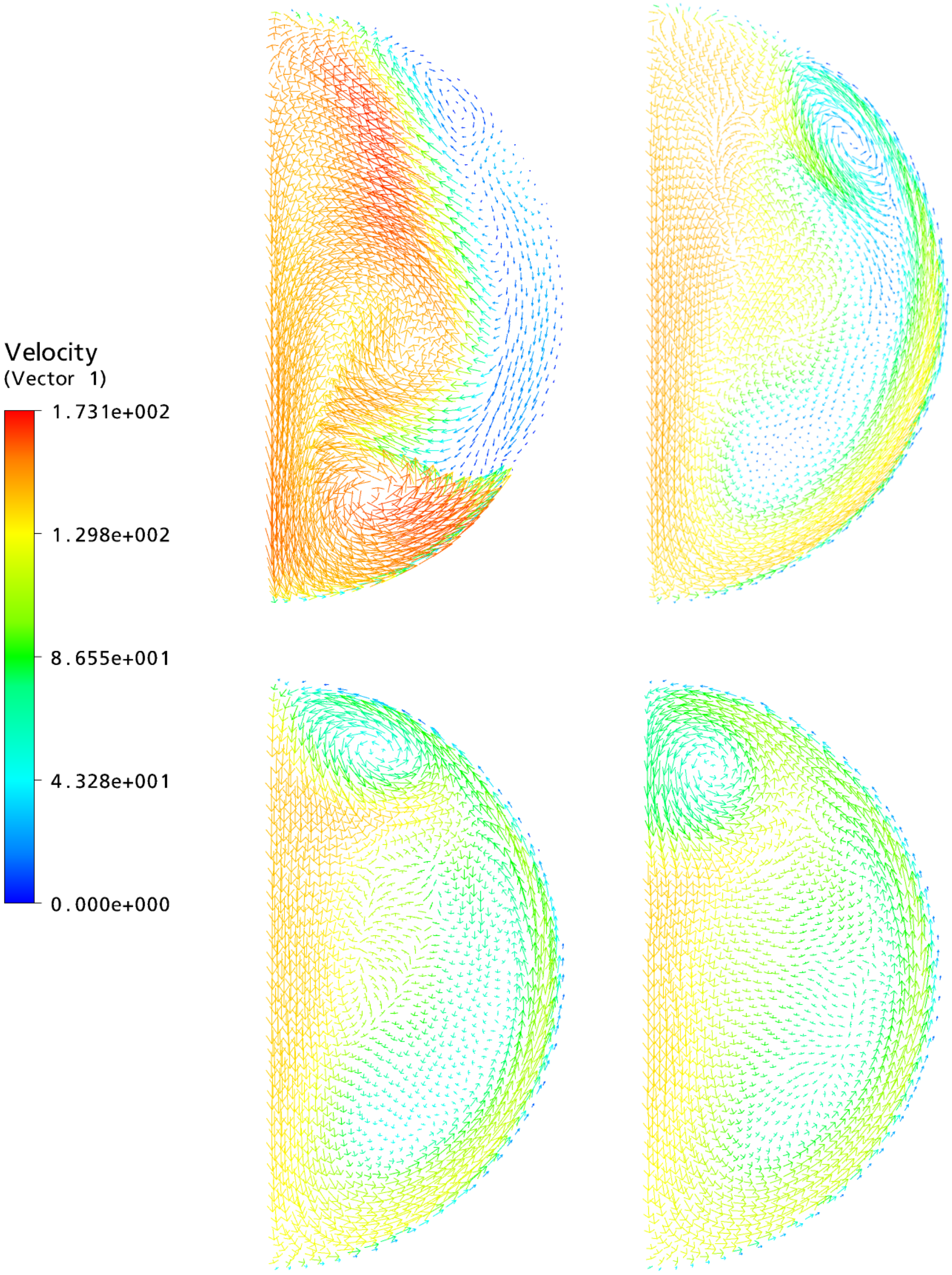

Figure 5.25: Vector plots of several cut-throughs of the outlet pipe in downstream direction. Pictures are ordered from left to right, top to bottom and are separated by 0.2m in downstream direction of the pipe.

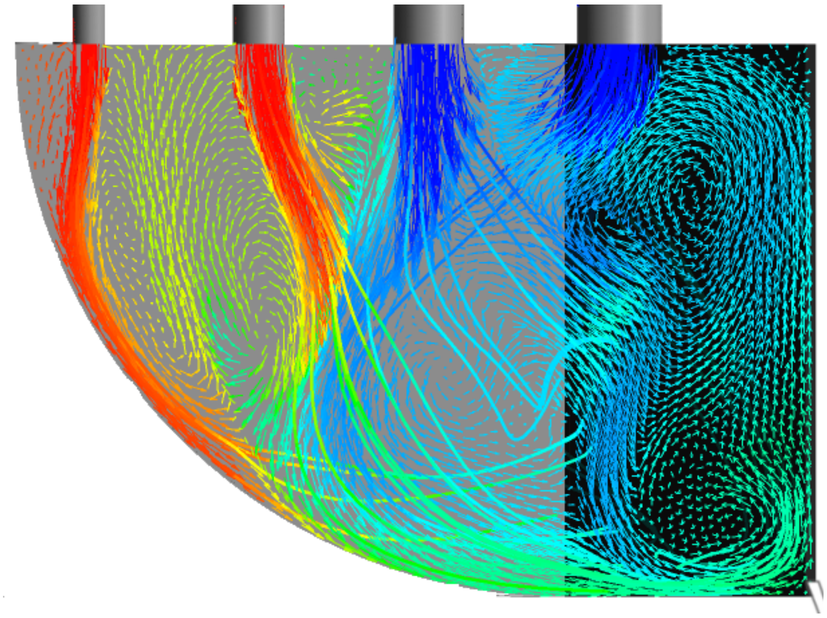

Figure 5.26: Combined streamline and vector plot of the flow within a rib. Streamline color as well as vector color shows temperature

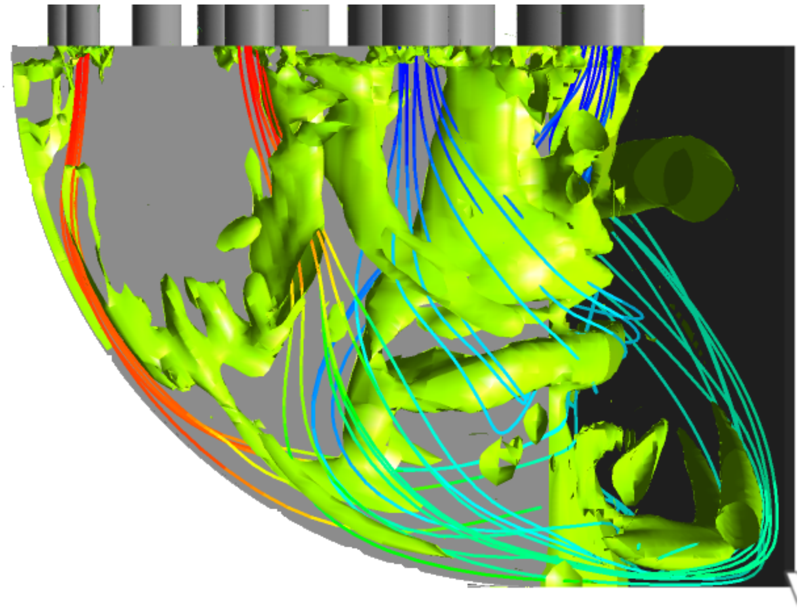

Figure 5.27: Combined streamline plot with iso-surfaces of constant $\lambda2$. Areas enclosed by the isosurfaces indicate swirl centers

5.3 BenSaid reactor cases

5.3.1 Overview

With the agreement between experiments and CFD being very good for the air test cases, the next step could be taken with the now well validated models and tools: the modeling of the lower plenum with conditions similar to a real reactor. The working fluid is helium at 60 bar and the “cold” inlet temperature is 600 °C and the hot inlet temperature is 800 °C. The dimensions of this geometry are similar to the D&W validation cases, with the only difference being an increase in size by a scaling factor of 2.9. Due to the maximum velocity of the flow approaching $\mathrm{Ma} = 0.3$ for air in the D&W case at $\mathrm{Re} = 1.6 \times 10^6$, the CFD calculations as well as the air experiments by Damm and Wehrlein had to be stopped at $\mathrm{Re} = 1.6 \times 10^6$ to maintain flow similarity with the helium flow of the HTR-Modul reactor (compressibility effects at $\mathrm{Ma} > 0.3$ would have prevented this). This is equivalent to 50% power of the full reactor. Due to different fluid properties of helium, the Mach number within the HTR-Modul reactor at 100% power is only 0.03.

5.3.2 Pressure loss

As indicated in the previous chapter, the first focus will be placed on pressure loss within the lower plenum. Expressing the non-dimensional pressure loss in dimensionless form as $\xi = \Delta P/\rho U^2$ one is confronted with the startling result that the pressure loss coefficient for the BenSaid cases is systematically 10% higher than that for the air based D&W validation as well as the experimental results of D&W. This result is reproduced to 0.5% accuracy no matter which turbulence model is used. This result is surprising since the D&W experiments have been scaled by Damm and Wehrlein according to dimensionless number theory, with similarity achieved for Re, Pr and Ma.

The reason for this discrepancy does not have anything to do with the fluid properties of Helium. The Prandtl number is almost identical for air and helium in this case. The differing molecular dynamics of helium being a mono-atomic gas with $\kappa = 5/3$ as opposed to the di-atomic gas mixture of air with $\kappa = 7/5$ are irrelevant for the lower plenum flow. There is simply no significant amount

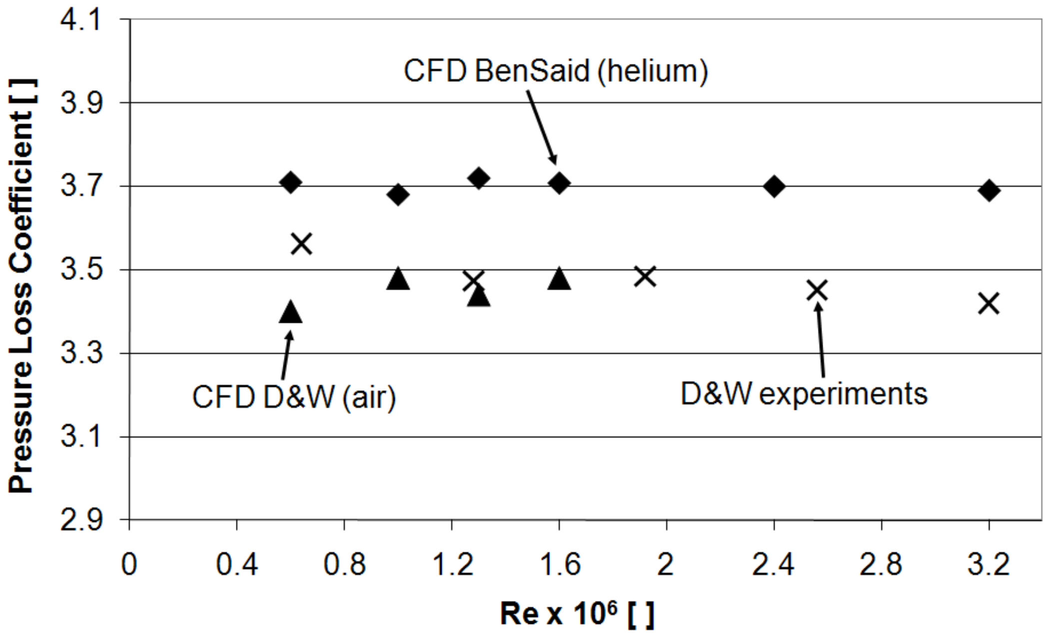

Figure 5.28: ξ against Re for the D&W cases, Bensaid cases and experimental results of D&W

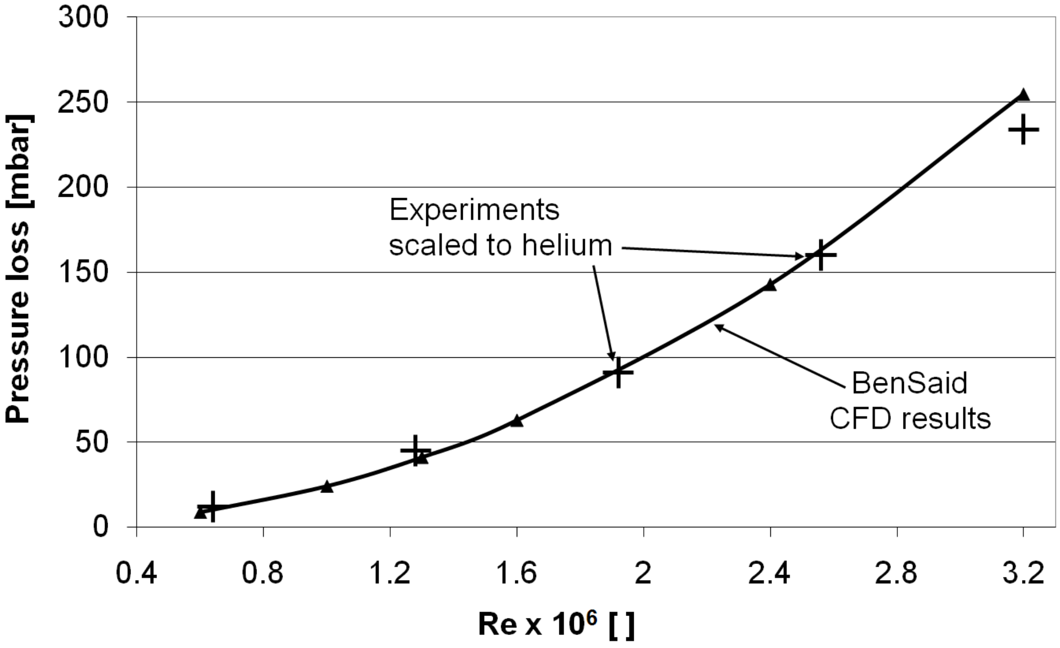

Figure 5.29: Comparison of absolute pressure loss between CFD and experiment as a function of Re

of thermodynamic work performed by the fluid where these differences would matter. The absolute pressure drop is 0.25 bar compared to a system pressure of 60 bar.

The reason for this discrepancy lies in the ratio of densities of hot and cold gas $\gamma = \rho_{cold}/\rho_{hot}$. When inspecting the Navier-Stokes equations and the passive scalar transport equation, there is no term where γ might have any influence. Only when the influence of time-averaging is accounted for (which always occurs when observing turbulent flows), do terms with $\partial\rho/\partial x$ appear in the transport equations. The reader is referred back to equations 3.17, 3.19, 3.23 and 3.26 for more detail. In the air experiments by Damm and Wehrlein $\gamma = 1.13$ while for the BenSaid HTR-Modul cases $\gamma = 1.23$. It should be noted, that the BenSaid case temperature difference used in this thesis for the HTR-Modul is somewhat different to those of the HTR-Modul which Damm and Wehrlein used (the temperature values there led to $\gamma = 1.17$). This is due to a significant underestimation of temperature differences of helium leaving the reactor core in the case of the original HTR-Modul design analysis. The BenSaid case and its temperatures reflects the current best estimate of these temperature differences. Additionally, when making a dimensional analysis of this flow, the Eckert number remains when extracting Pr and Re from the transport equations. The Eckert number is defined as follows:

$$\mathrm{Ec} = \frac{U^2}{c_p \Delta T} \tag{5.3}$$

and expresses the relationship of kinetic energy to enthalpy in a flow. The Eckert number is used to describe dissipative heating of fluids, and is in the case of highly turbulent convective fluids basically irrelevant. The ΔT in the Eckert number definition only describes the heating effect due to viscous dissipation, which can be estimated for a fluid in laminar flow via $T^* = 1/2\mathrm{Pr}\ \mathrm{Ec}$ with $\mathrm{Ec} = U^2/c_p\, T_{ref}$. It should be noted that for estimating the heat-up due to viscous forces As one can quickly see, the effect is negligible for gases with Prandtl numbers in the region of 0.7. Yet, the Eckert number does provide the useful insight that for the lower plenum flow, the characteristics of flow are vastly different when considering air or helium test cases. Given a Reynolds number of 1.6×10^6 in the outlet pipe, for air the Eckert number is equal to 0.16 while for Helium the Eckert number is equal to 0.0011. This means that in the air experiments vastly more energy is transported in the form of kinetic energy than in enthalpy compared to the helium cases.

The relevance of the discrepancy in the Eckert number is still debatable since subsequent CFD simulations on modified flow cases of the D&W experiments, where γ has been matched to that of the BenSaid reactor ($\gamma = 1.23$), produced ξ values equal to 3.69 for all relevant Reynolds numbers. The matching was achieved by setting the hot air temperature to 101 °C and subsequent small changes to mass flow Re matching. With this change, perfect similarity between the modified D&W experiments and the BenSaid reactor has been achieved for ξ. This indicates the importance of matching γ in the case of turbulent, variable-density flows. While this is a strong indicator that γ is highly relevant for this flow, only a detailed non-dimensional analysis of this flow can offer insight into issue of similarity between air experiments and the helium reactor flows.

Fundamental to performing a non-dimensional analysis is the determination of independent variables describing the problem. Since this is a flow with thermal mixing, the following basic variables as well as fluid properties can be chosen for transforming the Navier-Stokes equations into a non-dimensional form:

$$\text{characteristic length scale:} \quad L\ [m] \tag{5.4}$$

$$\begin{aligned} \text{characteristic velocity:} &\quad U\ [\tfrac{m}{s}] \\ \text{fluid viscosity:} &\quad \mu\ [\tfrac{N\,s}{m^2}] = [\tfrac{kg}{m\,s}] \\ \text{fluid thermal conductivity:} &\quad \lambda\ [\tfrac{W}{m\,k}] = [\tfrac{kg\,m}{s^3\,k}] \\ \text{fluid specific heat capacity:} &\quad c_p\ [\tfrac{J}{kg\,k}] = [\tfrac{m^2}{s^2\,k}] \end{aligned} \tag{5.5}$$

Additionally, a variable describing the drop of pressure within the domain would of use:

$$\text{relative pressure drop:} \quad \Delta P\ [\tfrac{N}{m^2}] = [\tfrac{kg}{m\,s^2}] \tag{5.6}$$

The last group of independent variables is related to temperature and density, describing the actual thermal mixing within the lower plenum. Given the ideal gas law

$$P = \rho \frac{R}{M} T \tag{5.7}$$

with R being the universal gas constant and M being the molar mass of the gas, one can quickly arrive at a correlation relating temperature fluctuations in terms of density at constant pressure:

$$\frac{\Delta T}{T_{ref}} = \frac{\rho_{ref}}{\Delta \rho} \tag{5.8}$$

Hence, any thermal mixing at constant pressure can be sufficiently described if any three of the four variables of equation (5.8) are chosen. For this non-dimensional analysis the following variables were selected:

$$\begin{aligned} \text{characteristic temperature difference:} \quad & \Delta T \; [K] \\ \text{reference density:} \quad & \rho_{ref} \; [\tfrac{kg}{m^3}] \\ \text{characteristic density variation:} \quad & \Delta \rho \; [\tfrac{kg}{m^3}] \end{aligned} \tag{5.9}$$

This results in 9 independent variables with 4 independent SI units (kg, m, s, k). According to the first Buckingham Π theorem, this physical problem can be sufficiently described via $9 - 4 = 5$ independent Π groups of non-dimensional variables. Using the second Buckingham Π theorem one can derive a group of non-dimensional variables. For this, the following four repeating variables which cannot form a Π group are selected: L, U, c_p and ρ_{ref}. For the first Π group,

$$\Pi_1 = f(L, U, c_p, \rho, \mu) \tag{5.10}$$

resulting in

$$\Pi_1 = \frac{\rho\, U\, L}{\mu} = \mathrm{Re} \tag{5.11}$$

In short form, the other four Π groups can be formed as follows:

$$\begin{aligned} \Pi_2 = & \quad f(L, U, c_p, \rho, \lambda) \\ & \Rightarrow \Pi_2 = \tfrac{L\, U\, \rho\, c_p}{\lambda} = \mathrm{Re}\,\mathrm{Pr} = \mathrm{Pe} \\ \Pi_3 = & \quad f(L, U, c_p, \rho, \Delta T) \\ & \Rightarrow \Pi_3 = \tfrac{U^2}{c_p\, \Delta T} = \mathrm{Ec} \\ \Pi_4 = & \quad f(L, U, c_p, \rho, \Delta P) \end{aligned} \tag{5.12}$$

$$\begin{aligned} & \Rightarrow \Pi_4 = \tfrac{\Delta P}{\rho U^2} = \mathrm{Eu} \\ \Pi_5 = \quad & f(L, U, c_p, \rho, \Delta\rho) \\ & \Rightarrow \Pi_5 = \tfrac{\rho}{\Delta\rho} = \gamma \end{aligned}$$

A summary of this analysis is given in table 5 below. The determinant of the resulting matrix of all dimensionless parameters is -4, indicating that the correlations found here are not singular. Of great interest is that now, ξ can be easily shown to be a function of $\xi(= \mathrm{Eu}) = f(\mathrm{Re}, \mathrm{Pr}, \mathrm{Ec}, \gamma)$ only. From the previous CFD calculations, and more importantly, from the experimental results of D&W, it appears that the correlation between ξ and Ec is very weak. This can be seen in figure 5.28, where ξ appears to not be a function of Re. Since the only common independent variable between Ec and Re is U, this is only possible if ξ is correlated such that $\xi = f(\mathrm{Re}\,\mathrm{Ec}^{-0.5}, Pr, \gamma)$. From this analysis it can be seen that γ is of great importance for achieving flow similarity of thermal mixing within the lower plenum, especially for estimating the pressure loss coefficient.

		ΔT^a	λ^b	μ^c	ΔP^d	$\Delta\rho^e$	L^f	U^g	c_p^h	ρ^i
		$[K]$	$[\frac{kg\,m}{s^3\,k}]$	$[\frac{kg}{m\,s}]$	$[\frac{kg}{m\,s^2}]$	$[\frac{kg}{m^3}]$	$[m]$	$[\frac{m}{s}]$	$[\frac{m^2}{s^2\,k}]$	$[\frac{kg}{m^3}]$
K	$0 =$	1	-1	0	0	0	0	0	-1	0
m	$0 =$	0	1	-1	-1	-3	1	1	2	-3
kg	$0 =$	0	1	1	1	1	0	0	0	1
s	$0 =$	0	-3	1	-2	0	0	-1	-2	0
Re	$0 =$	0	0	-1	0	0	1	1	0	1
Pe	$0 =$	0	1	0	0	0	1	1	1	1
Ec	$0 =$	-1	0	0	0	0	0	2	-1	0
Eu	$0 =$	0	0	0	1	0	0	-2	0	-1
γ	$0 =$	0	0	0	0	-1	0	0	0	1

Table 5: Summary of the dimensionless parameter analysis for the lower plenum flow

Due to the differences in γ between the BenSaid reactor and D&W cases, the pressure loss in a real reactor (based on the calculation of BenSaid) would be 10% higher than previously extrapolated by Damm and Wehrlein. This increase in pressure loss is very relevant to future high temperature reactors since one of the most challenging bottlenecks in design of these reactors is the ΔP budget available for the entire primary circuit.

5.3.3 Mixing efficiency

The results for the mixing coefficient Ψ are as expected for the k-ϵ model, with a near constant Ψ value irrespective of Re. The reader is reminded that the k-ϵ was primarily used for generating the inflow conditions as described in chapter 4.2.3. The RSM plus scalar flux model shows a significantly steeper gradient in the deterioration of Ψ with increasing Re (see figure 5.30) compared to the air test cases as well as experiments. The cause of the steeper gradient is unfortunately not clear. In theory, the gradient for helium should be flatter due to the higher γ value, causing higher turbulent diffusion of enthalpy. An ad hoc estimation of these effects is very difficult, though. The implemented scalar flux equations (3.35) have numerous highly complex permutations of the various scalar fluxes with the individual Reynolds stresses. In strongly swirling flows the Reynolds stresses as well as scalar fluxes can change very suddenly in sign as well as magnitude. This makes an estimation of which terms might be important, and even which sign they might have on average over a large region very difficult, if not impossible. These relationships have been studied in the past for very simplistic canonical flows, but for complex, almost chaotic, flows as observed in the lower plenum, no clear cause of the discrepancy could be found with certainty.

Another hypothetical reason for a flatter gradient can be found in the residence time of the fluid within the lower plenum. For air, the timespan of one flow through is roughly 0.07s, while for helium it is roughly 0.26s. In theory the fluid in the real HTR should then have more time to mix properly before exiting through the exit pipe. Hence, the calculated Ψ values might be assumed to be higher. Despite all of this theorizing, the steeper gradient has to be taken as fact, even if the exact cause cannot be fully identified. At full reactor power the mixing coefficient is 93.9%, meaning that the maximum temperature difference at the outlet would be approximately 12.8 °C according to the design calculations of BenSaid [7]. This value is high when factoring necessary safety margins into the design and may not be acceptable to designers as well as nuclear safety authorities.

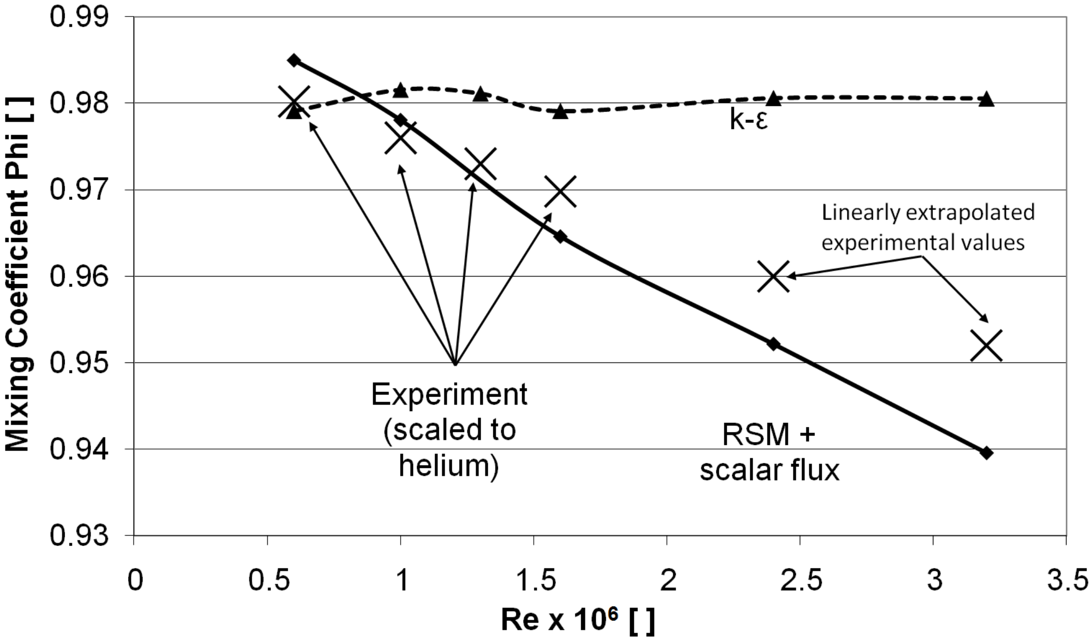

Figure 5.30: Ψ against Re comparison of CFD results against experiment for the BenSaid cases

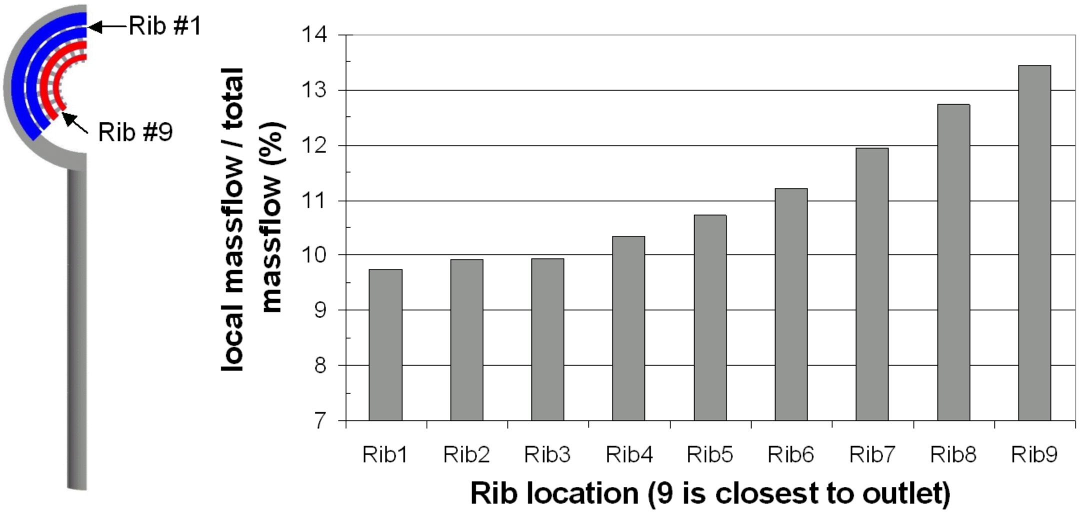

Figure 5.31: Preferential mass flow through the individual "ribs" of the lower plenum. Rib 9 is closest to the outlet.

5.3.4 Mass flow bias

Another newly identified issue is the uneven distribution of mass flow through the different "ribs" in this geometry (see figure 5.31). The "ribs" closest to the outlet have the lowest flow resistance due to their proximity to the exit, and hence the highest mass flow. The lowest value is for the rib opposing the outlet with 9.7% of total mass flow. The rib closest to the outlet contributes with 13.4% to mass flow. Reactor designers have to be acutely aware of this issue, and design the channel system between the reactor core and lower plenum in such a way that no effect to the azimuthal distribution of mass flow can be observed in the reactor cavity above. This can be quite easily achieved by providing wide and high annular channels above the individual round inlet rows of the lower plenum, similar in design to the inlet chambers designed for the CFD geometry in this thesis. The idea is to provide a channel where the flow resistance is significantly lower than the pressure drop caused by the relatively small round inlets into the lower plenum.

5.4 Unsteady effects

5.4.1 Overview

Investigations with full 360 ° geometries, ignoring the 180 ° symmetry plane, showed small deviations along the 180 ° symmetry plane. It was assumed that this in combination with the poor convergence of the RSM turbulence model might point to underlying transient flow phenomena within the lower plenum. In order to investigate this further, a preliminary transient simulation of the lower plenum was started. The flow and geometry is identical to that in the previous chapter, with the only difference being that a full 360 ° geometry of the lower plenum was used. Mass flow was set to an outlet pipe Reynolds number of 3.2^6. Due to computing power limitations, the mesh was made more coarse in the long outlet pipe. An adaptive time step scheme was selected which resulted in time steps of the order of 10^{-4}s to achieve satisfactory Courant numbers. A results file was written every 10^{-2}s. The timescale for a fluid particle to transverse the entire geometry is estimated to be about 0.24s. Hence, the first 0.5s calculated for this case were ignored. After about two months of computational time, the results presented here represent 1.71s of simulation time.

Due to the sparse and and not even continuous sampling rate of the results file, more involved techniques had to be used to make an spectral analysis of the data. A simple Fast-Fourier-Transform is impossible to perform on this data due to the small amount of data points, as well as the irregular sampling period of results file. The technique used in this thesis for the spectral transformation is the so-called Lomb Periodogram; A method originally developed for statistical analysis of the motion of far stars. More detail for this algorithm can be taken from [75]. This algorithm was implemented in Matlab as a C routine. Unlike a Fourier-Transform, this method produces normalized spectra. These spectra have an amplitude relating the likelihood that an observed peak is not due to random white noise. Due to sampling theorems, any spectra above 50Hz have been ignored as well as anything corresponding to a half of the total elapsed time in the simulation.

5.4.2 Transient mass imbalances

One of the most surprising results was the intensity of transient effects throughout the entire geometry. It was for example discovered that the mass flow imbalances through the round inlets into the lower plenum chamber across the symmetry plane were very significant, as one can see in fig 5.32. The transient imbalances between the two sides is the equivalent of up to 10% nominal mass flow. Even more severe fluctuations of the order of 50% compare to steady state values were observed through the individual inlets of the lower plenum. This imbalance can be seen in the outlet pipe severly affecting the flow there and interacting with the large recirculation zone at the start of the outlet pipe.

5.4.3 Transient flow features and details

Using the $\lambda2$ criterion for plotting swirl centers, the transient results show a significantly more detailed flow field than was the case in the steady state simulation. A plot with an isosurface of constant $\lambda2$ for the entire geometry can be seen in figure 5.33. In this figure, one can see the main swirling motion up the annular collection chamber in the upper half of the lower plenum chamber. This is the main swirling motion which is fed by individual jets from the lower plenum inlets.

One can see these individual feeding jets wrapping around this main swirling motion and then merging with it. In the background one can see the rather

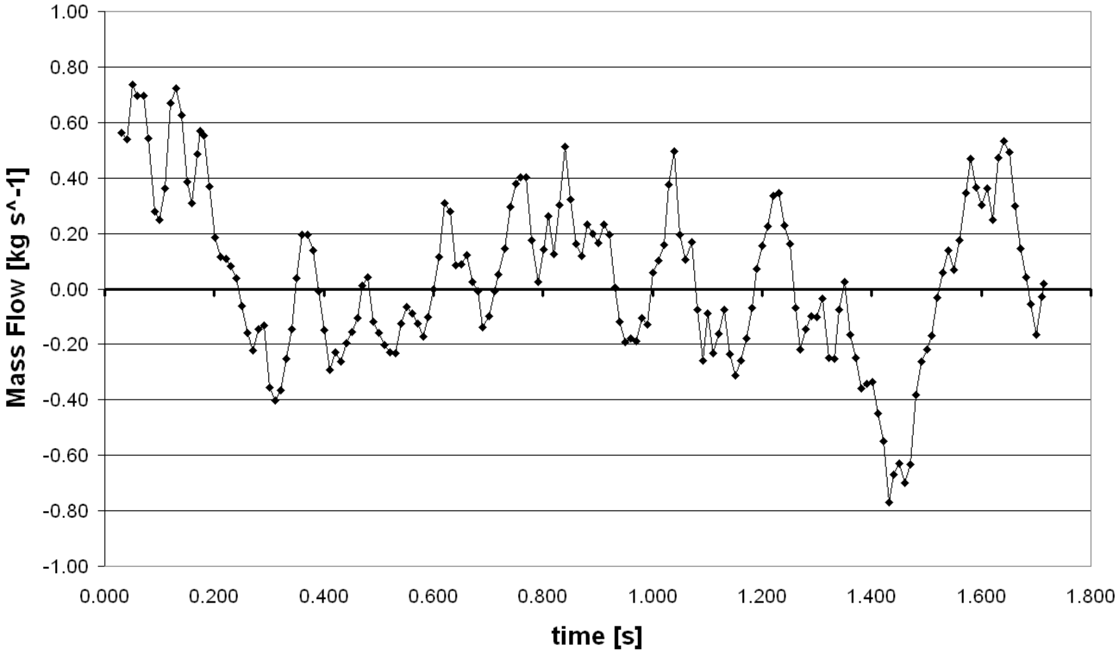

Figure 5.32: Transient mass flow imbalance across the symmetry plane between the inlets of the lower plenum chamber over time.

chaotic system of small eddies within the ribs and small recirculation zones due to detaching flow as it passes sharp corners within the lower plenum. The reader should also draw his attention to the very large recirculation zone found at the start of the outlet pipe. Interestingly, some small individual jets which can be seen warping themselves around the main swirling motion, detach from the main fluid motion and continue through the recirculation zone. The recirculation zone at the start of the outlet pipe is further shown in figures 5.34 and 5.35.

The next set of figures (5.36, 5.37, 5.38) are vector plots right at the start of the outlet pipe made at different times. Here one can see a large amount of variability in the recirculation zone over time. The small eddies within the blue area of the recirculation zone are the earlier mentioned inlet jets which detached themselves from the main swirling motion. The mass imbalances across the symmetry plane can be clearly seen by the momentum bias towards one side. The numbers in figure 5.36 denote the location of data points for analysis in sub-chapter 5.4.6.

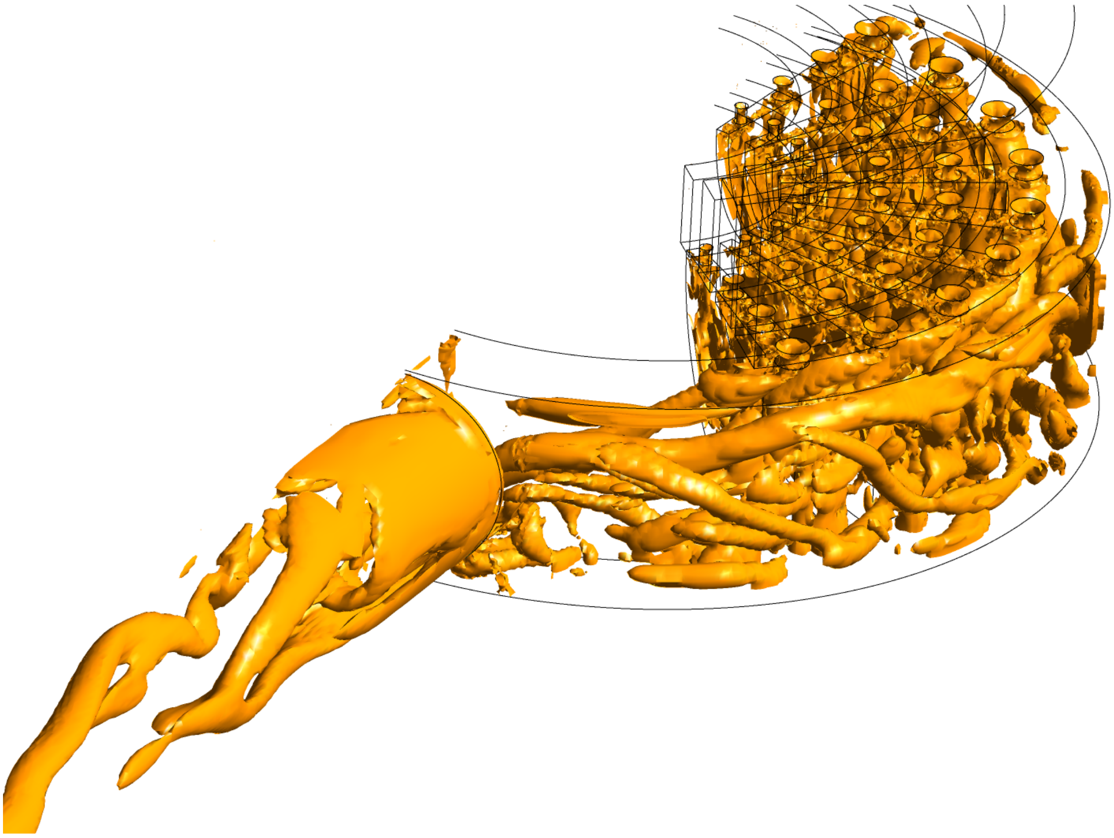

Figure 5.33: Plot of constant $\lambda 2$ iso-surfaces over the entire lower plenum geometry.

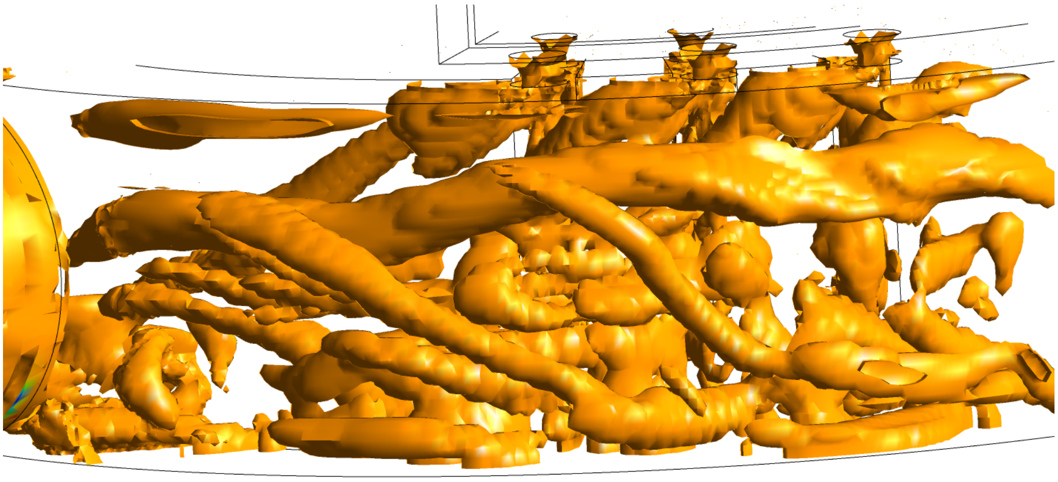

Figure 5.34: Plot of constant $\lambda 2$ iso-surfaces showing the strong vortex of the annular collection chamber with recirculation zones after each individual “rib”.

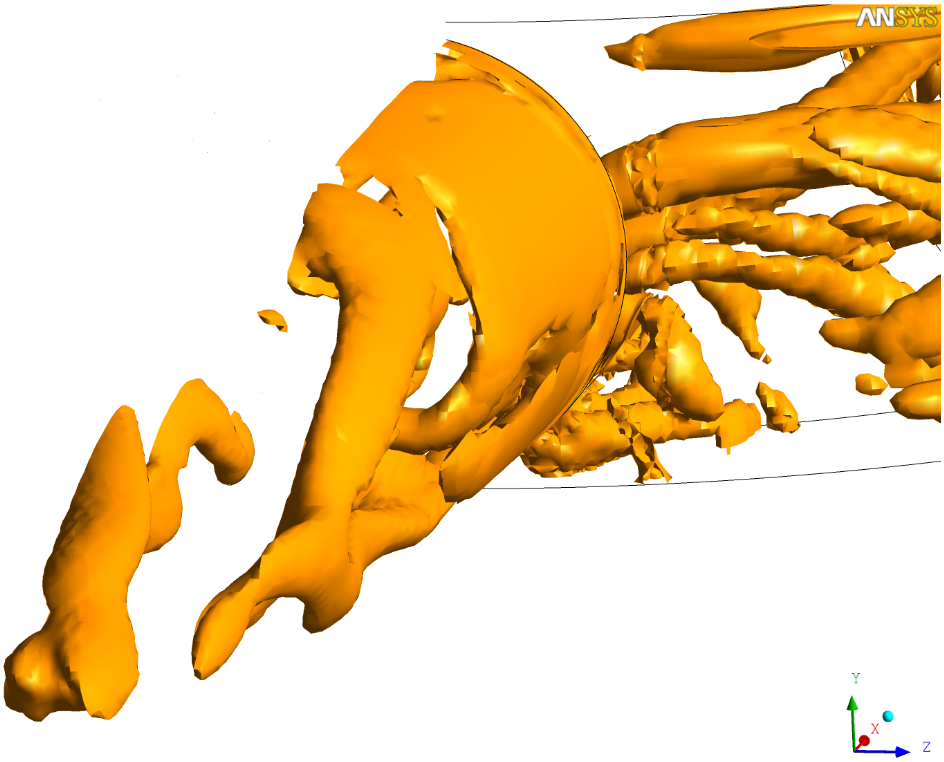

Figure 5.35: Plot of constant $\lambda 2$ iso-surfaces specifically of the recirculation zone at the start of the outlet pipe.

5.4.4 Pressure loss and fluctuations

The pressure loss coefficient is observed to fluctuate by about 10% around a mean which is nearly identical to the steady state results presented earlier. In figure 5.39 one can see how the pressure loss coeffcient ξ fluctuated about the steady state mean displayed as a thick horizonal line. Of more interest is perhaps the spectral analysis of this signal in figure 5.40. The dashed horizontal lines show the probability of an individual data point being caused by random white noise. It can thought of as a significance margin. In this spectral plot one can see a wide peak just below the 50% significance margin at frequencies between 39 and 45Hz. Due to the significance only being applied on a per data point basis, 20 data points of 50% significance means that 10 points are probably due to white noise, while the other 10 points are genuine frequency peaks. These pressure fluctuations have a strength of about 0.02bar, and it is not known to the author whether fluctuations of this intensity in the area of 40-45Hz might be problematic to components further down stream of the reactor.

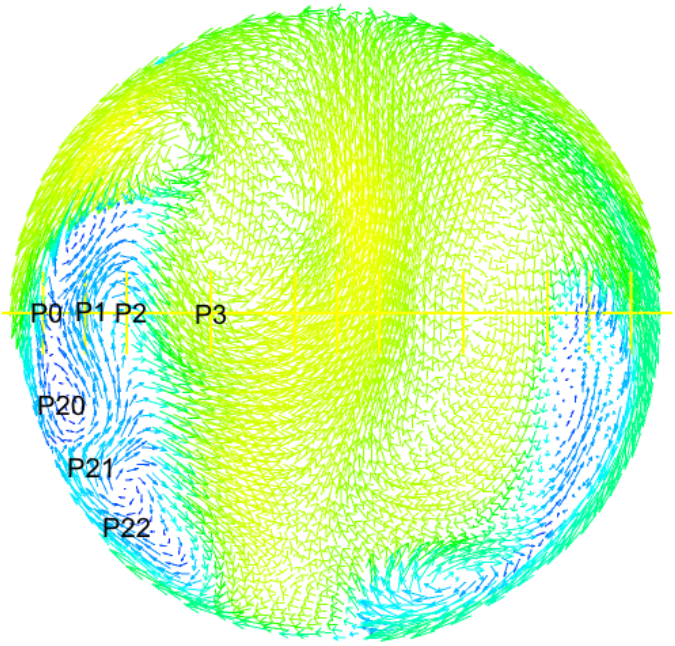

Figure 5.36: Vector plot across the start of the outlet pipe at a certain time (a).

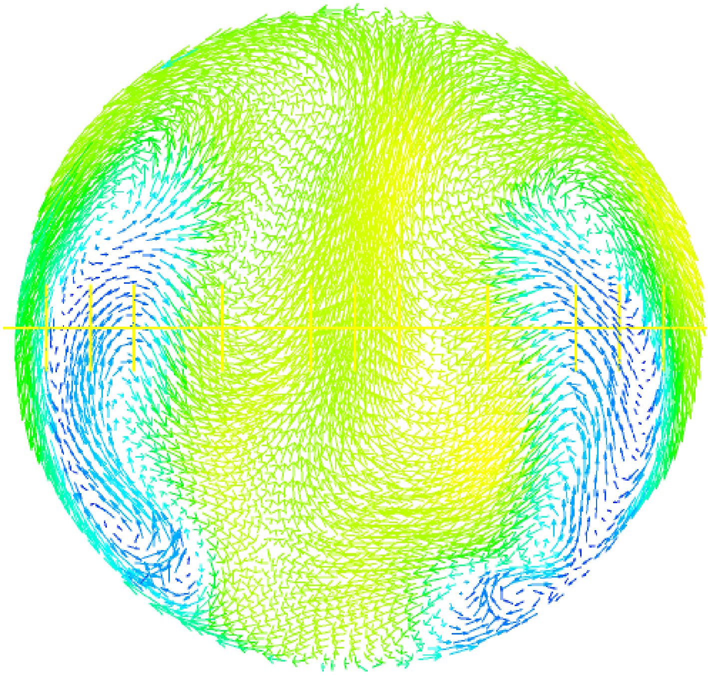

Figure 5.37: Vector plot across the start of the outlet pipe at a certain time (b).

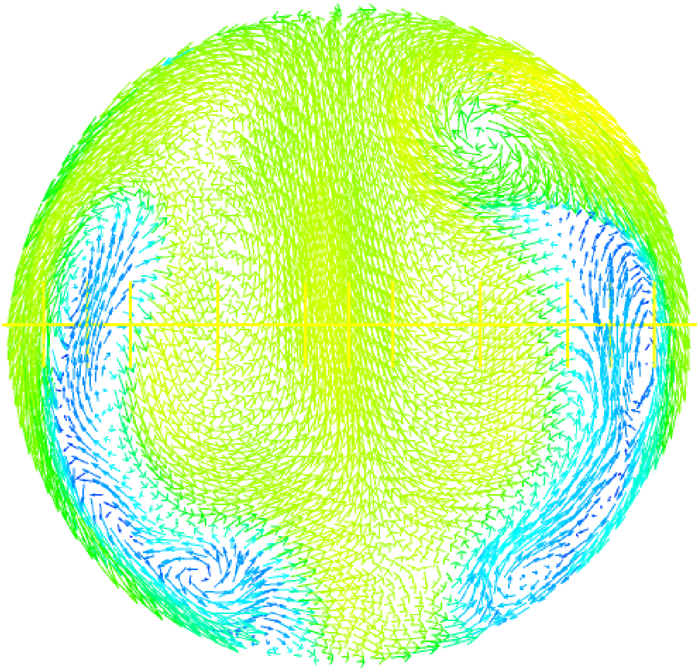

Figure 5.38: Vector plot across the start of the outlet pipe at a certain time (c).

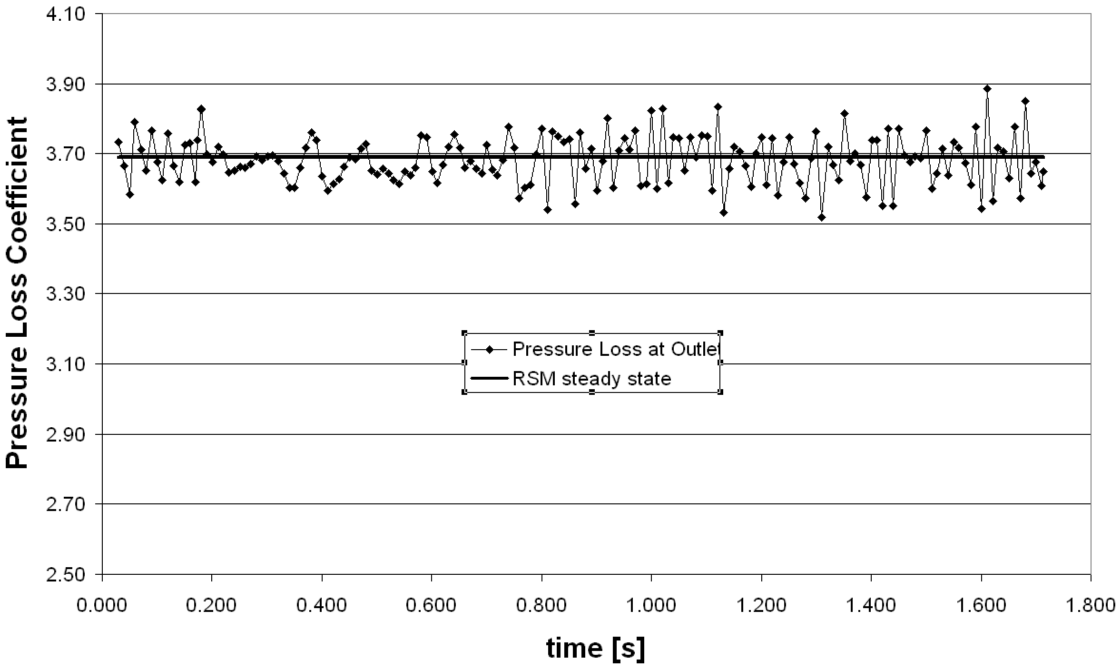

Figure 5.39: Pressure loss coefficient ξ fluctuations against time. The thick line shows the steady state value of ξ.

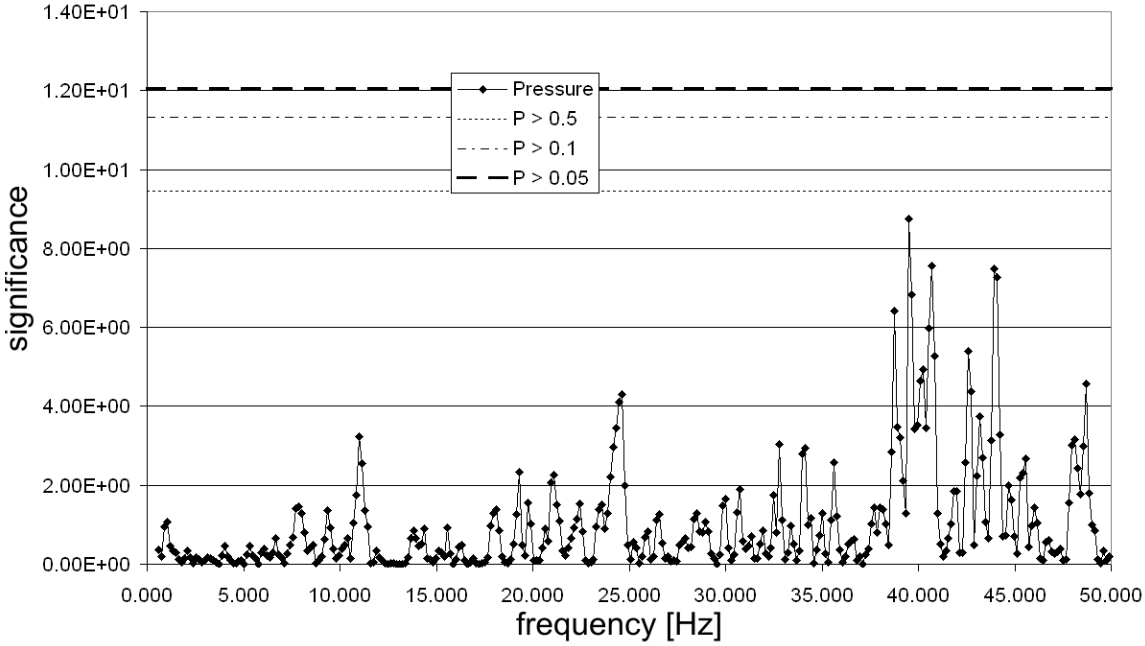

Figure 5.40: Spectral plot of significant fluctuating frequencies for the pressure loss coefficient ξ.

5.4.5 Mixing efficiency

Due to the the rather coarse mesh in the outlet pipe, mixing efficiencies Ψ will only be discussed up the start of the outlet pipe. The value of Ψ is highly sensitive to numerical diffusion, since it only accounts for the maximum temperature values, which can be easily reduced by a small amount due to numerical diffusion. The coarser mesh in the outlet pipe is already sufficient to significantly effect the mixing efficiency Ψ. It would be advisable to use some sort of statistical averaging procedure such as variance other the rather primitive min-max definition of Ψ.

In figure 5.41 the value of Ψ is systematically above its steady state value shown by the thick horizontal line. The spectra of ϕ is interesting as it shows the possibility of peaks in the region of 5, 7 and 17Hz. Unfortunately the signal is too weak and a longer simulation time with more data files would be necessary to see whether these peaks are only statistical flukes.

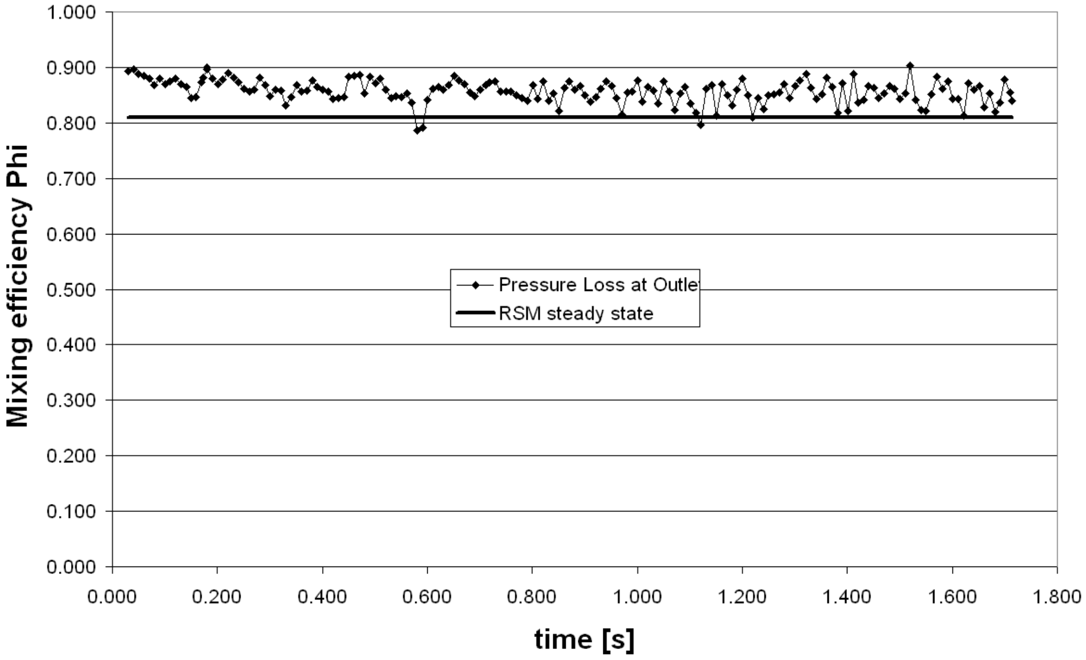

Figure 5.41: Transient fluctuations of Ψ against time.

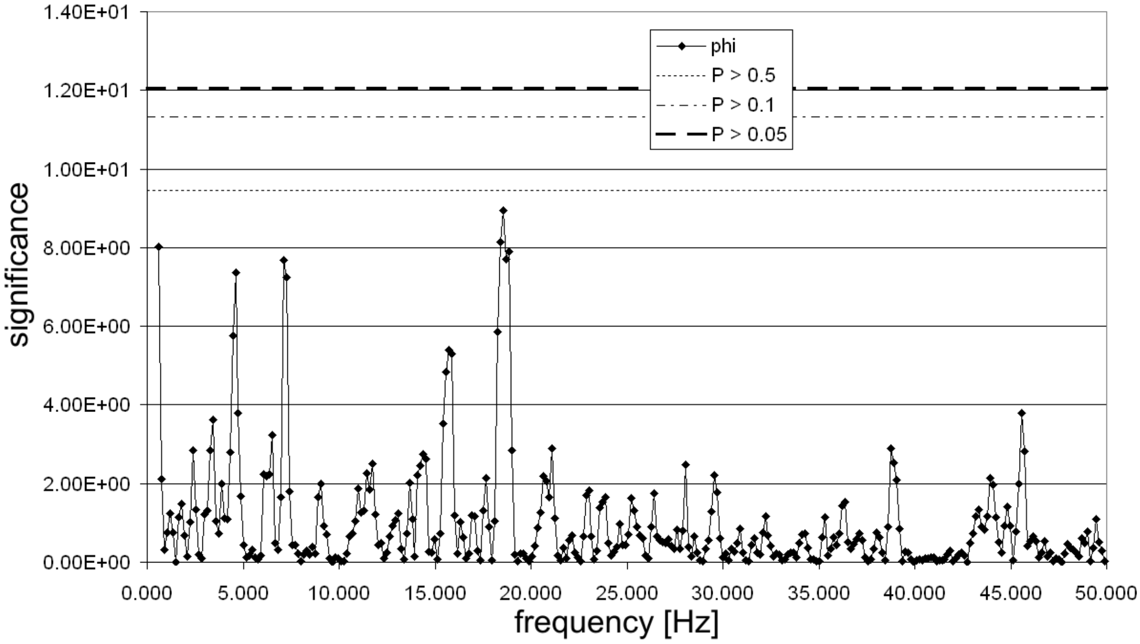

Figure 5.42: Spectral analysis of Ψ at the start of the outlet pipe.

5.4.6 Investigation on the recirculation zone of the outlet pipe

In this section the structure of the recirculation zone in the outlet pipe will be investigated in more detail. This zone may by important to future designers as the materials used for the outlet pipe are operating very close to their limits and can be hence easily damaged. Three data points, points 20 to 22 have been selected for this task. Their location can be seen in figure 5.36.

The temperature data (fig. 5.43 shows a strong correlation between the three data points for temperature with a computed autocorrelation function very close to 1. The amplitude of oscillations is around 10 °C with some rare extremes above 15 °C. The spectral data (fig. 5.44) shows a very significant and wide peak between 2.5 and 5Hz. It is interesting to note that while the three points are strongly correlated in temperature, their correlation is significantly weaker for axial velocity u (fig. 5.45). It can be also seen that the spectral peaks for axial velocity are very different to those of temperature. While nothing especially noteworthy, this is a nice direct example of why turbulence modeling of passive scalars and momentum should not be linked directly via linear eddy viscosity concepts. Further, the separation in spectra also shows a need that for passive scalar as well as momentum turbulence quantities to actually have their own individual equations for turbulence time or length scales.

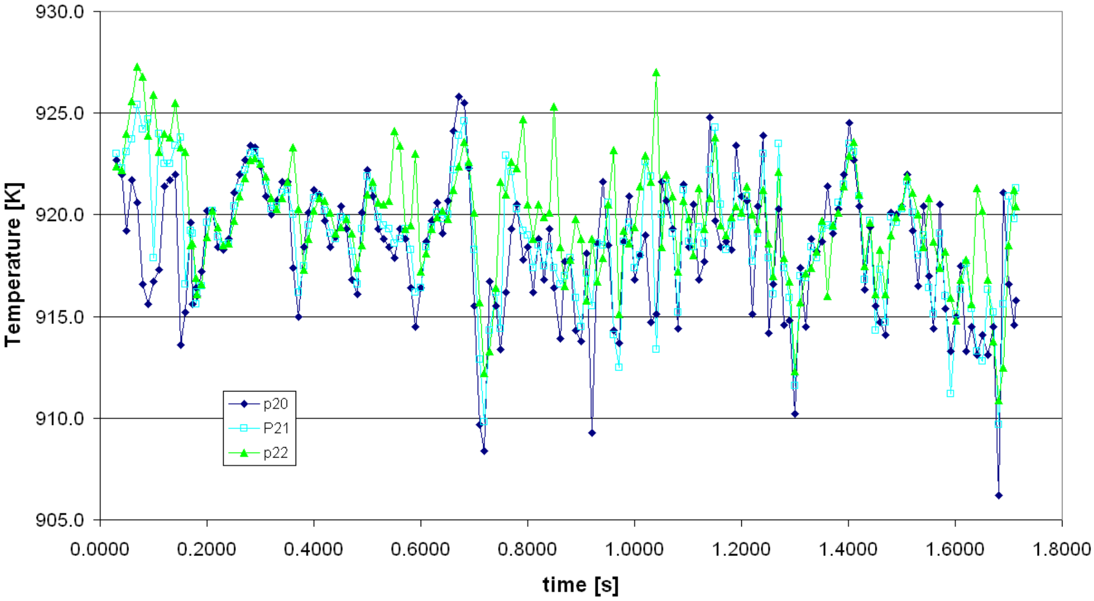

Figure 5.43: Transient temperature data in points 20 to 22 against time.

5.4.7 Temperature fluctuations in the outlet pipe

The next set of data points are the points labeled P0 to P2 in figure 5.36. They were chosen because of the extraordinary low frequency peak in the region of slightly below one Herz. This frequency would be certainly low enough for some cyclic heat transfer to occur with the pipe walls in a real reactor, causing rapid cyclic aging of the pipe wall materials.

Due to the rather ad hoc nature of this transient simulation, one should not yet put too much weight into these results, though. This transient simulation has been mostly performed to identify topics and areas of interest fur future investigations. Several issues, such as the possibility of low frequency temperature transients close to the wall or low frequency pressure oscillations, have been identified which may need further investigation.

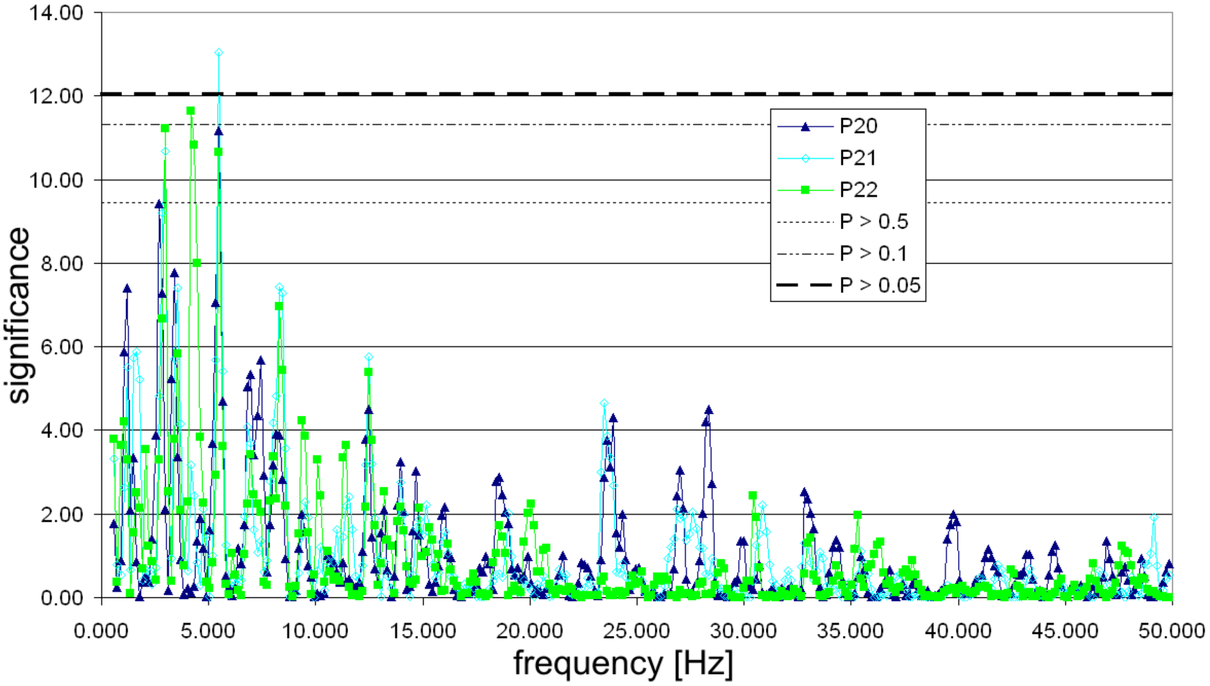

Figure 5.44: Spectral analysis of the temperature data in points 20 to 22.

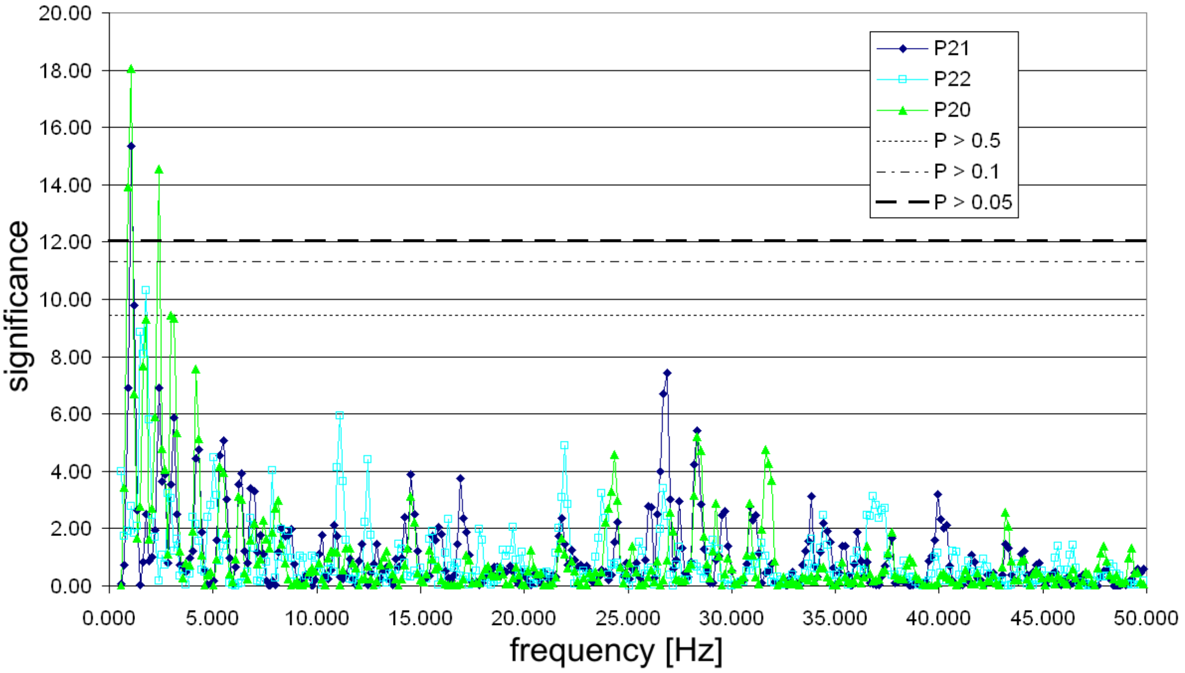

Figure 5.45: Spectral analysis of axial velocity data in points 20 to 22.

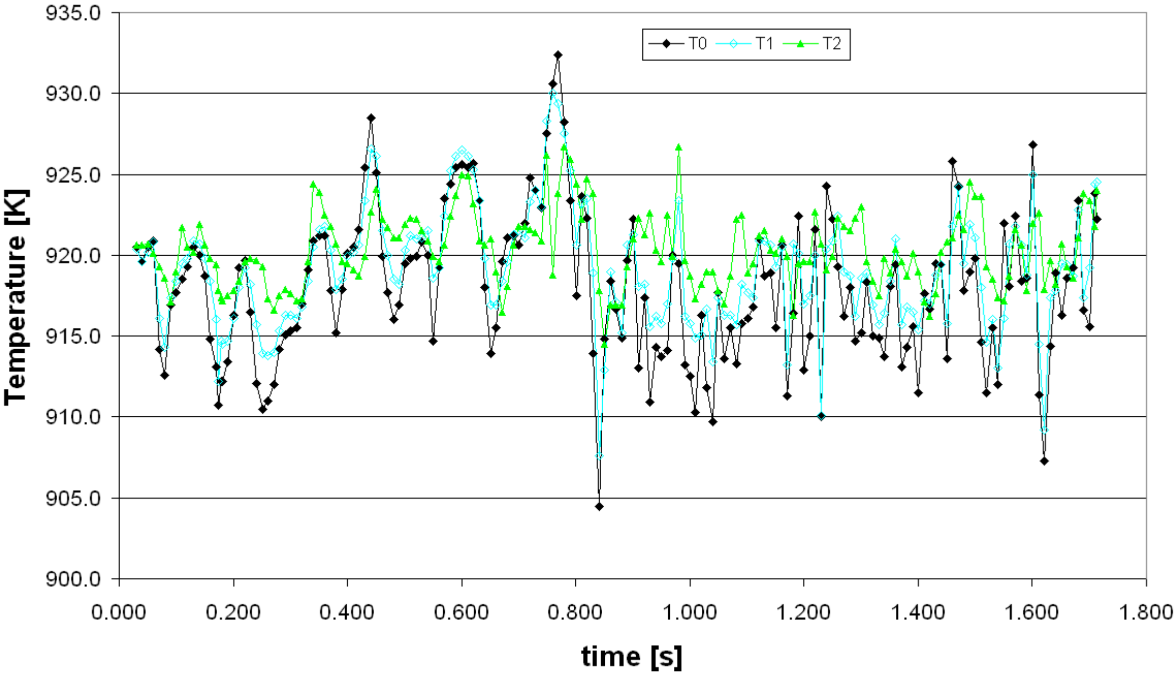

Figure 5.46: Preferential mass flow through the individual “ribs” of the lower plenum. Rib 9 is closest to the outlet.

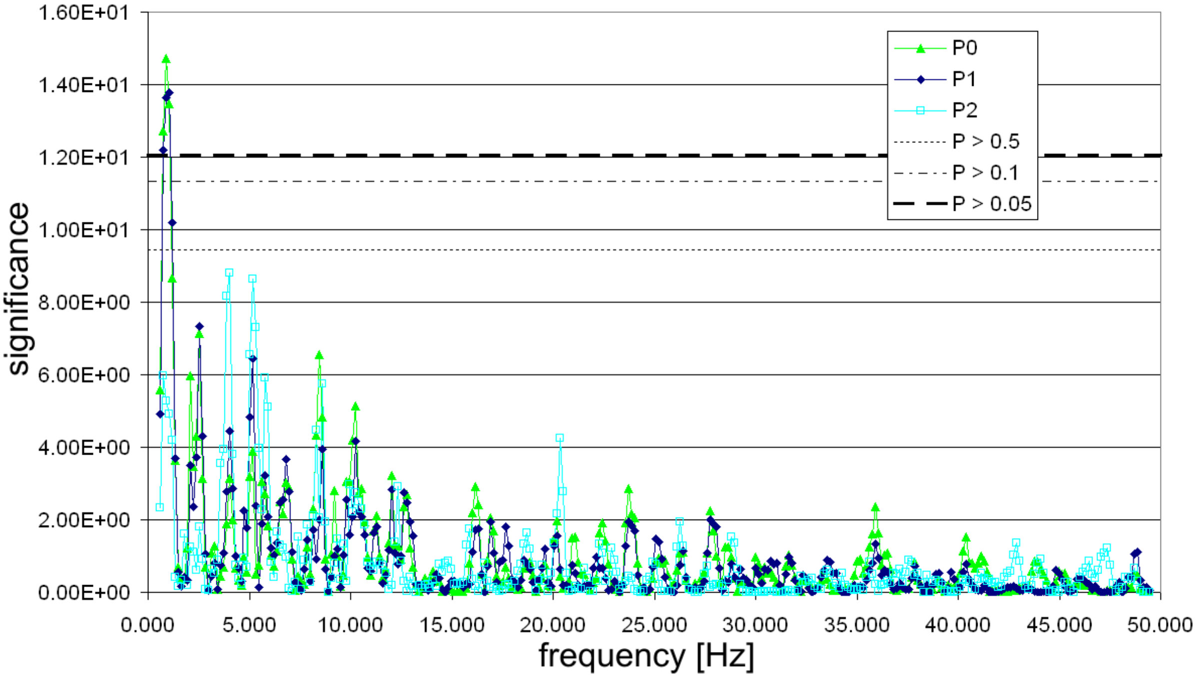

Figure 5.47: Preferential mass flow through the individual “ribs” of the lower plenum. Rib 9 is closest to the outlet.

Chapter 6

Conclusion

The lower plenum of a pebble-bed high-temperature reactor (HTR) is used to mix temperature variations of the helium coolant as it exits the nuclear core. Due to an uneven power distribution in radial direction, with the location of maximum power in the center, as well as very poor mixing within the core in radial direction, these temperature differences can be as high as 210 °C. Experiments have been performed previously on scaled air test rigs, with those done by Damm and Wehrlein [5] standing out in particular. One particular issue of these experiments, though, is the uncertain scalability of their results to future reactors, as well as a lack of detailed knowledge of the flow within the lower plenum. It is hence the aim of the work presented here to develop a scalable CFD model for investigating the flow, as well as mixing behavior of the lower plenum of HTRs.

The flow of the lower plenum of an HTR is characterised by very strong swirl, with the Swirl number at $\sim$1 in the annular collection chamber as well as outlet pipe. The hot and cold gases from the core enter the lower plenum via radially inwards pointing “rib”-like structures, where very complex eddy flows achieve significant mixing. The flow exiting these “rib” interacts itself with the strong vortex in the annular collection chamber, enhancing mixing. As the flow is moving downstream through the annular collection chamber past these ribs, flow entering the collection chamber through these ribs is excitating the main swirl vortex in the collection chamber, as well as causing an acceleration of the entire flow. This highly turbulent and swirling flow is challenging to model accurately in CFD, and great care has to be taken in selecting and implementing proper turbulence models.

Due to the difficulty of simulating the turbulent and strongly swirling flow in the lower plenum, a new model for the turbulent transport of passive scalars developed and implemented in ANSYS CFD. This model is based on the second order modeling of the turbulent scalar fluxes and it proved its capabilities in the very challenging swirl flow validation test cases by So et al. [55; 64; 65; 66]. With this validated model, simulations on the experiments by Damm and Wehrlein were in very good agreement and demonstrated that the lower plenum flow can be accurately modeled in CFD.

The simulations on the experiments by Damm and Wehrlein showed that linear-eddy viscosity turbulence models, such as the k-ϵ model, are generally unsuited for this problem. They are capable of predicting the correct loss of pressure, but any further results or utility of these models for the lower plenum flow have to be viewed very sceptically. The RSM is able to reproduce the observed flow of the experiments significantly better, but due to the simplistic linear eddy diffusivity model, there is a significant error in the results for mixing efficiency. Only in combination with the above mentioned scalar flux model could a very good agreement with experiments be achieved. Of great importance was the demonstration of correct scaling of the results with varying Reynolds number, prerequisite for investigating different lower plenums with confidence.

With the demonstration of scalability of the CFD models, a simulation of more realistic flow configurations based on the HTR-Modul could be conducted successfully. he discrepancy of the non-dimensional pressure loss coefficient ξ between air test cases and HTR test cases using helium. It could be shown that the method of extrapolating the experimental air values to helium flows in a real reactor were not accurate, and that these extrapolations under predicted the pressure loss for the HTR-Modul by nearly 10%. The source for this error is thought to be two-fold. Firstly, in turbulent flows with strong density gradients the ratio of density differences γ is of great importance for achieving similarity of flow. Secondly, it can be shown via dimensionless number analysis that for the case of weakly compressible flows with a coupled energy equation, the dimensionless Eckart number plays an important role, too. Future experimentators wishing to investigate the lower plenum flow will have to be accutely aware of this issue and design their experiments accordingly to achieve flow similarity.

The HTR-Modul simulations also showed that the extrapolation by Damm and Wehrlein for mixing efficiencies may not have been sufficiently conservative. The CFD results indicated that mixing efficiencies Ψ may be worse than expected with a value of $\Psi = 93.9\%$. For the HTR-Modul this would translate to a maximum temperature difference of 12.8 °C which is borderline value for licensing purposes. In the future with bigger reactor designs this issue may become more important since these reactors will be almost certainly operated under higher Reynolds numbers with a higher ΔT at bottom of the core. This would result in lower mixing efficiencies and hence higher ΔT at the heat exchanger, turbine interfaces.

A further issue discovered with the HTR-Modul simulation is the problem of unequal mass flow through the various "ribs" of the lower plenum. Due to flow always finding the way of least resistance, the ribs closest to the outlet pipe will recieve significantly more mass flow than those in different positions. Unless mitigated, this bias would have severe consequences in an HTR introducing azimuthal temperature as well as mass flow variations. This would result in significantly higher temperature variations within the reactor core leading to an overall lower power output due to safety concerns. Fortunately, this issue can be fairly easily mitigated, by introducing channels similar to those used in the CFD calculations for generating the correct inflow conditions.

Simulations on geometries which did not make use of the 180 °C symmetry plane indicated that there might be weak transient flow features found in the lower plenum flow. In order to investigate this further, a transient simulation on the HTR-Modul geometry was started. Preliminary results showed very strong transient flow behavior to occur within this geometry. There is a very high likelihood that transient pressure waves with an amplitude of about 0.02bar and a frequency of 40-45Hz will occur within the outlet pipe. A strong decoupling in timescales of velocity, pressure and temperature fluctuations was observed. There is a likelihood for fluctuations in in the mixing efficiency Ψ to occur at around 17Hz in the outlet pipe and any subsequent components. More importantly, though, there are several regions close to the large recirculation zone at the start of the outlet pipe were temperature fluctuations in the near wall region have a frequency in the region of 1-2 Hz and an amplitude of 15-20 °C. This needs further investigation in the future as these fluctuations may cause rapid aging of the steel outlet pipe, or other steel components of the hot gas duct.

In summary, a capable tool for investigating the lower plenum flow as been developed and successfully used. The results discussed here, were additionally presented at several conferences [76; 77; 78] in front of experts in the field of computational fluid mechanics and turbulence modeling, and were received with great interest. The scalability of this tool has been demonstrated and it can be used for investigating refinements in the lower plenum geometry or used for design of the lower plenum in new reactors in the future.

References

[1] British Petroleum p.l.c. (BP), *Statistical Review of World Energy 2007*. http://www.bp.com/, 2007. 1

[2] International Energy Annual 2005, *World Carbon Dioxide Emissions from the Use of Fossil Fuels*. Energy Information Administration, US Department of Energy, 2007. 1

[3] IAEA - TECDOC - 978, *Fuel performance and fission product behavior in gas cooled reactors*. International Atomic Energy Agency (IAEA), 1997. 2, 3

[4] IAEA - TECDOC - 784, *Response of fuel, fuel elements and gas cooled reactor cores under accidental air or water ingress conditions*. International Atomic Energy Agency (IAEA), 1993. 2, 3

[5] G. Damm and R. Wehrlein, "Simulation tests for temperature mixing in a core bottom model of the HTR-Module," *Nuclear Engineering and Design*, pp. 97–105, 1992. 4, 7, 15, 66, 101

[6] N. B. Said, G. Lohnert, and M. B. W. Bernnat, "The impact of design on the decay heat removal capabilities of a modular pebble bed HTR," *Nuclear Engineering and Design*, no. 5-6, pp. 648–656, 2006. 4

[7] N. B. Said, *Thermohydraulische Analysen für das Betriebs- und Nachwärmeabfuhrverhalten modularer Hochtemperaturreaktoren mit verschiedenen Kernkonfigurationen*. PhD thesis, University of Stuttgart, 2007. 4, 14, 48, 86

[8] M. Yao, Z. Huang, C. Ma, and Y. Xu, "Simulating test for thermal mixing in the hot gas chamber of the HTR-10," *Nuclear Engineering and Design*, pp. 233–240, 2002. 9, 10, 11

[9] M. Hishida, N. Akino, M. Ogawa, T. Kunugi, H. Kawamura, K. Sanokawa, and Y. Okamoto, "Heat transfer problems in a VHTR," *Heat Transfer in High Technology and Power Engineering, Proceedings*, no. Hemisphere Publ. Co., pp. 273–284, 1987. 9

[10] Y. Inagaki, R. Hino, K. Kunitomi, K. Takase, I. Ioka, and S. Maruyama, "R&D on thermal hydraulics of core and core-bottom structure," *Nuclear Engineering and Design*, no. 1-3, pp. 273–284, 1987. 9

[11] N. Tauveron, "Thermal fluctuations in the lower plenum of an high temperature reactor," *Nuclear Engineering and Design*, no. 2-3, pp. 125–137, 2003. 9

[12] N. Anderson, Y. Hassan, and R. Schultz, "Analysis of the hot gas flow in the outlet plenum of the very high temperature reactor using coupled RELAP5 - 3D system code and a CFD code," *Nuclear Engineering and Design*, p. 274279, 2008. 9, 10

[13] J. Wang, Z. Huang, H. Bo, and S. Jiang, "Flow field analysis of the hot gas chamber of the 10MW high temperature reactor," *2nd International topical meeting on high temperature reactor technology, Beijing, China*, 2004. 10, 11, 23

[14] J. Wang, H. Bo, S. Jiang, Y. Xu, and W. Zheng, "Optimization of hot gas chamber in high temperature reactor," *Jounal of Nuclear Science and Technology*, no. 11, pp. 1–7, 2004. 10, 11, 23

[15] N. B. Said, G. Lohnert, M. Buck, and W. Bernnat, "The impact of design on the decay heat removal capabilities of a modular pebble bed HTR," *Nuclear Engineering and Design*, no. 5-6, pp. 648–656, 2006. 14

[16] Hermann Schlichting, *Grenzschicht-Theorie.* Verlag G.Braun, Karlsruhe, 1982. 17, 24

[17] ANSYS Ltd., *ANSYS CFX-Solver Theory Guide.* ANSYS CFX Release 11.0, 2006. 19

[18] Wilcox, *Turbulence Modeling for CFD.* DCW Industries, 1998. 24, 30

[19] A. Favre, "Equations des gez turbulents compressibles," *J. de Mchanique*, pp. 361–421, 1965. 25

[20] P. Chassaing, "The modeling of variable density turbulent flows: A review of first-order closure schemes," *Flow, Turbulence and Combustion*, pp. 293–332, 2001. 25

[21] H. HaMinh and B. E. Launder and J. MacInnes, *The turbulence modeling of variable density flows - A mixed-weighted decomposition. In: Bradbury, L.S.J., Durst, F., Launder, B. E., Schmidt, F. W., Whitelaw, J. H., (eds).* University of California, Davis. Springer-Verlag, Berlin, 1981. 25

[22] W. P. Jones and B. E. Launder, "The prediction of laminarization with a two-equation model of turbulence," *Int. J. Heat and Mass Transfer*, pp. 301–314, 1972. 28

[23] D. C. Wilcox, “Multiscale model for turbulent flows,” *In AIAA 24th Aerospace Sciences Meeting*, 1986. 28

[24] B. E. Launder, “Heat and mass transport, in: Bradshaw (ed.),” *Turbulence, Topics in Applied Physics*, pp. 232–287, 1976. 29

[25] R. Jester-Zürker, S. Jakirlic, and C. Tropea, “Computational modelling of turbulent mixing in confined swirling environment under constant and variable density conditions,” *Flow, Turbulence and Combustion*, pp. 217–244, 2005. 29, 35, 37, 60

[26] S. Jakirlic, K. Hanjalic, and C. Tropea, “Modeling rotating and swirling turbulent flows: A perpetual challenge,” *AIAA Journal*, no. 10, pp. 1984–1996, 2002. 29, 35, 55, 59

[27] W. P. Jones and D. Lentini, “A realisable non-linear eddy viscosity model for confined swirling flows,” *Int. Journal of Heat and Fluid Flow*, no. 6, pp. 1612–1627, 2008. 29, 33, 35, 37, 60

[28] T. J. Craft, B. E. Launder, and K. Suga, “Development and application of a cubic eddy-viscosity model of turbulence,” *J. Heat and Fluid Flow*, pp. 108–115, 1996. 29

[29] S. Wallin and A. V. Johansson, “An explicit algebraic Reynolds stress model for incompressible and compressible turbulent flow,” *J. Fluid Mech*, pp. 89–132, 2000. 29

[30] A. Abdon and B. Sunden, “Numerical investigation of impingement heat transfer using linear and non-linear turbulence models,” *Numerics of Heat Transfer*, pp. 563–578, 2001. 29

[31] B. Weigand, T. Schwartzkopf, and T. P. Sommer, “A numerical investigation in a parallel plate channel with piecewise constant wall temperature boundary conditions,” *Journal of Heat Transfer*, pp. 626–634, 2002. 29

[32] Wolfgang Rodi, *Turbulence models and their application in hydraulics: a state-of-the-art review.* Balkema, Rotterdam, 1993. 30

[33] T. Gatski and C. Speziale, “On explicit algebraic stress models for complex turbulent flows,” *J. Fluid Mechanics*, vol. 254, pp. 59–78, 1993. 30

[34] J. Weis and K. Hutter, “On euclidean invariance of algebraic Reynolds stress models in turbulence,” *J. Fluid Mechanics*, vol. 476, pp. 63–68, 2003. 30

[35] B. Launder, G. Reece, and W. Rodi, “Progress in the development of a reynolds-stress turbulence closure,” *J. Fluid Mechanics*, no. 3, pp. 537–566, 1975. 31

[36] M. Gibson and B. Launder, "Ground effects on pressure fluctuations in the atmospheric boundary layer," *J. Fluid Mechanics*, no. 3, pp. 491–511, 1978. 31

[37] C. Speziale, "Modeling the pressure-gradient-velocity correlation of turbulence," *Pysics of Fluids*, pp. 69–71, 1985. 31

[38] C. Speziale, "Analytical methods for the development of reynolds stress closures in turbulence," *Annual Review of Fluid Mechanics*, pp. 107–157, 1991. 31

[39] J. Lumley, "Compuational modeling of turbulent flows," *Advances in Applied Mathematics*, pp. 123–176, 1978. 31

[40] C. Speziale, "Second-order closure models for rotating turbulent flows," *Q. Applied Mathematics*, pp. 721–733, 1987. 31

[41] C. Speziale, S. Sarkar, and T. Gatski, "Modeling the pressure-strain correlation of turbulence," *Journal of Fluid Mechanics*, pp. 245–272, 1991. 31, 35

[42] W. Jones and A. Pascau, "Calculation of confined swirling flows with a second moment closure," *J. of Fluids Engineering*, pp. 248–255, 1989. 31

[43] M. Gibson and B. Younis, "Calculation of swirling jets with a reynolds stress closure," *Physics of Fluids*, no. 1, pp. 38–48, 1986. 31

[44] S. Hogg and M. Leschziner, "Computation of highly swirling confined flow with a reynolds stress turbulence model," *AIAA Journal*, no. 1, pp. 57–63, 1989. 32, 34

[45] S. Hirai and T. Takagi, "Numerical prediction of turbulent mixing in a variable-density swirling pipe flow," *Int. J. Heat and Mass Transfer*, no. 12, pp. 3141–3150, 1991. 32, 34, 37, 60

[46] M. Hallbäck, J. Groth, and A. V. Johansson, "An algebraic model for nonisotropic turbulent dissipation rate in reynolds stress closures," *Physics of Fluids A*, no. 2, pp. 1859–1866, 1990. 32, 35

[47] K. Hanjalic and S. Jakirlic, "Contribution towards the second-moment closure modelling of separating turbulent flows," *Computers & Fluids*, no. 2, pp. 137–156, 1998. 32, 35

[48] S. Hirai and T. Takagi, "Parameters dominating swirl effects on turbulent transport derived from stress-scalar-flux transport equation," *Int. J. Heat and Mass Transfer*, no. 12, pp. 2175–2182, 1995. 33

[49] M. Freitag, M. Klein, M. Gregor, D. Geyer, C. Schneider, A. Dreizler, and J. Janicka, “Mixing analysis of a swirling recirculating flow using DNS and experimental data,” *Int. J. Heat and Fluid Flow*, no. 4, pp. 636–643, 2006. 33

[50] M. Freitag and M. Klein, “Direct numerical simulation of a recirculating, swirling flow,” *Flow, Turbulence and Combustion*, pp. 51–66, 2005. 33

[51] L. N. Carteciano and G. Grötzbach, *Validation of turbulence models in the computer code FLUTAN for a free hot sodium jet in different buoyancy flow regimes.* Forschungszentrum Karlsruhe, 2003. 33

[52] D. Vandromme, *Turbulence modelling in variable density flow.* PhD thesis, University of Brussels, 1980. 33

[53] B. E. Launder and D. S. A. Samaraweera, “Application of a second-moment turbulence closure to heat and mass transport in thin shear flows - i. two-dimensional transport,” *Int. Journal of Heat and Mass Transfer*, pp. 1631–1643, 1979. 34, 37

[54] W. P. Jones and P. Musonge, “Closure of the reynolds stress and scalar flux equations,” *Physics of Fluids*, pp. 3589–3604, 1988. 34

[55] R. So, S. Ahmed, and H. Mongia, “Jet characteristics in confined swirling flow,” *Experiments in Fluids*, pp. 221–230, 1985. 34, 38, 44, 59, 102

[56] M. Ohtsuka, “Numerical analysis of swirling non-reacting and reacting flows by the reynolds stress differential method,” *Int. Journal of Heat and Mass Transfer*, no. 2, pp. 331–337, 1995. 34, 37, 60

[57] H. Kawamura and Y. Kurihara, “Modelling of turbulent scalar transport in homogeneous turbulence,” *Int. J. Heat Mass Transfer*, p. 19351945, 2000. 34

[58] J. G. Brasseur and M. J. Lee, *Advances in turbulence 2.* edited by Fernholz and H.E. Fiedler (Springer, Berlin, 1989. 34

[59] S. Pope, “Consistent modelling of scalars in turbulent flows,” *Physics of Fluids*, pp. 404–408, 1983. 34

[60] C. J. Chen and W. Rodi, *Vertical turbulent buoyant jets, a review of experimental data.* Pergamon Press, Oxford, 1980. 36

[61] C. Chen, J. J. Riley, and P. A. McMurthy, “A study of favre averaging in turbulent flows with chemical reaction,” *Combustion and Flame*, pp. 257–277, 1991. 36

[62] S. Hogg and M. Leschziner, “Second-moment-closure calculation of strongly swirling confined flow with large density gradients,” *Int. J. of Heat and Fluid Flow*, no. 1, pp. 16–27, 1989. 37, 44, 45, 60

[63] W. Steenbergen, *Turbulent Pipe Flow with Swirl.* PhD thesis, Eindhoven University, 1995. 38, 42, 55, 56

[64] R. So, S. Ahmed, and M. Yu, "The near field behavior of turbulent gas jets in a long confinement," *Experiments in Fluids*, pp. 2–10, 1987. 38, 44, 59, 102

[65] S. Ahmed, R. So, and H. Mongia, "Density effects on jet characteristics in confined swirling flow," *Experiments in Fluids*, pp. 231–238, 1985. 38, 44, 59, 102

[66] S. Ahmed and R. So, "Concentration distributions in a model combustor," *Experiments in Fluids*, pp. 107–113, 1986. 38, 44, 59, 102

[67] C. L. Rumsey, B. vanLeer, and P. L. Roe, "A multidimensional flux function with applications to the Euler-Navier-Stokes," 41

[68] R. Harth and K. Hammeke, *Thermodynamische Stoffwerte von Helium im Bereich von 0 bis 3000C und 0.2 bis 200 bar, Jül - 666 - RB.* Kernforschungsanlage Jülich, 1970. 50

[69] Y. G. Lai, "Predictive capabilities of turbulence models for a confined swirling flow," *AIAA Journal*, vol. 34, no. 8, pp. 1743–1745, 1996. 55

[70] R. Roback and B. V. Johnson, *Mass and Momentum Turbulent Transport Experiments with Confined Swirling Air Flow.* NASA contractor report 168252, 1983. 59

[71] B. Wegner, A. Maltsev, C. Schneider, A. Sadiki, A. Dreizler, and J. Janicka, "Assessment of unsteady RANS in predicting swirl flow instability based on LES and experiments," *International Journal of Heat and Fluid Flow*, no. 3, pp. 528–536, 2004. 59

[72] X. Yang and H. Ma, "Cubic eddy-viscosity turbulence models for strongly swirling confined flows with variable density," *Int. J. Numerical Mathematics in Fluids*, pp. 985–1008, 2004. 60

[73] C. D. Pierce and P. Moin, "LES of a confined coaxial jet mixing in a confined duct," *AIAA Paper 98-2892*, 1998. 60

[74] E. von Lavante, S. Perpeet, and J. Yao, "Simulation of flow in a vortex-shedding flowmeter using an implicit solver," *AIAA Paper 99-0170, Reno*, 1999. 64

[75] S. Teukolsky, W. Vetterling, and B. Flannery, *Numerical Recipies in C++, Second Edition.* Cambridge University Press, 2002. 89

[76] D. von Lavante and E. Laurien, “Turbulent scalar flux models for the mixing of hot gases in the swirling flow of high-temperature reactor lower plenums,” *4th International Topical Meeting on High Temperature Reactor Technology, Washington DC, USA, 28. September - 1. Oktober*, 2008. 104

[77] D. von Lavante and E. Laurien, “Application of a scalar flux model to strongly swirling flows in confined geometries,” *Proceedings of 7th International ERCOFTAC Symposium on Engineering Turbulence Modelling and Measurements, Limassol, Cyprus, 4-6 Juni*, 2008. 104

[78] D. von Lavante and E. Laurien, “Comparison of turbulence models for hot gas mixing in swirling flow in high-temperature reactors,” *Proceedings of the 12th International Topical Meeting on Nuclear Reactor Thermal Hydraulics, Pittsburgh, Pennsylvania, USA, 30. September - 4. Oktober*, 2007. 104

Appendix A

Appendix

A.1 Derivation of Reynolds Stress transport equations

The transport equation for the individual Reynolds stresses $\widetilde{u_i u_j}$ are derived below. At first, a continuity equation for turbulent fluctuations will be derived. This equation will be needed later for simplifications. Given the instantaneous continuity equation (eqn. 2.1), it's instantaneous quantities are expanded in the following way: $u \rightarrow \widetilde{u} + u''$ and $\rho \rightarrow \overline{\rho} + \rho''$. From this equation, the Favre-averaged continuity equation 3.16 is subtracted resulting in the following equation:

$$\frac{\partial \rho'}{\partial t} + \frac{\partial \overline{\rho} u_i''}{\partial x_i} + \frac{\partial \rho' u_i''}{\partial x_i} + \frac{\partial \rho' \widetilde{u}_i}{\partial x_i} = 0 \tag{A.1}$$

Time-averaging the above equation is an alternative method for deriving the simplification of eqn. 3.13 yielding $\partial \left[\overline{\overline{\rho} u_i''} + \overline{\rho' u_i''} \right] / \partial x_i = 0$.

Similarly to the above equation, the instantaneous momentum transport equations are obtained from the following decomposition:

$$\begin{aligned} u &= \widetilde{u} + u'' \\ P &= \overline{P} + P' \\ \rho &= \overline{\rho} + \rho'' \\ \sigma_{ij} &= \overline{\sigma_{ij}} + \sigma'_{ij} \end{aligned} \tag{A.2}$$

this yields the momentum equation:

$$\begin{gathered}
\left(\overline{\rho}+\rho'\right)\frac{\partial\left(\widetilde{u}_i+u_i''\right)}{\partial t}+\left(\overline{\rho}+\rho'\right)\left(\widetilde{u}_j+u_j''\right)\frac{\partial\left(\widetilde{u}_i+u_i''\right)}{\partial x_j} \\
=-\frac{\partial\overline{P}}{\partial x_i}-\frac{\partial P'}{\partial x_i}+\frac{\partial\overline{\sigma_{ij}}}{\partial x_j}+\frac{\partial\sigma_{ij}'}{\partial x_j}
\end{gathered} \tag{A.3}$$

which can be rewritten as

$$\begin{gathered}
\overline{\rho}\frac{\partial\widetilde{u}_i}{\partial t}+\underbrace{\overline{\rho}\frac{\partial u_i''}{\partial t}+\rho'\frac{\partial\left(\widetilde{u}_i+u_i''\right)}{\partial t}}_{=\Pi_i}+\overline{\rho}\widetilde{u}_j\frac{\partial\widetilde{u}_i}{\partial x_j} \\
\underbrace{\overline{\rho}\widetilde{u}_j\frac{\partial u_i''}{\partial x_j}+\left(\overline{\rho}u_j''+\rho'\widetilde{u}_j+\rho'u_j''\right)\frac{\partial\left(\widetilde{u}_i+u_i''\right)}{\partial x_j}}_{=\Psi_{ij}} \\
=-\frac{\partial\overline{P}}{\partial x_i}-\frac{\partial P'}{\partial x_i}+\frac{\partial\overline{\sigma_{ij}}}{\partial x_j}+\frac{\partial\sigma_{ij}'}{\partial x_j}
\end{gathered} \tag{A.4}$$

For ease of readability the terms Π_i and Ψ_{ij} have been introduced. Subtracting from the above eqn. A.4 the Favre-averaged momentum equation (eqn. 3.17), maintaining the i-index equal between both equations, and multiplying with u_j'' results in:

$$u_j''\,\Pi_i+u_j''\,\Psi_{ik}=-u_j''\frac{\partial P'}{\partial x_i}+u_j''\frac{\partial\sigma_{ik}'}{\partial x_k}+u_j''\frac{\partial\overline{\rho}\widetilde{u_i''u_k''}}{\partial x_k} \tag{A.5}$$

Repeating the same as before, but multiplying with u_i'' instead of u_j'' will yield another set of equations shown below (eqn. A.6). Since this is a completely independent new set of equations, the common i-index needs to be called something different, in this case “j” is chosen, to differentiate them from eqn. A.5.

$$u_i''\,\Pi_j+u_i''\,\Psi_{jk}=-u_i''\frac{\partial P'}{\partial x_j}+u_i''\frac{\partial\sigma_{jk}'}{\partial x_k}+u_i''\frac{\partial\overline{\rho}\widetilde{u_j''u_k''}}{\partial x_k} \tag{A.6}$$

Adding eqn. A.5 and eqn. A.6 and averaging the result, one is presented with the result shown below:

$$\begin{gathered}
\overline{u_i''\,\Pi_j}+\overline{u_j''\,\Pi_i}+\overline{u_i''\,\Psi_{jk}}+\overline{u_j''\,\Psi_{ik}}= \\
-\overline{u_i''\frac{\partial P'}{\partial x_j}}-\overline{u_j''\frac{\partial P'}{\partial x_i}}+\overline{u_i''\frac{\partial\sigma_{jk}'}{\partial x_k}}+\overline{u_j''\frac{\partial\sigma_{ik}'}{\partial x_k}}+\overline{u_i''\frac{\partial\overline{\rho}\widetilde{u_j''u_k''}}{\partial x_k}}+\overline{u_j''\frac{\partial\overline{\rho}\widetilde{u_i''u_k''}}{\partial x_k}}
\end{gathered} \tag{A.7}$$

This set of nine equations needs to be tidied up a bit to show the familiar set of Reynold Stress transport equations. In the following, the Π containing terms will be simplified.

$$\begin{gathered}
\overline{u_i''\,\Pi_j} + \overline{u_j''\,\Pi_i} = \\
\overline{u_i''\,\bar{\rho}\frac{\partial\, u_j''}{\partial t}} + \overline{u_j''\,\bar{\rho}\frac{\partial u_i''}{\partial t}} + \overline{u_i''\rho'\frac{\partial u_j''}{\partial t}} + \overline{u_j''\rho'\frac{\partial u_i''}{\partial t}} + \overline{u_i''\rho'\frac{\partial \widetilde{u}_j}{\partial t}} + \overline{u_j''\rho'\frac{\partial \widetilde{u}_i}{\partial t}} = \\
\bar{\rho}\overline{\frac{\partial u_i''u_j''}{\partial t}} + \underbrace{\overline{\rho'\frac{\partial \widetilde{u}_i\widetilde{u}_j}{\partial t}}}_{=0} + \overline{\rho'\frac{\partial u_i''u_j''}{\partial t}} = \\
\overline{\rho\frac{\partial u_i''u_j''}{\partial t}} = \underbrace{\bar{\rho}\frac{\partial \widetilde{u_i''u_j''}}{\partial t}}_{1}
\end{gathered} \tag{A.8}$$

This term can be carried over to the final Reynold Stress transport equation. Expanding the Ψ terms of eqn. A.7

$$\begin{gathered}
\underbrace{\overline{u_j''\bar{\rho}\widetilde{u}_k\frac{\partial u_i''}{\partial x_k}} + \overline{u_i''\bar{\rho}\widetilde{u}_k\frac{\partial u_j''}{\partial x_k}}}_{I} + \overline{u_j''\bar{\rho}u_k''\frac{\partial \widetilde{u}_i}{\partial x_k}} + \overline{u_j''\rho'u_k''\frac{\partial \widetilde{u}_i}{\partial x_k}} + \overline{u_i''\bar{\rho}u_k''\frac{\partial \widetilde{u}_j}{\partial x_k}} + \overline{u_i''\rho'u_k''\frac{\partial \widetilde{u}_j}{\partial x_k}} \\
+ \underbrace{\overline{u_j''\rho'\widetilde{u}_k\frac{\partial u_i''}{\partial x_k}} + \overline{u_i''\rho'\widetilde{u}_k\frac{\partial u_j''}{\partial x_k}}}_{II} + \underbrace{\overline{u_i''\bar{\rho}u_k''\frac{\partial u_i''}{\partial x_k}} + \overline{u_j''\bar{\rho}u_k''\frac{\partial u_i''}{\partial x_k}}}_{III} \\
+ \underbrace{\overline{u_j''\rho'u_k''\frac{\partial u_i''}{\partial x_k}} + \overline{u_i''\rho'u_k''\frac{\partial u_j''}{\partial x_k}}}_{IV} + \overline{u_j''\rho'\widetilde{u}_k\frac{\partial \widetilde{u}_i}{\partial x_k}} + \overline{u_i''\rho'\widetilde{u}_k\frac{\partial \widetilde{u}_j}{\partial x_k}} =
\end{gathered} \tag{A.9}$$

Using the product rule, the following simplifications can be made to terms I, II, III and IV:

$$\begin{gathered}
\underbrace{\overline{\bar{\rho}\widetilde{u}_k\frac{\partial u_i''u_j''}{\partial x_k}} + \overline{\bar{\rho}\widetilde{u}_k\frac{\partial u_i''u_j''}{\partial x_k}}}_{I} + \underbrace{\overline{u_j''\rho'u_k''\frac{\partial \widetilde{u}_i}{\partial x_k}} + \overline{u_j''\rho'u_k''\frac{\partial \widetilde{u}_i}{\partial x_k}}}_{II} + \underbrace{\overline{u_i''\bar{\rho}u_k''\frac{\partial \widetilde{u}_j}{\partial x_k}} + \overline{u_i''\rho'u_k''\frac{\partial \widetilde{u}_j}{\partial x_k}}}_{III} \\
+ \overline{\bar{\rho}u_k''\frac{\partial u_i''u_i''}{\partial x_k}} + \overline{\rho'u_k''\frac{\partial u_i''u_j''}{\partial x_k}} + \overline{u_j''\rho'\widetilde{u}_k\frac{\partial \widetilde{u}_i}{\partial x_k}} + \overline{u_i''\rho'\widetilde{u}_k\frac{\partial \widetilde{u}_j}{\partial x_k}}
\end{gathered} \tag{A.10}$$

Terms I, II and III can be combined as follows:

$$I \;=\; \bar{\rho}\widetilde{u}_k\frac{\partial \widetilde{u_i''u_j''}}{\partial x_k}$$

$$\begin{aligned} II &= \bar{\rho}\widetilde{u_j'' u_k''}\frac{\partial \widetilde{u}_i}{\partial x_k} \\ III &= \bar{\rho}\widetilde{u_i'' u_k''}\frac{\partial \widetilde{u}_j}{\partial x_k} \end{aligned} \tag{A.11}$$

These terms can be taken over to the final equation, the remainder will be combined with other terms.

In equation A.7 the pressure terms and laminar diffusion terms σ can be reformulated via the product rule:

$$\begin{gathered} \overline{u_i''\frac{\partial P'}{\partial x_j}} + \overline{u_i''\frac{\partial P'}{\partial x_j}} = \\ \frac{\partial \overline{P'u_i''}}{\partial x_j} - \overline{P'\frac{\partial u_i''}{\partial x_j}} + \frac{\partial \overline{P'u_j''}}{\partial x_i} - \overline{P'\frac{\partial u_j''}{\partial x_i}} = \\ \overline{-P'\left(\frac{\partial u_i''}{\partial x_j} + \frac{\partial u_j''}{\partial x_i}\right)} + \frac{\partial \overline{P'u_i''}}{\partial x_k}\delta_{jk} + \frac{\partial \overline{P'u_j''}}{\partial x_k}\delta_{ik} \qquad (A.12) \\ (A.13) \end{gathered}$$

And for σ

$$\begin{gathered} \overline{u_j''\frac{\partial \sigma'_{ik}}{\partial x_k}} + \overline{u_i''\frac{\partial \sigma'_{jk}}{\partial x_k}} = \\ \frac{\partial \overline{\sigma'_{ik}u_j''}}{\partial x_k} - \overline{\sigma'_{ik}\frac{\partial u_j''}{\partial x_k}} + \frac{\partial \overline{\sigma'_{jk}u_i''}}{\partial x_k} - \overline{\sigma'_{jk}\frac{\partial u_i''}{\partial x_j}} = \end{gathered}$$

These terms can be taken over to the final equation. The remaining terms are as follows, and can be simplified after some algebraic manipulation and the application of the product and chainrule:

$$\begin{gathered} \overline{\bar{\rho}u_k''\frac{\partial u_i''u_i''}{\partial x_k}} + \overline{\rho' u_k''\frac{\partial u_i''u_j''}{\partial x_k}} + \underbrace{\overline{u_j''\rho'\widetilde{u}_k\frac{\partial \widetilde{u}_i}{\partial x_k}} + \overline{u_i''\rho'\widetilde{u}_k\frac{\partial \widetilde{u}_j}{\partial x_k}}}_{=0 \text{ due to continuity}} \qquad (A.14) \\ \overline{-u_j''\frac{\partial \bar{\rho}\widetilde{u_i''u_k''}}{\partial x_k}} - \overline{u_i''\frac{\partial \bar{\rho}\widetilde{u_j''u_k''}}{\partial x_k}} \\ = \frac{\partial}{\partial x_k}\left[\overline{\rho u_i''u_j''u_k''}\right] \end{gathered}$$

Collecting all terms will yield the final transport equation for Reynolds stresses:

$$
\begin{aligned}
&\underbrace{\overline{\rho}\frac{\partial \widetilde{u_i''u_j''}}{\partial t}}_{\text{rate of change}} + \underbrace{\overline{\rho}\widetilde{u}_k\frac{\partial \widetilde{u_i''u_j''}}{\partial x_k}}_{\text{convection}} = \underbrace{-\overline{\rho}\widetilde{u_j''u_k''}\frac{\partial \widetilde{u}_i}{\partial x_k} - \overline{\rho}\widetilde{u_i''u_k''}\frac{\partial \widetilde{u}_j}{\partial x_k}}_{\text{production}} \\
&+ \underbrace{\frac{\partial}{\partial x_k}\left[\overline{\rho}\widetilde{u''_i u''_j u''_k} + \overline{p'u''_i}\delta_{jk} + \overline{p'u''_j}\delta_{ik} - \overline{u_i''\sigma_{jk}} - \overline{u_j''\sigma_{ik}}\right]}_{\text{diffusion}} \qquad \text{(A.15)} \\
&\underbrace{-\overline{u_j''}\frac{\partial \overline{p}}{\partial x_i} - \overline{u_i''}\frac{\partial \overline{p}}{\partial x_j}}_{\text{density-velocity covariance}} \underbrace{+\overline{p'\left(\frac{\partial u''_i}{\partial x_j} + \frac{\partial u''_j}{\partial x_i}\right)}}_{\text{pressure strain-rate correlation}} \underbrace{-\overline{\sigma_{ik}\frac{\partial u_j''}{\partial x_k}} - \overline{\sigma_{jk}\frac{\partial u_i''}{\partial x_k}}}_{\text{viscous dissipation}}
\end{aligned}
$$

A.2 The $\lambda 2$ criterion for identification of 3D swirl

The $\lambda 2$ criterion can be used to identify swirl centers in complex 3D swirling motion. The most commonly used method of identifying swirl centers is via simple visual inspection, but for the case of 3D swirl, the fluid motion may appear too chaotic. In addition one is faced with the problem that depending on the angle of the cutting plane used for generating vector plots, the swirl center will move significantly and it is very difficult to extract information about the exact direction of the swirling motion. An analytical tool which can automatically identify and highlight swirling motion is hence needed. One of the most commonly used analytical methods in CFD to visualize swirling motion is the so-called $\lambda 2$ criterion. It postulates the following:

Swirl occurs where the Eigenvalues of the fluid strain tensor $\Theta_{ij} = \partial u_i / \partial x_j$ have complex solutions. Given the Cayley-Hamilton theorem, one can rewrite the Eigenvalue problem of Θ_{ij} into the following Eigenvector form:

$$\lambda^3 + \lambda^2 P + \lambda Q + R = 0 \tag{A.16}$$

Where λ is the Eigenvector of Θ_{ij} and P, Q and R are the 1st, 2nd and 3rd invariants of Θ_{ij} respectively. They are defined as shown below:

$$\begin{aligned} P &= \Theta_{ii} \\ Q &= 1/2\left(\Theta_{ij}\,\Theta_{ji} - (\Theta_{ii})^2\right) \\ R &= \det\left(\Theta_{ij}\right) \end{aligned}$$

The above Eigenvector equation is a cubic polynomial equation, which has complex solutions given the following condition is satisfied:

$$\left(\frac{Q}{3}\right)^3 + \left(\frac{R}{2}\right)^2 < 0 \tag{A.17}$$

Satisfying this condition is called the $\lambda 2$ criterion. Swirl centers can be identified by plotting iso-surfaces of a constant negative $\lambda 2$ value.